The Diffractive Photoproduction of J/Ψ Vector Mesons with High Transverse Momenta at HERA

Duncan P. Brown

Year 2000

THE UNIVERSITY
of MANCHESTER

Particle Physics Group
Department of Physics and Astronomy

A thesis submitted to the University of Manchester for the degree of Doctor of Philosophy in the Faculty of Science and Engineering.

Contents

List of Figures

List of Tables

Abstract

The differential cross section $d\sigma/dt$ is measured as a function of $|t|$ for diffractive J/Ψ production in the kinematic region $|t| = 0 - 10$ GeV^{2}c^{-2} using data taken during 1997 by the H1 detector at HERA. Events are selected in which proton remnants masses greater than about 1.6 GeVc^{-2} are produced at the proton vertex and in which a J/Ψ vector meson is produced elastically, with a photon elasticity $z > 0.8$, off an incoming photon of virtuality $Q^2 < 0.01$ GeV^{2}c^{-2} at the photon vertex. The measurement is made in the photon-proton centre-of-mass energy ranges 60 GeV $< W_{\gamma p} <$ 147 GeV and 165 GeV $< W_{\gamma p} <$ 233 GeV. An exponential behaviour of the differential cross section is observed in both centre-of-mass energy ranges. A shift towards lower values of $|t|$ appears in the observed cross sections as $W_{\gamma p}$ increases. Gradients of $\alpha' = 0.016 \pm 0.005$ GeV^{-2}c^2 and $\alpha' = 0.016 \pm 0.010$ GeV^{-2}c^2 are extracted from functional fits to the differential cross section for the pomeron trajectory in the lower and higher $W_{\gamma p}$ ranges respectively. These observations are consistent with a shrinkage of the diffraction peak predicted by Regge theory, but not expected within the framework of perturbative QCD. The differential cross section $d\sigma/dW^2_{\gamma p}$ is measured as a function of $s = W^2_{\gamma p}$ in the same kinematic regions for diffractive J/Ψ production in which a remnant mass less than about 1.6 GeVc^{-2} is produced at the proton vertex . The differential cross section is converted into a measurement of the total cross section as a function of s. The total cross section rises over the s-range investigated. It is not possible to rule out deviations away from a smooth dependence in the total cross section with increasing s, and in the differential cross section with increasing s. The measurements are consistent with the Regge theory description of the pomeron and with the results of similar analyses in the muon channel.

Declaration

No portion of the work referred to in this thesis has been submitted in support of an application for another degree or qualification of this or any other institute of learning.

Chapter 1

Introduction.

One of the best ways to develop a deeper understanding of the structure of particles and of the nature of the forces between them is to scatter them off one another. A good way to proceed is to perform experiments in which the projectile particle, together with its interaction with other particles, is reasonably well understood and the target particle is to be investigated. A good choice for the projectile particle would be the electron, for example, since a great deal of work towards understanding this particle and the electromagnetic force has already been completed. The target particle might then be chosen to be the neutron or the proton, of which comparatively little is known. The fact that the negatively charged electron interacts at all with the neutrally charged neutron, for example, suggests that the neutron may be made up from smaller charged constituents [1].

Since the early 1950s large particle collision experiments have been built to probe the structure of the smallest known particles. Colliding beam experiments today complement the earlier fixed target approach, however the total cross section and its related differential cross sections, are still usually the first quantities to be investigated experimentally. Cross sections are important quantities in particle physics since they are proportional to the probability for scattering and contain a large amount of information about the structure of the target, and of the forces between it and the projectile. It was therefore surprising when many of the first cross sections to be measured displayed very similar properties, even though a variety of different target and projectile particles had been used.

To understand the origin of these similarities work began to try to develop a theoretical model of the scattering process. This proved to be very difficult at first since no detailed knowledge as to whether any constituent particles were contained inside the target particles existed, no such constituent particles having ever been directly observed. A theory based on very general assumptions concerning scattering behaviour was therefore developed which was expected to describe the behaviour of almost all scattering processes. This theory, which was essentially completed during the 1960s, is often referred to as Regge theory, after Italian scientist T. Regge who made an important contribution towards its completion. When compared with experimental data the predictions of Regge theory were found to agree with many of the scattering measurements. At higher centre-of-mass energies, however, it could no longer describe certain experimentally measured cross sections unless an entire set of particles existed which had not been detected experimentally. This group of particles is referred to as the pomeron, after Russian physicist I. Y. Pomeranchuk.

The member particles of the pomeron are very specific in that it is expected that when their external angular momentum values are plotted as a function of the square of their masses it will be possible to draw a smooth function, or trajectory, through the points. Also, within the framework of Regge theory, it could be shown that they must each carry the same quantum numbers as the vacuum. Since these new particle states could be made up from smaller constituent particles, the constituents would then have to collect themselves together in such a way that they create a bound-state which is effectively invisible against a background of empty space. The member particles of the pomeron are therefore very difficult to detect directly. In 1994, however, some evidence was presented for a possible bound two-gluon, or glueball, state with a mass of about 1.9 GeVc^{-2} and the correct quantum numbers to be a member of the pomeron set [2]. This observation, however, has never been confirmed, so the member particles of the pomeron still await experimental verification today.

Since the 1960s a more complex extension to the theory of particle scattering has also been developed. This contains hypotheses as to which particles have smaller constituents, what these constituents might be and how these would then bind together. This theory is referred to as the standard model. A section of this model, which is used to describe the strong interaction, predicts processes in which 'objects' with the quantum numbers of the vacuum may be exchanged between the

particles participating in a scattering experiment. This is referred to as quantum chromodynamics, or QCD, and its predictions are expected to agree with those of Regge theory. QCD is also able to describe many scattering measurements. It does not, however, usually incorporate the possible existence of bound particles with the quantum numbers of the vacuum. In addition, its predictions may disagree with some of those of Regge theory concerning the physical behaviour of the pomeron. The pomeron is therefore an object of some considerable interest in particle physics.

Rather than attempting to directly detect the pomeron particles it is also possible that evidence for their existence might be found in processes in which they would be expected to play a role if they exist. It has recently been demonstrated that the predicted QCD cross sections for one such process, the diffractive production of vector mesons, in which the magnitude of the Mandelstam variable t is large, are not expected to be restrictively small in the kinematic regime accessible to the HERA lepton-proton collider. The HERA collider was designed to perform a deeper investigation of the substructure of the proton and is located in Hamburg at DESY (Deutsches Elektronen-Synchrotron). Since this process is mediated by the exchange of the quantum numbers of the vacuum, should any member particles of the pomeron exist with masses corresponding to this kinematic region then it may be possible to identify them.

In the work described here the differential cross section $d\sigma/dt$ is measured as a function of t for diffractively produced J/Ψ vector mesons selected via their decays into electron-positron pairs. This measurement is made for processes in which the proton dissociates, in two different photon-proton centre-of-mass energy regions. Since the Regge theory description of the scattering force is based on families of particle resonances, the proton-intact process is also investigated, in both centre-of-mass energy regions, for resonance effects. All measurements are made in the kinematic region of photoproduction, in which the incoming lepton at HERA is scattered through a small angle emitting an almost-real photon. Since the cross section is high at HERA for photoproduction events this is expected to help compensate for the small cross section of the diffractive process. These measurements apply to data taken during 1997 by the H1 detector, one of the four detector experiments of the HERA accelerator. The integrated luminosity at the end of 1997 was higher than for previous data-taking periods. HERA collided beams of 27.6 GeV positrons with beams of 820 GeV protons during this period.

One explanation for the current disagreements between Regge theory and QCD is that the QCD prediction only becomes valid at larger values of t. The Regge theory behaviour, which was extracted at lower values of t, may agree with the QCD prediction in this higher t-region. The aim of this work is to determine whether any particles belonging to the pomeron exist with masses corresponding to the kinematic range accessible to the HERA collider and to test the QCD and Regge theory predictions for the behaviour of this process experimentally.

Chapter 2

Regge Theory and the Pomeron.

Many scattering processes, first experimentally investigated using the fixed target colliders of the 1950s, display very similar properties. Since no detailed knowledge was available as to whether any constituent particles existed in the target particles the first theoretical expressions for particle scattering were derived from very simple assumptions concerning the general scattering process. These assumptions were expected to apply to almost all scattering processes and the expressions obtained were therefore expected to account for the similarities between scattering measurements.

In this chapter the derivation of the Regge theory description of particle scattering is followed from its origin in quantum theory. The quantum mechanical wave treatment of the scattering process is chosen and it is explained how expressions for the total and differential cross sections are obtained from an expression for the amplitude of the scattered wave. The scattering amplitude is then examined in more detail, expanded as a series in partial waves, each partial wave describing one angular momentum component of the incoming beam. A useful relationship referred to as the optical theorem is then derived. A complete expression for the scattering amplitude is then obtained if the phase shifts between the incoming and scattered waves are known. This is illustrated using the process of resonance production. The phase shifts, however, are not usually available. The quantum mechanical description of the scattering process is then extended to relativistic scattering energies so that comparisons may be made to relativistic scattering measurements. The frame-

dependent quantities are first replaced by the relativistically invariant Mandelstam variables and the similarities between scattering measurements are accounted for using crossing symmetry. The centre-of-mass energy is then allowed to become large and an important method using dispersion relations which attempted to extract the behaviour of the scattering amplitude in this limit is then discussed. A discussion of the successful Regge approach, in which angular momentum was treated as a complex and continuous variable, then follows. The scattering force may then be interpreted in terms of Reggeon exchange, the exchange of Regge trajectories. The discussion that follows then concentrates on those aspects which suggested the existence of a pomeron family and the properties that the member particles of this family are expected to possess. This chapter opens with the definition of the total and differential cross sections and the relationship between them.

In a typical fixed target experiment a beam of particles is fired at a stationary target made up from some material. Some of the particles will pass through the target material unaffected and continue in the same direction as the incoming beam. From time to time, however, incoming particles will meet particles present in the target material, interact and scatter. There are various directions in which these may then leave the interaction region. Provided the incoming particles are uniformly incident on the target the probabilty (P_s) that an incoming particle scatters is related to the total cross section (σ) according to

$$P_s = n_0 \sigma dz$$

where the target material has a particle number density n_0 and thickness dz. The total cross section is a measure of the 'effective' cross sectional area of a target particle which gives rise to scattering. This 'effective' area may vary as the energy of the incoming particles is increased, for example, and therefore contains a large amount of information concerning the structure of the target particles. Other processes such as absorption of the incident particles by the target particles may also occur but these are not considered here. The process of diffraction will be considered later.

To obtain an expression for the probabilty (P_Ω) that an incoming particle scatters into a smaller angular region of opening angle $d\Omega$, the expression for the total scattering probability is differentiated with respect to solid angle. This gives

$$P_\Omega = n_0 dz \frac{d\sigma}{d\Omega}.$$

This quantity is related to the angular differential cross section $d\sigma/d\Omega$ which contains a large amount of information concerning the forces between the target and the projectile. These influence the probability that an incoming particle will scatter in a given direction. A differential cross section describing the probabilty that an incoming particle scatters into a small range in any measurable variable may clearly be obtained by instead differentiating the total scattering probability with respect to other variables.

The total cross section may be re-obtained by integrating-back any differential cross section over all possible values of the variable to which it applies. This is because the smaller probabilities for scattering into each smaller region, when summed, must equal the total probability for scattering. It is only necessary, therefore, to obtain a single theoretical expression for the angular differential cross section since this may be integrated-back to obtain an expression for the total cross section. Expressions for other differential cross sections, if required, may then be obtained by differentiating the total cross section with respect to other variables.

An expression for the angular differential cross section may be derived for non-relativistic scattering energies. To obtain an expression for relativistic particle scattering its behaviour as the typical energy of the projectile is increased, together with any alterations necessary to incorporate any other processes which enter at relativistic energies, must then be considered. At non-relativistic speeds the general scattering process may be viewed in either the particle or the equivalent quantum-mechanical wave picture. The expressions obtained will be equivalent to each other due to wave-particle duality. The general scattering process in the wave picture is shown in figure 2.1. Here the beam of particles constantly incident on the target is described by an incoming wave Ψ_i which is chosen to approach the target along the positive z-axis. The origin is chosen to be at the centre of the target. Each of the particles approaching in the beam are assumed to have the same energy. The beam would normally be produced from a general initial particle beam by collimators which only allow particles to pass through a small opening. Provided this opening is larger that the wavelength of the initial incoming wave and larger than the size of the target then the incoming wave may be approximated by a plane wave [3]. Some of the particles in the beam will pass through the target unaffected giving rise to an outgoing unscattered wave Ψ_f. The unscattered wave will also be described by a plane wave. The amplitude of the unscattered wave, however, is expected to

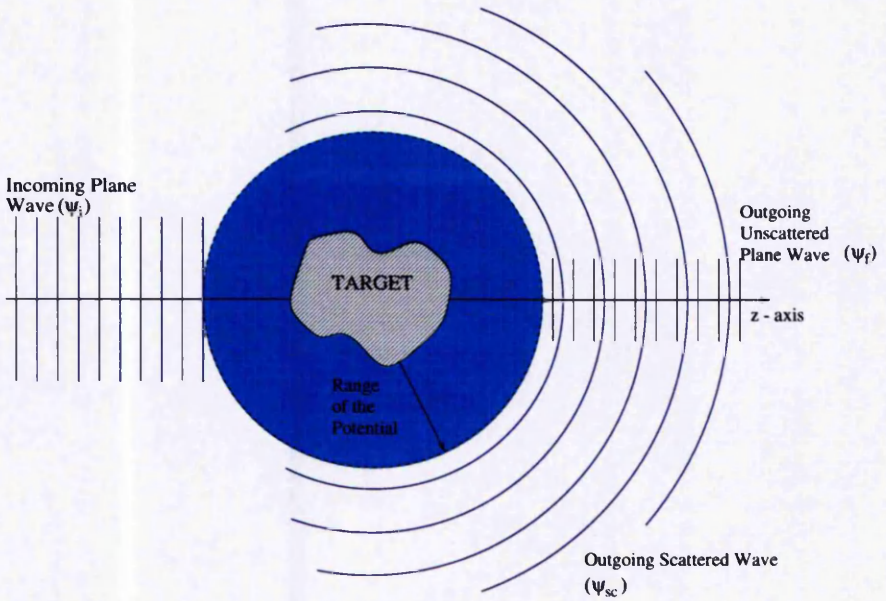

Figure 2.1: The general scattering process in the wave-picture. The incoming beam of particles is described by a plane wave Ψ_i. Some particles pass through the target material unaffected giving rise to an unscattered wave Ψ_f. The rest interact with particles present in the target and scatter giving rise to a scattered wave Ψ_{sc}.

be smaller than that of the incoming wave since it will contain fewer particles. If, for example, the amplitude of the incoming wave is normalised to unity then the probability for no scattering will be given by the square of the amplitude of the unscattered wave. Clearly this is expected to be lower than unity since, in general, some of the incident particles will interact with particles present in the target and give rise to an outgoing scattered wave Ψ_{sc}.

To obtain an expression for the angular differential cross section it is necessary to know the form of the scattered wave. This contains the details on how particles scatter as a function of theta and phi, where theta and phi refer to the spherical polar coordinate system. For non-relativistic scattering the wavefunction describing the scattering process is expected to be a solution to the Schrödinger equation. It is expected then that the set of eigenfunctions (Ψ) describing the scat-

tering problem in the region away from the target can be written in the form

$$\Psi = e^{ikz} + \Psi_{sc}.$$

Here the plane waves corresponding to the incoming and unscattered waves have been combined into a single term, and the normalisation of the wavefunction has been chosen so that the amplitude of the combined plane wave equals unity. By first obtaining the eigenfunctions of the scattering problem and then extracting the term corresponding to the plane wave it will be possible to separate the contribution of the scattered wave to the wavefunction. This may then be used to calculate the angular differential cross section.

It may be assumed that the force between the projectile and the target is described by a potential which dies away as the distance from the target increases. In the region close to the target detailed knowledge of the potential arising from the target particles, and also any constituents that these particles may have, would be required. This region was avoided in the development of Regge theory. In the region away from the target the influence of the potential is neglected. Since an incoming plane wave is constantly entering the interaction region, and an unscattered and a scattered wave are constantly leaving, a steady-state situation develops. The wavefunction describing this region is therefore expected to be a solution to the time-independent Schrödinger equation.

2.1 The Scattered Wave.

Consider first the general solutions to the time-independent Schrödinger equation in a region where absolutely no potential is present, including the region close to the origin. These are the general solutions (Ψ_k) to the so-called free-particle Schrödinger equation

$$\frac{\hbar^2}{2m}\nabla^2\Psi_k + E\Psi_k = 0.$$

The solutions may be obtained in any coordinate system. The solutions in spherical polar coordinates, however, are the most sensible to consider, since it will then be a simple matter to fit them into the region away from the target in the scattering picture by considering the limit $r \to \infty$. It will be recalled that the general method

for obtaining the general solutions is to begin by writing the wavefunction as a product of a function which depends only on the radius r, a function which depends only on theta and a function which depends only on phi. The wavefunction in this form is then substituted into the Schrödinger equation and operated through the Laplacian operator ∇^2, written in spherical polar coordinates. The result may then be rearranged such that one side of the expression only depends on the radius, and the other side contains all the angular dependence. The only way in which this expression can hold is then if both sides individually equal some constant. This may be written as $\lambda_1\hbar^2$. The problem is then reduced to two separate equations, one describing the behaviour of the radial function and one describing the angular behaviour. Both equations individually equal the same constant.

The same process, however, may then be repeated for the angular equation, separating it into a theta equation and a phi equation. Both equations once again must individually equal some constant λ_2. The radial, theta and phi dependencies of the wavefunction can therefore be separated. The phi equation may be solved first to obtain the phi-dependent part of the wavefunction. If the constant λ_2 is written as m^2, where m is the magnetic quantum number, then these solutions are proportional to $\exp(\imath m\phi)$. Since the full wavefunction is required to be single valued, the value of the phi-dependent solutions at ϕ are required to equal their value at $\phi + 2\pi$, and the magnetic quantum number must therefore be restricted to take only positive or negative integer values, or zero. The value of $\lambda_2 = m^2$, together with the restriction on m, are then propagated through to the theta equation which may be solved next. The solutions to the theta equation for $m = 0$ are then the Legendre Polynomials $P_l(\cos\theta)$. If $m \neq 0$ the solutions are the more complicated associated Legendre functions. In both cases, however, the value of the constant λ_1 is given by

$$\lambda_1 = l(l+1)$$

where l is the angular momentum quantum number. The theta solutions may be combined with the phi solutions and written as $Y_l^m(\theta,\phi)$. The functions $Y_l^m(\theta,\phi)$ are referred to as the spherical harmonic functions. The angular momentum quantum number l may also only take positive or negative integer values, or zero, due to the restriction on m. Only those values greater than or equal to zero are selected, however, since a particle is not physically expected to carry a negative angular momentum value. For any fixed angular momentum l, the magnetic quantum number may only take integer values ranging between +l and -l.

Finally the angular solutions together with the restrictions on both quantum numbers are carried through to the radial equation. To solve this a raising and a lowering operator may be defined which generate the entire set of solutions to the radial equation from its solutions at an angular momentum of $l = 0$. Since there are two solutions at $l = 0$, two towers of total solutions are generated by repeatedly operating with the raising operator on each $l = 0$ solution. One $l = 0$ solution generates the set of spherical Bessel functions $j_l(kr)$ and the other generates the set of spherical Neumann functions $n_l(kr)$. Some general linear combination of these two results then gives the general form of the total solution to the radial equation. Combining all of this together gives the following result

$$\Psi_k = \sum_l \sum_m \left(A_l\, j_l(kr) + B_l\, n_l(kr)\right) Y_l^m(\theta, \phi) \tag{2.1}$$

where A_l and B_l are the constants arising from the general linear combination in the radial solution [1].

These general solutions, however, apply to a region where there is absolutely no potential. In the scattering problem a potential exists in the region close to the target. The general solutions to the free-particle Schrödinger equation are therefore only expected to apply in the scattering problem when the separation from the origin (r) is large. The spherical Bessel functions in this limit [4] behave as follows

$$j_l(kr) \xrightarrow{r\to\infty} \frac{\sin\left(kr - \frac{l\pi}{2}\right)}{kr}$$

and the spherical Neumann functions in the same limit have the following behaviour

$$n_l(kr) \xrightarrow{r\to\infty} \frac{-\cos\left(kr - \frac{l\pi}{2}\right)}{kr}.$$

The eigenfunctions Ψ to the scattering problem in the region outside of which the potential acts are therefore

$$\Psi = \sum_l \sum_m \left(\frac{A_l}{kr}\, \sin\left(kr - \frac{l\pi}{2}\right) - \frac{B_l}{kr}\, \cos\left(kr - \frac{l\pi}{2}\right)\right) Y_l^m(\theta, \phi).$$

The expression may be simplified by combining the sine and cosine functions into a single sine function using the trigonometric identity

$$R\sin(\theta + \delta) = a\sin\theta + b\cos\theta$$

which follows from the relationship

$$\sin(\theta + \delta) = \sin\theta\cos\delta + \cos\theta\sin\delta$$

if the cosine and sine of the angle δ are written in terms of the side lengths of a right angled triangle. With $\cos\delta = \frac{a}{R}$ and $\sin\delta = \frac{b}{R}$, where $R^2 = a^2 + b^2$ and $\tan\delta = \frac{b}{a}$, the result follows. The wavefunction is then

$$\Psi = \sum_l \sum_m \left(\frac{C_l}{kr} \sin\left(kr - \frac{l\pi}{2} + \delta_l(k) \right) \right) Y_l^m(\theta, \phi).$$

It is now clear that the effect of the potential close to the origin is to introduce a phase shift $\delta_l(k)$ to the wave function.

To identify the form of the scattered wave this now needs to be separated into the sum of two terms, one of which may be identified with the plane wave. Before approaching this the wavefunction may be further simplified, however, using the fact that a great many scattering processes show no variation with azimuthal angle phi. The azimuthal dependence is therefore not needed. Since the phi-dependent part of the wavefunction is proportional to $\exp(\imath m\phi)$ this is done by only considering the $m = 0$ terms. The sum over m may therefore be removed and the spherical harmonic functions replaced by the Legendre polynomials

$$P_l(\cos\theta) = \left(\frac{4\pi}{2l+1} \right)^{\frac{1}{2}} Y_l^0.$$

These were the solutions to the theta equation for $m = 0$. The expression for the wavefunction which is to be separated therefore becomes

$$\Psi = \sum_l \frac{C_l'}{kr} \sin\left(kr - \frac{l\pi}{2} + \delta_l(k) \right) P_l(\cos\theta)$$

where

$$C_l' = \left(\frac{2l+1}{4\pi} \right)^{\frac{1}{2}} C_l.$$

To separate the wavefunction the sine function is first written in its complex form giving

$$\Psi = \sum_{l=0}^{\infty} \frac{C_l'}{2\imath kr} \left(e^{\imath\left(kr - \frac{l\pi}{2} + \delta_l(k)\right)} - e^{-\imath\left(kr - \frac{l\pi}{2} + \delta_l(k)\right)} \right) P_l(\cos\theta).$$

The eigenfunctions are now given by a sum of an incoming and an outgoing spherical wave. The general form of a spherical wave is $Ae^{\imath\theta}/r$, where A is some fixed constant.

An exponential factor is now factorised out to give

$$\Psi = \sum_{l=0}^{\infty} \frac{C_l'}{2ikr}\, e^{-i\left(\frac{l\pi}{2}+\delta_l(k)\right)} \left(e^{i(kr+2\delta_l(k))} - e^{-i(kr-l\pi)}\right) P_l(\cos\theta).$$

A factor e^{ikr} is now added and subtracted, so that the net effect of doing this is to add zero, giving

$$\Psi = \sum_{l=0}^{\infty} \frac{C_l'}{2ikr}\, e^{-i\left(\frac{l\pi}{2}+\delta_l(k)\right)} \left(e^{i(kr+2\delta_l(k))} - e^{-i(kr-l\pi)} + e^{ikr} - e^{ikr}\right) P_l(\cos\theta).$$

The wavefunction may now be separated into the sum of two terms. The first is given by

$$\sum_{l=0}^{\infty} \frac{C_l'}{2ikr}\, e^{-i\left(\frac{l\pi}{2}+\delta_l(k)\right)} \left(e^{ikr} - e^{-i(kr-l\pi)}\right) P_l(\cos\theta). \tag{2.2}$$

and corresponds to the sum of the second and third terms of the previous expression. This may be identified with the plane wave. This follows because the general solutions to the free-particle Schrödinger equation in Cartesian coordinates must equal the general solutions in spherical polar coordinates. The general solutions in spherical polar coordinates have already been considered and are given by equation 2.1. The general solution in Cartesian coordinates is just a plane wave for a general particle momentum 3-vector $\vec{p}_i$ [5],

$$\Psi = \frac{1}{(2\pi\hbar)^{\frac{3}{2}}} \exp\left(\frac{i\vec{p}_i \cdot \vec{r}}{\hbar}\right).$$

If this is substituted into the time-independent Schrödinger equation the well known expression

$$E = \frac{\hbar^2 |\vec{k}_i|^2}{2m}$$

is obtained. The plane wave solution in Cartesian coordinates is equal to the expression given in equation 2.1. A plane wave travelling in the direction of increasing z, however, has the form

$$\exp(ikz) = \exp(ikr\cos\theta).$$

This will be equal to some special linear combination of the eigenfunctions in spherical polar coordinates. Since the incoming plane wave is independent of the azimuthal angle ϕ, here also only the $m = 0$ solutions in spherical polar coordinates will be

needed. The spherical harmonic functions may again be replaced by the Legendre polynomials. The expression [6] turns out to be

$$\exp(\imath kr\cos\theta) = \sum_{l=0}^{\infty}(\imath)^l(2l+1)j_l(kr)P_l(\cos\theta).$$

In the region away from the potential, where the radius r tends to infinity, the behaviour of the spherical Bessel functions in this region, where the sine function has again been written in its complex form, gives

$$\exp(\imath kz) = \frac{1}{2\imath k}\sum_{l=0}^{\infty}\imath^l(2l+1)\frac{\left(e^{\imath(kr-\frac{l\pi}{2})} - e^{-\imath(kr-\frac{l\pi}{2})}\right)}{r}P_l(\cos\theta).$$

Here the $\imath^l$ factor may be re-written using the fact that $\imath = e^{\frac{\imath\pi}{2}}$ giving

$$\exp(\imath kz) = \frac{1}{2\imath k}\sum_{l=0}^{\infty}(2l+1)\frac{\left(e^{\imath kr} - e^{-\imath(kr-l\pi)}\right)}{r}P_l(\cos\theta).$$

This is equal to Equation 2.2. if the constant C_l' is chosen to be

$$C_l' = (2l+1)e^{\imath\left(\frac{l\pi}{2}+\delta_l(k)\right)}.$$

The normalisation of the plane waves is now set to equal unity. Clearly other normalisations may be chosen. The second term corresponds to the first and fourth terms of the separated wavefunction and is given by

$$\sum_{l=0}^{\infty}\frac{C_l'e^{-\imath(\frac{l\pi}{2}+\delta_l(k))}e^{\imath kr}}{2\imath kr}\left(e^{2\imath\delta_l(k)} - 1\right)P_l(\cos\theta).$$

This must therefore correspond to the scattered wave. Here an additional factor of $e^{\imath kr}$ has been factorised out. Inserting the value of the constant C_l' gives

$$\sum_{l=0}^{\infty}\frac{(2l+1)e^{\imath kr}}{2\imath kr}\left(e^{2\imath\delta_l(k)} - 1\right)P_l(\cos\theta).$$

This may be written in the form

$$\Psi_{sc} = f(k,\cos\theta)\frac{e^{\imath kr}}{r}.$$

The scattered wave is therefore outgoing spherically symmetric. The function $f(k,\cos\theta)$ is given by

$$f(k,\cos\theta) = \frac{1}{2\imath k}\sum_{l=0}^{\infty}(2l+1)\left(e^{2\imath\delta_l(k)} - 1\right)P_l(\cos\theta) \qquad (2.3)$$

and is referred to as the scattering amplitude.

2.2 The Angular Differential Cross Section.

Now that the form of the scattered wave is known an expression for the angular differential cross section may be obtained by considering the probability current densities ($\vec{j}$) associated with the plane wave and the scattered wave. The probability current density associated with a wave is an expression for the probability flowing per unit time per unit area, where the area is perpendicular to the direction of the vector quantity $\vec{j}$. The probability current density may be considered as being analogous to the current density of electromagnetism.

In electromagnetism the amount of charge which lies inside a volume V is conserved. Should the amount of charge fall inside the volume then this must be accompanied by a flow of charge through the surface enclosing the volume. In quantum theory the conserved quantity is the probability for finding a particle inside a volume V. Should the probability fall inside the volume then this must be accompanied by a flow of probability through the enclosing surface. This relationship is described by the continuity equation in quantum theory. The probability current density is defined by the continuity equation and is calculated from a wavefunction according to the following expression

$$\vec{j} = \frac{\hbar}{2mi}(\Psi^*\nabla\Psi - \Psi\nabla\Psi^*)$$

where the * represents complex conjugation. The scattered probability current density is then obtained by setting

$$\Psi = \Psi_{sc} = f(k, \cos\theta)\frac{e^{ikr}}{r}.$$

Since r, the distance from the origin, has been allowed to tend to infinity the ∇-operator only contains an $\hat{r}$-component, since the other components are all negligible in comparison due to their inverse r-dependencies. Therefore

$$\nabla\left(f(k, \cos\theta)\frac{e^{ikr}}{r}\right) = \left(f(k, \cos\theta)ik\frac{e^{ikr}}{r}\right)\hat{r}$$

and the scattered probability current density is

$$\vec{j}_{sc} = \frac{1}{r^2}|f(k, \cos\theta)|^2\frac{\hbar k}{m}\hat{r}.$$

The quantity $\vec{j}_{sc} \cdot d\vec{S}$ is then the probability flowing per unit time through a small element of the surface area of size $|d\vec{S}|$. Since the expression is calculated in spherical

polar coordinates the surface is chosen to enclose a sphere centred at the origin. In spherical polar coordinates the surface vector then points radially outwards from the origin and is given by

$$\vec{dS} = r^2 d\Omega \hat{\mathbf{r}}.$$

The amount of probability flowing outwards per second through a small angular region of solid angle $d\Omega$ is then given by

$$\vec{j}_{sc} \cdot \vec{dS} = |f(k, \cos\theta)|^2 \frac{\hbar k}{m} d\Omega.$$

This is the expression for the number of particles dN_s that scatter per second into a small angular region of opening angle $d\Omega$.

Rather than considering the target as being comprised of many target particles, for the purpose of deriving a theoretical expression it is of interest to know how particles will scatter off a single target particle. The number of incoming particles which meet the target per second is given by

$$\vec{j}_{inc} \cdot \vec{dS} = \sigma |\vec{j}_{inc}|$$

where σ is the total cross section, or the area of the target particle. The magnitude of the probability current density associated with the plane wave may be obtained using the same expression as before and is given by

$$|\vec{j}_{inc}| = \frac{\hbar k}{m}.$$

Assuming all the particles which meet the target scatter then the number N_s that scatter is given by

$$N_s = \sigma |\vec{j}_{inc}|$$

and the number scattering into a small angular subregion is found by differentiating this with respect to solid angle. Therefore

$$dN_s = \frac{d\sigma}{d\Omega} |\vec{j}_{inc}| d\Omega$$

and the differential cross section is obtained according to

$$\frac{d\sigma}{d\Omega} = \frac{dN_s}{|\vec{j}_{inc}| d\Omega}.$$

Inserting all the relevant expressions into the right-hand side gives finally

$$\frac{d\sigma(\theta, \phi)}{d\Omega} = |f(k, \cos\theta)|^2.$$

2.3 The Partial Wave Expansion.

The expression for the angular differential cross section is given entirely in terms of the scattering amplitude. An expression for the scattering amplitude has already been obtained and is given in Equation 2.3. It is often, however, written in the form

$$f(k, \cos\theta) = \sum_{l=0}^{\infty}(2l+1)a_l(k)P_l(\cos\theta).$$

where

$$a_l(k) = \frac{\left(e^{2i\delta_l(k)} - 1\right)}{2ik}.$$

This is the partial wave expansion of the scattering amplitude [7]. It is a series which separates the individual angular momentum components of the scattered wave. The $a_l(k)$ factors are referred to as the partial wave amplitudes. The partial wave amplitudes are a measure of the scattering of each individual angular momentum component of the incoming beam. The partial wave amplitudes may be written as follows

$$a_l(k) = \frac{e^{i\delta_l(k)}\sin\delta_l(k)}{k}$$

by simply isolating the factor corresponding to $\sin\delta_l(k)$ in its complex form. If an expression for the total cross section is then derived, using the formula

$$\sigma = \int |f(k, \cos\theta)|^2 d\Omega,$$

it leads to the following expression

$$\sigma = \frac{4\pi}{k^2}\sum_{l=0}^{\infty}(2l+1)\sin^2\delta_l(k). \tag{2.4}$$

The integral which is required to obtain this is given by

$$\int P_l(\cos\theta)P_l(\cos\theta)\sin\theta d\theta = \frac{2}{2l+1}.$$

The total cross section may therefore be written in the form

$$\sigma = \sum_{l=0}^{\infty}\sigma_l$$

where

$$\sigma_l = \frac{4\pi}{k^2}(2l+1)\sin^2\delta_l(k).$$

The total cross section is given by the sum of each of the partial cross sections σ_l. An incident beam of particles comprised of states of different angular momenta must therefore behave such that each individual angular momentum component scatters independently. Each individual partial cross section has an upper bound, determined by its value when the phase shift is an odd multiple of $\frac{\pi}{2}$, which is given by

$$\sigma_l^{max} = \frac{4\pi}{k^2}(2l+1)$$

These bounds are referred to as a unitarity bounds. The property of unitarity will be considered in more detail in the next chapter. By comparing Equation 2.4 with Equation 2.3, however, the total cross section may be related directly to the scattering amplitude as follows

$$\sigma = \frac{4\pi}{k}\text{Im } f(\theta = 0).$$

This relationship between the total cross section and the imaginary part of the $\theta = 0$, or forward, scattering amplitude is called the optical theorem. It arises because when $\theta = 0$ the Legendre polynomials equal unity. This expression is of particular use since it often avoids the need to perform difficult integrations.

The expression for the scattering amplitude has been derived for processes in which particles have equal energies before and after scattering. A similiar result is obtained for other processes. It can be seen that the phase factor introduced by the potential attaches itself to the outgoing scattered wave. To predict the behaviour of scattering processes it is necessary to say something about the phase shifts which are introduced by the potential. To precisely determine the behaviour of the phase shifts, however, it is necessary to know the form of the potential since the Schrödinger equation needs to be solved in this region so that the term corresponding to $\delta_l(k)$ can be extracted from the expression when the radius is large. Although the exact form of the potential is not known, it is possible, however, to isolate certain aspects of the probable behaviour of the phase shifts for certain scattering phenomena. One such phenomenon for which this may be done is the process of resonance production in particle scattering.

2.4 Resonances.

A resonance is formed when a number of particles combine to give a new short-lived particle state. They are normally identified by forming the invariant mass of a subset of the particles that remain after the interaction. If two particles exist in the initial state and two particles exist in the final state, a resonance is usually represented as shown in figure 2.2 a). The production of a resonance leads to a peak in the cross section since the scattering process prefers to use the state for scattering. Peaks occur at positions where the centre-of-mass energy of the incoming particles equals the mass of an allowed resonance.

Resonance peaks may be interpreted using the partial wave expansion as arising when one of the partial wave amplitudes dominates. As an example, consider the total cross section for π^+-proton scattering which peaks at a pion kinetic energy of 190 MeV [8]. The centre-of-mass energy of the initial state when the pion has this kinetic energy is 1232 MeV. This peak is interpreted as being due to the production of a resonance, referred to as the Δ^{++}-resonance, which then has a mass equal to this energy. The value of the maximum height of the cross section at this point is given by

$$\sigma = \frac{8\pi}{k^2}.$$

Since total angular momentum is equal to $\frac{3}{2}$, which is equal to the spin, or isopsin, of the Δ^{++}-resonance, the orbital angular momentum must be zero. The $l = 0$ component therefore dominates. The phase shift then passes through 90 degrees at this point.

For any value of the phase shift, the exponential factor in the partial wave amplitude may be written as follows

$$e^{2i\delta_l(k)} = \frac{e^{i\delta_l(k)}}{e^{-i\delta_l(k)}}.$$

This may be written as

$$e^{2i\delta_l} = \frac{1 + i\tan\delta_l}{1 - i\tan\delta_l}.$$

The partial wave amplitude is then given by

$$\frac{\left(e^{2i\delta_l(k)} - 1\right)}{2ik} = \frac{1}{2k}\frac{1}{(\cot\delta_l - i)}.$$

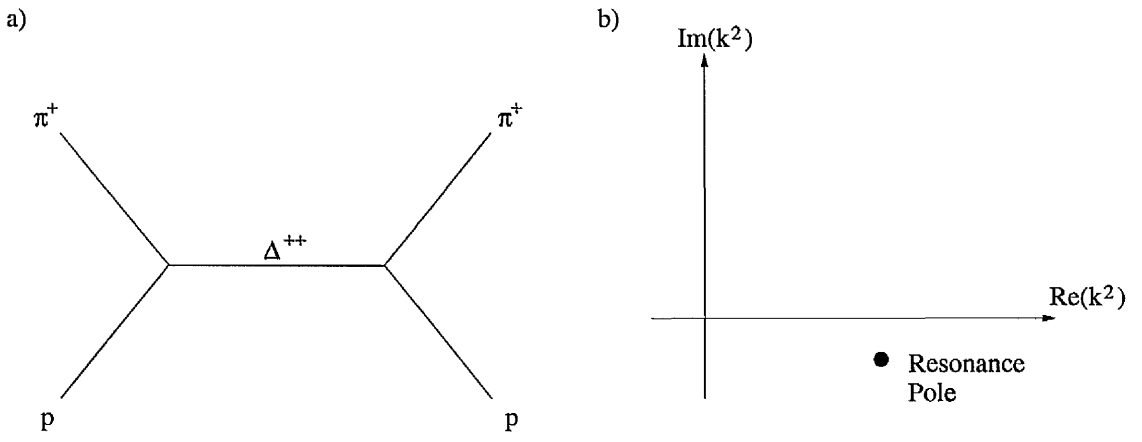

Figure 2.2: A resonance occurs when the initial state particles combine to give a new, short lived state. A resonance may be viewed as a pole in the complex k^2-plane lying just under the positive real axis.

Expanding $\cot\delta_l$ about the position of the peak, where the energy is equal to E_0 and the phase shift is 90 degrees, gives

$$\cot\delta_l = 0 + (E_0 - E)\frac{d(\cot\delta_l)}{dE}\bigg|_{E=E_0}.$$

The first term is equal to zero because $\cot\frac{\pi}{2} = 0$. Setting the value of the differential to be

$$\frac{d(\cot\delta_l)}{dE} = \frac{\Gamma}{2}$$

gives the following expression for the partial wave amplitude

$$a_l(k) = \frac{1}{2k}\frac{\frac{\Gamma}{2}}{(E_0 - E) - i\frac{\Gamma}{2}}.$$

This is the Breit-Wigner formula for the partial wave amplitude in the region of a resonance. The energy at which this occurs must take a real positive value, however, the resonance can be thought of as a pole in the complex energy plane at a position

$$E = E_0 - i\frac{\Gamma}{2}.$$

At this value the denominator becomes equal to zero. Since Γ describes the width of the resonance peak and is typically small the pole lies just below the positive real axis in the complex energy plane (Fig. 2.2 b)).

2.5 The Mandelstam Representation.

The expressions obtained previously for the total and differential cross sections apply to non-relativistic scattering energies. Before these expressions can be compared to the results of the scattering experiments which were performed at relativistic energies the system dependent variables must be replaced by relativistically invariant ones. It will then be possible to predict the behaviour of scattering at high centre-of-mass energies by considering the high centre-of-mass energy limit.

If four particles participate in a particular scattering process it is usual to re-express equations in terms of the Mandelstam variables s, t and u [9]. These are defined as follows

$$\begin{aligned} s &= (p_1 + p_2)^2 \\ t &= (p_1 + p_3)^2 \\ u &= (p_1 + p_4)^2 \end{aligned}$$

where the Mandelstam four-vectors p_1, p_2, p_3 and p_4 are to be used to represent the four-vectors of the particles participating in the scattering process. Each of the Mandelstam four-vectors, however, are defined as being positive when entering the interaction region (Fig. 2.3). Depending on how many of the four particles participating in the interaction leave the interaction region a number of these particle four-vectors will need to be reversed, that is set equal to their antiparticle four-vectors, before they are inserted into the formulae for s, t and u. Consider a process in which two particles come together and two particles leave the interaction region. For simplicity the masses of each of the four participating particles may be taken to be equal. The description of this process in the Mandelstam representation is obtained by first reversing the directions of the two outgoing physical particle four-vectors. Clearly, there are then several different pairs of Mandelstam vectors which can be chosen to represent the reversed particle four-vectors. Consider choosing vectors 3 and 4 to represent the reversed four-vectors of the outgoing particles. The two incoming particles are then represented by vectors 1 and 2. If, for further simplicity, the process is viewed in the centre-of-mass frame, then the two incoming particles have equal energies (E) and momenta of equal magnitude (k). In addition they will approach each other head on so the directions of their momentum vectors

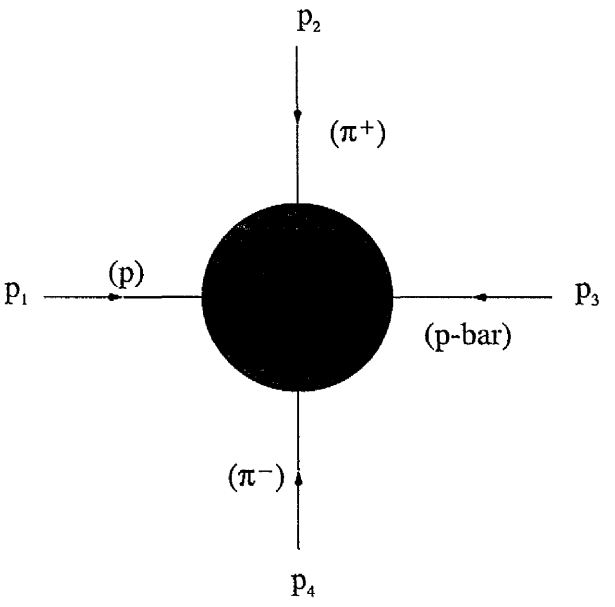

Figure 2.3: If four particles participate in a scattering process the Mandelstam representation may be used to describe the particle vectors. Each of the vectors of the Mandelstam picture are defined as being positive when entering the interation region.

will be exactly opposite. Therefore, the Mandelstam variable s will be given by

$$s = (p_1 + p_2)^2 = 2m^2 + 2p_1 \cdot p_2.$$

Evaluating the scalar product gives

$$s = 2m^2 + 2E^2 + 2k^2.$$

Using the relationship $E^2 = k^2 + m^2$ this gives

$$s = 4(k^2 + m^2).$$

The value of s will always be positive.

In the centre-of-mass frame the two outgoing particles will also have equal energies and momenta of equal magnitude. The centre-of-mass energy is still shared

between two objects of equal mass. The particles come out back-to-back so the momenta also have exactly opposite directions. These three-momenta may be written as $\mathbf{k}'$ and $-\mathbf{k}'$. In addition the magnitude of $\mathbf{k}'$ must also equal the magnitude of $\mathbf{k}$, since the masses of all the particles are equal. If the Mandelstam four-vector 1 is set equal to

$$p_1 = (E, \mathbf{k})$$

so it defines the incoming particle with the positive momentum vector then, since Mandelstam vector 3 is given by the antiparticle four-vector of the physically outgoing particle,

$$p_3 = (-E, -\mathbf{k}').$$

and the value of the Mandelstam variable t is then

$$t = -(\mathbf{k} - \mathbf{k}')^2$$

This simplifies to

$$t = -(2\mathbf{k}^2 - 2\mathbf{k}^2 \cos\theta) = -2\mathbf{k}^2(1 - \cos\theta)$$

where θ is the angle between incoming particle 1 and outgoing particle 3 in the centre-of-mass frame. This variable is always negative. The expression for u in the same way is given by

$$u = -2\mathbf{k}^2(1 + \cos\theta).$$

This quantity is also always negative. When s is positive and both t and u are negative the process is said to be described in the s-channel. By conservation of energy and momentum,

$$p_1 + p_2 = -p_3 - p_4.$$

The s-channel description would therefore also have been obtained if Mandelstam vectors 1 and 2 had been chosen to represent the particles leaving the interaction region.

If instead, however, vectors 2 and 4 are chosen to represent the reversed four-vectors of the particles leaving the interaction region then, using the previous descriptions of the physical particle four-vectors, the value of t will be given by

$$t = (E_1 + E_3)^2 = 4(\mathbf{k}^2 + m^2)$$

and will always be positive. Vectors 1 and 3 now represent the incoming particles. This is the same expression that was obtained for s in the s-channel description. If vector 1 is now taken to be represent the incoming particle of positive momentum as before and vector 4 is chosen to be

$$p_4 = (-E, -\mathbf{k}'),$$

the value of u is

$$u = -2k^2(1 - \cos\theta).$$

Similarly s is given by

$$s = -2k^2(1 + \cos\theta).$$

Since t is positive and s and u are always negative this is the description of the process in the t-channel. The formulae are the same as before but the Mandelstam variables to which they correspond have altered. Note that if vectors 2 and 3 are reversed a u-channel description of the process is obtained which produces a similar outcome. This symmetry is referred to as crossing symmetry. It arises from the equivalence of considering an antiparticle with positive momentum and energy to considering a particle with negative momentum and negative energy, which was first proposed by P. A. M. Dirac. The idea applies in any frame since the Mandelstam variables are relativistically invariant, and also when the particles do not have equal masses. The expressions obtained are more complicated in this case however. There are therefore three ways of describing a single scattering process in which two particles enter and two particles leave the interaction region.

Consider then using the Mandelstam representation to describe the process

$$\pi^+ + p \rightarrow p + \pi^+.$$

This may be described in either the s, t or u-channel. The scattering amplitude will be given by the same expression in each case, with the appropiate letter used to label the three quantities in that channel. Consider the s-channel description of this process such that the incoming proton is represented by vector 1 and the incoming π^+ is represented by vector 2. Which Mandelstam vectors represent which particles is also shown in fig. 2.3. If the different process,

$$p + \bar{p} \rightarrow \pi^- + \pi^+.$$

is now taken, however, and described in the t-channel then vectors 1 and 3 represent the incoming particles. The four Mandelstam vectors may then be chosen in such a way that they correspond to the same particles as they did in the previous process. In addition the process

$$\mathrm{p} + \pi^- \rightarrow \pi^- + \mathrm{p}.$$

will also lead to an equivalent Mandelstam representation if its u-channel description is chosen. Three apparently different processes will therefore be described by the same scattering amplitude. It will be required to make the necessary replacements for s, t and u as explained but their scattering amplitudes will have the same physical behaviours. It is now possible to see why different scattering processes show similarities.

The Mandelstam representation may be used to relate more processes, however, when it is recalled that vectors 1 and 2 could have been initially chosen to represent the outgoing particles in the s-channel description of the reaction

$$\pi^+ + \mathrm{p} \rightarrow \mathrm{p} + \pi^+.$$

Similarly there is a complementary way of obtaining the t-channel and u-channel descriptions. If these equivalent descriptions are also considered then the inverse-antiparticle reactions of those already considered are also obtained. These are the reverse interactions of the previous processes with each particle replaced by its antiparticle. They are given by

$$\begin{array}{lllllll} \pi^- & + & \bar{\mathrm{p}} & \rightarrow & \bar{\mathrm{p}} & + & \pi^- \\ \bar{\mathrm{p}} & + & \pi^+ & \rightarrow & \pi^+ & + & \bar{\mathrm{p}} \\ \pi^- & + & \pi^+ & \rightarrow & \mathrm{p} & + & \bar{\mathrm{p}}. \end{array}$$

In general there are six different reactions all linked to the same scattering amplitude by crossing symmetry. Note that if the first reaction had instead been initially represented in the t-channel the same six crossed reactions would still be obtained. The idea may be extended further by adding, for example, the inverse reactions of all those already obtained to the list. This is equivalent to also adding time reversal invariance. These extensions are not however considered here.

Consider finally then replacing the frame-dependent variables by Mandelstam variables in the partial wave expansion. The s-channel is chosen here as the basis channel, however the labels may be swapped for scattering amplitudes in other

channels. At high energies a particle's mass is negligible in comparison to its momentum and the approximation

$$E = k$$

is good. Therefore, s simplifies to

$$s = 4k^2.$$

Substituting s into the equation for t and rearranging gives

$$\cos\theta = 1 + \frac{2t}{s}.$$

Since in general

$$s + t + u = m_1^2 + m_2^2 + m_3^2 + m_4^2.$$

where the masses m_1, m_2, m_3 and m_4 correspond to masses of the four participating particles, only two of the Mandelstam variables are independent. It is therefore enough to express the scattering amplitude as a function of just two of the Mandelstam variables. For scattering processes described in the s-channel the scattering amplitude in terms of the Mandelstam variables is given by,

$$f(s,t) = \sum_{l=0}^{\infty}(2l+1)a_l(s)P_l(1+\frac{2t}{s}).$$

Of interest for the purposes of this analysis is the differential cross section $d\sigma/dt$. This may be easily related to the angular differential cross section. The angular differential cross section is given by

$$\frac{d\sigma}{d\Omega} = \frac{1}{2\pi}\frac{d\sigma}{d(\cos\theta)}.$$

Using the expression for t in the s-channel

$$dt = 2k^2 d(\cos\theta)$$

and the relationship between the angular differential cross section and $d\sigma/dt$ becomes

$$\frac{d\sigma}{d\Omega} = \frac{k^2}{\pi}\frac{d\sigma}{dt}$$

The differential cross section $d\sigma/dt$ therefore essentially behaves as

$$\frac{d\sigma}{dt} \sim \left|\frac{f(k,\cos\theta)}{s^{0.5}}\right|^2$$

Note that, in the s-channel, t represents the momentum transfer squared between particles 1 and 3. If it is now attempted to extract the high energy behaviour, by considering the limit ($s \to \infty$), the partial wave amplitude is found to actually diverge. This leads to an infinitely large scattering amplitude, and therefore infinitely large predictions for differential and total cross sections. This is, however, due to the fact that the series diverges and not necessarily because the scattering amplitude actually is infinite in this limit. Some work will need to be done to extract expressions for relativistic scattering.

2.6 Extension to Relativistic Scattering Theory.

Mandelstam was able to extend the idea of crossing symmetry further such that all the different descriptions of the scattering process could be extracted from a single expression for the scattering amplitude, written for example in terms of the s-channel variables, without the need for swapping over labels. To do this he considered unphysical values of energy and momentum.

In general the four particles participating in the scattering process will all have different energies and momenta when viewed in some general frame of reference. The general process is shown in figure 2.4 where the labels correspond to the physical particle four-vectors. P_1 and P_2 are the physical four-vectors of the incoming particles in the s-channel. The expressions for the Mandelstam variables in the s-channel are therefore

$$\begin{aligned} s &= (P_1 + P_2)^2 \\ t &= (P_1 - P_3)^2 \\ u &= (P_1 - P_4)^2 \end{aligned}$$

since the outgoing physical particle four-vectors have to be reversed. Suppose now, however, that the incoming particle with four-vector P_2 enters with a momentum four-vector given by $P_2 = -P_4$. The energy of this particle will then be negative and the direction of its momentum will be exactly opposite to that of the outgoing particle described by P_4. Its four-vector is therefore given by $P_2 = (-E_4, -k_4)$. Clearly this does not correspond to a physical situation since this particle cannot physically enter the interaction region with a negative energy. If the outgoing particle labelled

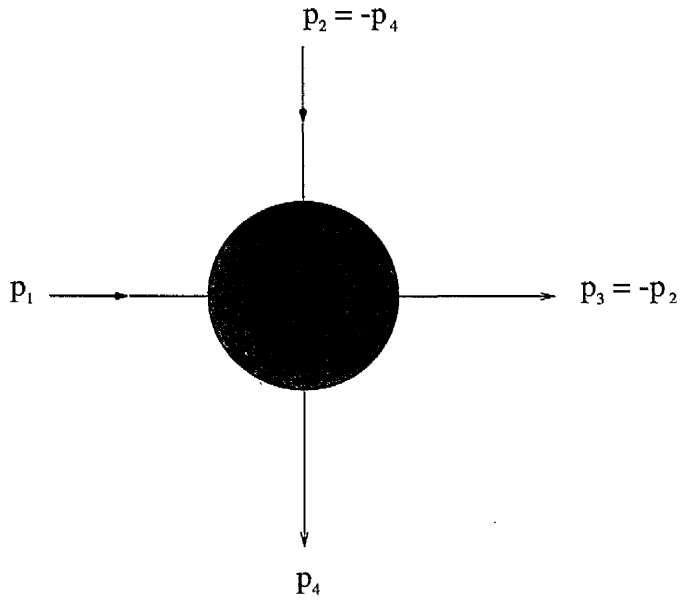

Figure 2.4: If two of the four particles participating in the scattering process may be taken to enter or leave with unphysical values of energy, their four-vectors given as shown, then a single scattering amplitude may be used to extract all of the different channel descriptions of the scattering process.

by P_3 is also considered to leave the interaction region with a negative energy, such that $P_3 = -P_2$, then the expressions for the Mandelstam variables in the s-channel become

$$\begin{aligned} s &= (P_1 - P_3)^2 \\ t &= (P_1 + P_2)^2 \\ u &= (P_1 - P_4)^2 \end{aligned}$$

The value of t now corresponds to the centre of mass energy squared. This is exactly what would have been obtained if it had been decided to view the process in the t-channel. Therefore by considering particles entering the interaction region with unphysical negative energies, and also those particles leaving the interaction region, it is possible to retrive the expressions for the other channels from one expression for the scattering amplitude. A single expression for the scattering amplitude would then be used to describe each of the three equivalent ways of viewing a single scatter-

ing process and also each of the six different processes related by crossing symmetry. In the example of the previous section the two incoming particles will no longer enter in equal and opposite directions when unphysical energies are considered. The act of crossing therefore alters the relativistic frame of reference.

To find out if it is possible to use unphysical particle vectors it is necessary to return to the general solutions to the Schrödinger equation and ask if solutions may be found for unphysical values of energy. Of particular interest is the dependence of the wavefunction on the magnitude of the wavevector **k**. The dependence of the wavefunction on k arose from the solutions to the radial equation. Solutions to the radial equation, however, may also be found for negative values of k^2 and for complex values of k^2. The partial wave expansion may therefore be considered valid for negative real values of k^2 and for complex values of k^2 even though only positive real values have a physical interpretation. This implies that k itself may be in general considered to be a complex number. The three Mandelstam variables may now be considered in general complex since they are each related to complex k^2. To pull out an s-channel description of a scattering process from the scattering amplitude a region where the real part of s is positive and the real parts of t and u are negative must be considered. To extract the t-channel description a region where the real parts of s and u are negative and the real part of t is positive must be considered.

It should be noted that the expression for s now remains fixed. When the real part of k^2 is equal to some negative value $-k_0^2$, s becomes equal to

$$s = s_0 = -4k_0^2 + 4m^2$$

plus some imaginary term. If k_0^2 is large enough then the real part of s_0 will be negative. The real part of s then corresponds to the value of the momentum transfer squared of a scattering process viewed in the t-channel such that for example

$$s_0 = -2k_1^2(1 - \cos\theta_t)$$

Similarly the expression for t is fixed and it is necessary to consider this at some other value of k^2 such that t independently equals

$$t = t_0 = 4k_1^2 + 4m^2$$

and therefore corresponds to the centre-of-mass energy squared in the t-channel. At higher energies where the masses of the participating particles become negligible

this corresponds to choosing the value of t such that

$$\cos\theta_t = 1 + \frac{2s_0}{t_0}.$$

One therefore considers different regions in the complex k^2-plane (or the complex s-plane, for example).

An alternative method of extending this idea to higher values of centre-of-mass energy now appears. To consider a large value of the centre-of-mass energy t in the related t-channel, a value of t corresponding to a large value of k_1^2 in the t-channel needs to be extracted from the s-channel expression for t. This means that a large value of $t_0 \to \infty$ needs to be selected. The formula for t in the s-channel is given by

$$t = -2k^2(1 - \cos\theta)$$

To make this large and positive it is possible to choose a value of k^2 which has a large negative real part. The value of s would then independently have to be fixed at some smaller negative value so that a corresponding high centre-of-mass scattering process at some reasonably small value of momentum transfer were selected. This corresponds to independently selecting an alternative value of k^2 which has a smaller negative real part.

This method of extracting the high energy limit was approached in the theory of dispersion relations [10]. In the theory of complex integration it is known that the value of the integral of a complex function is equal at all points within the contour around which the integration is performed. If the scattering amplitude could then be written in the form

$$A(s_0, t) = \int \frac{A'(s', t)}{s_0 - s'} ds'$$

it would then be possible to argue that the scattering amplitude is equal everywhere inside the contour. The low energy description of the scattering process would then be equivalent to the high energy description. The result just depends on the singularities chosen to lie inside the contour. The integrand has a singularity at $s = s_0$ to fix the value of s at some negative number. A simple example of a possible contour is shown in figure 2.5. When the contribution from the circular part of the contour tends to zero as the radius tends to infinity, the complex integral reduces to just an integral from $-\infty$ to $+\infty$ along the real axis. This then equals a factor

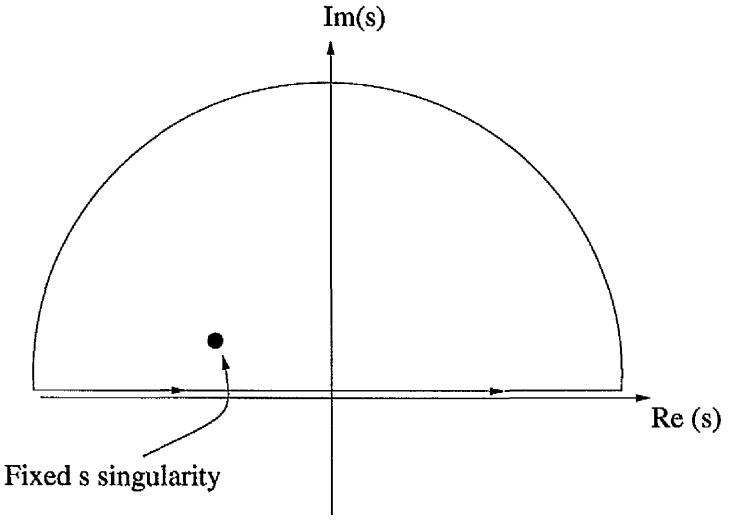

Figure 2.5: In an ideal case a contour could be set up in the complex s-plane and integrated over to give a set of dispersion relations for the scattering amplitude. In practice many more singularities are present in the complex s-plane.

$2\pi i$ multiplied by the sum of the contributions, or residues, from each singularity inside the contour. When this integral is performed it reduces to a set of dispersion relations, a pair of expressions relating the real part and imaginary parts of the scattering amplitude. A great deal of work in the field of dispersion relations has been completed, however, dispersion relations in the field of particle physics are in practice very complicated objects. In general the partial wave expansion contains other singularities in the complex s-plane, related to those discussed in terms of the complex k^2-plane. The positions of some of these singularities will depend upon which resonances occur in the scattering process. This depends on the potential which gives rise to the scattering force. Although the process of absorption has not been considered here other poles, which arise when the target and projectile combine to form a stable bound state, may also be present. In addition, it is not always possible to argue that the contribution from the circular part tends to zero as the radius is increased and the integration then leads to more complicated subtracted dispersion relations.

2.7 Regge Poles and the Asymptotic Limit.

An alternative way of obtaining the high energy limit is required. Consider once again extracting a large positive value of t from the expression for t in the s-channel. If the value of k^2 is now fixed at some small negative value, the high energy region may be extracted by letting $\cos\theta$ tend to negative infinity, or equivalently $|\cos\theta| \rightarrow \infty$. The value of s may still be independently fixed at some small, negative value as before. For $\cos\theta$ to take unphysical values the scattering angle must be allowed to become complex. The value of $\cos\theta$ itself then also becomes complex. Since solutions to the Schrödinger equation may also be obtained for complex values of $\cos\theta$ it is possible to argue that the partial wave expansion is valid for unphysical values of k^2 and $\cos\theta$ even though only positive real values of energy and scattering angles in the range $0° < \theta < 180°$ have physical interpretations. To extract the behaviour of the scattering amplitude in a related channel the real parts of complex s and t are once again considered.

It is the convention in experimental particle physics to describe processes in the s-channel. To arrive at a result which is already written in terms of the s-channel variables a partial wave expansion written in the t-channel is now considered, from which the description of a high energy s-channel process is extracted. The value of t is then always negative. This is because it labels a momentum transfer squared and not because t must always be negative. The procedure may be applied such that a t-channel scattering amplitude which refers to a high centre-of-mass energy process is obtained from an s-channel scattering amplitude (this is done, for example, in reference [11]). The measured value of t would then always be positive because it would label the centre-of-mass energy squared. In addition it should be noted that no statement needs to be made about what takes place in the interaction region. A process, for example, in which the two incoming particles combine together to form a resonance may be viewed in any channel. There is only a relationship between what occurs in the interaction region and the channel once it has been decided to view this process in a particular channel. If the t-channel is chosen to represent the resonance process then a particle exchange diagram represents the s-channel process.

The partial wave expansion in the t-channel is given by

$$f(s,t) = \sum_{l=0}^{\infty}(2l+1)a_l(t)P_l(\cos\theta_t).$$

If $\cos\theta_t$ is now allowed to tend to infinity, however, in the expression as it stands, the series also diverges. This problem was however solved by Italian physicist T. Regge who returned to the general solutions to the free-particle Schrödinger equation and took the unusual step of considering complex values of angular momentum [12].

The phi-dependence of the eigenfunctions was removed in the derivation of the partial wave expansion because scattering experiments often show no dependence on the azimuthal angle phi. Since the phi-dependence is to be removed anyway Regge wrote the general solutions as a product of a function that depends only on the radius r and a function that depends only on theta. The same procedure for separating the problem into two equations, one that contains the radial dependence and one that contains the theta dependence may be repeated. When the theta equation is solved, however, there is now no restriction on the constant, since this arose from the solution to the phi-equation. Solutions to the theta equation may then be found for continuous and complex values of angular momenta l. They are the hypergeometric functions $H(l, \cos\theta_t)$. The hypergeometric functions reproduce the Legendre polynomials for positive, negative integer and zero values of the angular momentum quantum number.

The partial wave expansion may therefore be considered valid for all l, except where there are singularities in the complex l-plane. The sum over discrete values of l is now be replaced by a contour integral over complex and continuous values of angular momentum and is given, for positive, negative integer and zero values of angular momentum, by

$$f(s,t) = \frac{i}{2}\int_C dl(2l+1)\frac{a(l,t)}{\sin\pi l}P(l,-\cos\theta_t)$$

where

$$\cos\theta_t = 1 + \frac{2s}{t}.$$

The new partial wave expansion reproduces the previous expression when positive, negative integer or zero values of angular momentum are considered. This is ensured by a factor $\sin\pi l$ in the integrand which has zeros at positive and negative integer values of l and zero l. The contour of integration is chosen as shown in figure 2.6. It then only selects positive integer and zero values of angular momentum. A contribution from each of the singularities is then produced when the integration is performed, giving a series in l. It is assumed that no additional singularites arising

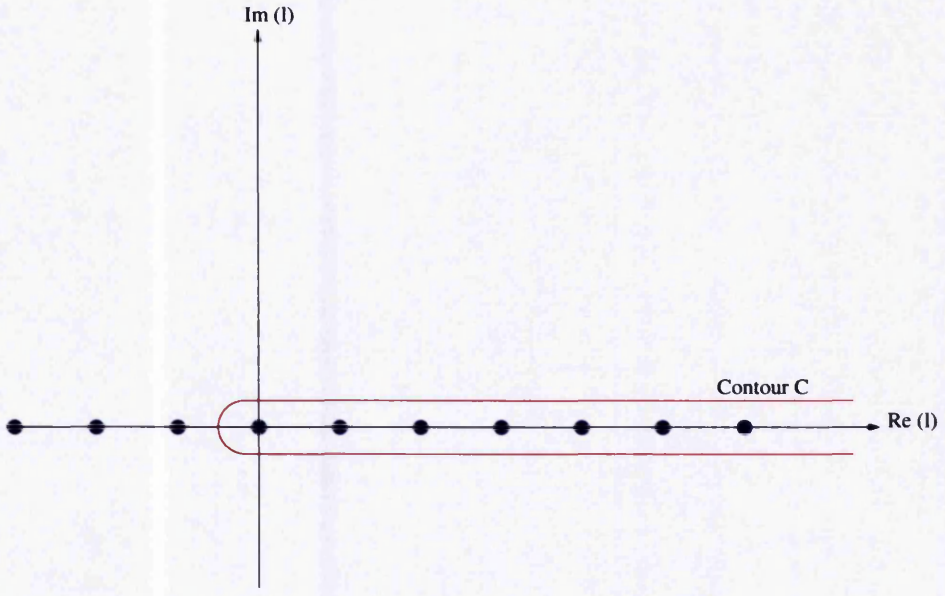

Figure 2.6: If angular momentum l is allowed to become a free, continuous parameter, which may be real or complex, the sum in the partial wave expansion is replaced by a complex integral which is performed over a contour surrounding a series of poles on the real axis. For physical reasons only the poles corresponding to positive angular momenta are surrounded.

from the partial wave amplitudes lie inside the contour. The integral has been divided by the additional factor

$$2i(-1)^{l+1}$$

which is required since each of the poles which lie inside the contour on the real axis contribute this factor multiplied by the equivalent term in the partial wave expansion. The factor $(-1)^l$ is taken care of by noting that

$$P_l(-\cos\theta) = \frac{P_l(\cos\theta)}{(-1)^l}.$$

The partial wave amplitudes are now also functions of complex and continuous angular momentum.

It is now possible, however, to change, or deform, the path of integration to a new contour without changing the result, provided the new contour does not

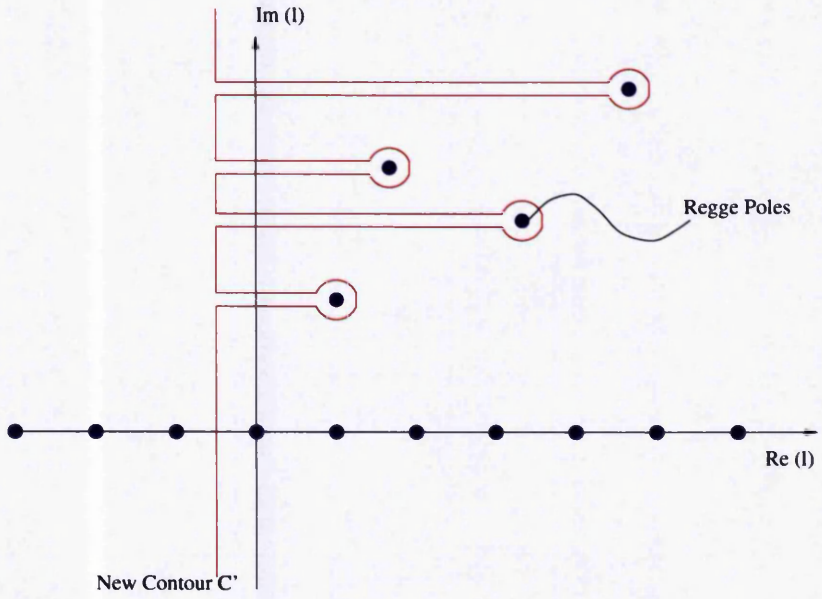

Figure 2.7: It is possible to change, or deform, the contour of integration to any other contour provided no additional poles are contained inside the contour. The additional poles which must be avoided are referred to as Regge poles.

contain any additional poles or branch cuts. Consider deforming the contour of integration to a new contour C' which lies along the line Re $l = -\frac{1}{2}$. The contour returns via a half-circle closed in the right-hand half plane which has an infinite radius. Singularities in the partial wave amplitudes, which may be interpreted as resonances in a similar way to which they were interpreted for the complex energy plane, now lie in this region and must be avoided. These poles in the partial wave amplitudes are referred to as Regge poles [13]. The new contour of integration will look something like that shown in fig. 2.7. The poles of the partial wave amplitudes are functions of t and occur at angular momentum values of $l = \alpha_i(t)$ for $i = 1, 2, 3, \ldots$.

Integrating around the new contour gives the following expression

$$f(s,t) = \frac{i}{2}\int_{-\frac{1}{2}-i\infty}^{-\frac{1}{2}+i\infty} dl \frac{(2l+1)a(l,t)P(l,-\cos\theta_t)}{\sin\pi l} + \sum_i \frac{\pi}{2}(2\alpha_i(t)+1)\frac{\beta_i(t)P_{\alpha_i(t)}(l,-\cos\theta_t)}{\sin\pi\alpha_i(t)}.$$

Here the β factors are the residues of each Regge pole. This expression gives the

same result as before since the contour only contains the poles along the real angular momentum axis. Changing the path of integration in this way was first considered by Watson in 1918 [14] and later by Sommerfeld in the theory of the propagation of radio waves [15] and is therefore referred to as a Sommerfeld-Watson transform.

The asymptotic limit $\cos\theta_t \rightarrow -\infty$ may be now taken. The Legendre polynomials have the following behaviour as $\cos\theta_t$ tends to negative infinity,

$$P_l(z = -\cos\theta_t) \stackrel{z\rightarrow\infty}{\longrightarrow} |z|^l.$$

The argument z is infinite in the high energy limit. The Legendre polynomials are therefore given by $(\cos\theta_t)^l$. When this is now inserted into the expression obtained by integrating around the new contour, since the integral is carried out along the line $\mathrm{Re}\, l = -\frac{1}{2}$, the first term will be suppressed by a factor $(\cos\theta_t)^{-\frac{1}{2}}$ in comparison to those contributions from the Regge poles. The first term of the expression is often referred to as the background integral. The dominant term will arise from the Regge pole with the largest real angular momentum value. This is the pole furthest to the right in the complex plane and is referred to as the leading Regge pole.

The scattering amplitude is therefore given by

$$f(s,t) \sim \frac{\pi}{2}(2\alpha_i(t)+1)\frac{\beta_i(t)}{\sin\pi\alpha_i(t)}(\cos\theta_t)^{\alpha_i(t)}.$$

By noting that $\cos\theta_t$ behaves essentially as

$$(\cos\theta_t)^{\alpha_i(t)} \sim s^{\alpha_i(t)}$$

in the high centre-of-mass energy (high s) limit, the amplitude may be now written in the following form

$$f(s,t) \sim \frac{\pi}{2}(2\alpha_i(t)+1)\frac{\beta_i(t)}{\sin\pi\alpha_i(t)}s^{\alpha_i(t)}.$$

Here s represents the centre-of-mass energy of the related process which has been extracted from the scattering amplitude by crossing. The value of t is now negative and corresponds to some value of the momentum transfer squared. As the centre-of-mass energy is increased the position of the Regge poles move. They trace out a path in the complex angular momentum plane which is referred to as a Regge trajectory. The Regge poles may pass through several physical positive real angular momentum values as they trace out their trajectories.

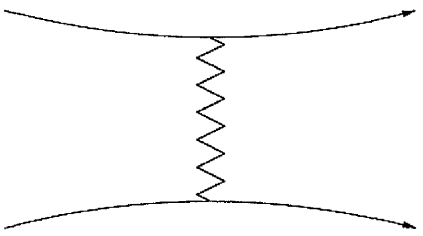

Figure 2.8: The force which gives rise to scattering may be viewed as being due to the exchange of a superposition of all the particles that can appear as resonances in the scattering process. The superposition of particle states is referred to as a Reggeon.

If the residue of the pole can now be written in the form

$$\beta_i(t) = \frac{\gamma_1(t)\gamma_2(t)}{\Gamma(\alpha_i(t))}$$

then it is possible to interpret the scattering amplitude as describing the exchange of an object between the particles participating in the scattering process as shown in figure 2.8 [16]. This object is called a Reggeon and is given by some superposition of several particle resonance states. This is the explanation for the origin of the scattering force in Regge theory. Exactly which processes the resonances may appear in will be discussed later. The function $\Gamma(\alpha_i(t))$ equals zero at negative integer values of its argument.

2.8 The Pomeron

The formula for the scattering amplitude in the asymptotic limit may now be used to predict the behaviour of the differential and total cross sections. The differential cross section is given by [11],

$$\frac{d\sigma}{dt} \sim \left|\frac{f(s,t)}{s}\right|^2 \sim s^{2\alpha_s(t)-2}.$$

The total cross section σ is then obtained by integrating this over all solid angles. Alternatively, using the optical theorem, it is given by

$$\sigma = \frac{f(s, t=0)}{s} \sim s^{\alpha_1(t=0)-1}.$$

The behaviour of both the differential and total cross sections are therefore determined by the leading Regge pole.

It may appear unusual at this stage that the different processes all related to the same scattering amplitude will scatter due to the exchange of the same Reggeon. This would imply that the resonances that may be formed in each scattering process would be the same. In section 2.5 the process

$$\pi^+ + \mathrm{p} \rightarrow \mathrm{p} + \pi^+$$

was related to five other scattering processes. In section 2.4 a resonance that may be produced in this process was identified as the Δ^{++}-resonance. This resonance can clearly not appear, however, in the related t-channel process

$$\mathrm{p} + \bar{\mathrm{p}} \rightarrow \pi^- + \pi^+.$$

since it would violate conservation of charge. Charge conservation has not however been enforced anywhere in this derivation and the positions of the resonance poles only depends upon the mass of the resonance. The resonance in this process is the Δ^0-resonance which has essentially the same mass as the Δ^{++}-resonance. Similarly resonances in the other processes related by crossing symmetry are

$$\begin{array}{ccccccccc}
\pi^- & + & \mathrm{p} & \rightarrow & \Delta^0 & \rightarrow & \bar{\mathrm{p}} & + & \pi^- \\
\pi^- & + & \bar{\mathrm{p}} & \rightarrow & \overline{\Delta^{++}} & \rightarrow & \bar{\mathrm{p}} & + & \pi^- \\
\bar{\mathrm{p}} & + & \pi^+ & \rightarrow & \overline{\Delta^0} & \rightarrow & \pi^+ & + & \bar{\mathrm{p}} \\
\pi^- & + & \pi^+ & \rightarrow & \Delta^0 & \rightarrow & \mathrm{p} & + & \bar{\mathrm{p}}.
\end{array}$$

The antiparticles of the Δ-resonances have the same mass as their particle partners. Each process therefore produces one charged version of the Δ-particles. The different charged versions of the Δ-resonance were also considered as different versions of the same particle in the later development of the quark model. Since the mass of the neutron is essentially equal to the mass of the proton it is expected that pion-neutron scattering will also have a similar description. The other two charged versions of the Δ-resonance were therefore also combined with the two already discussed.

In the case of the strong interaction there is an additional complication which arises due to the fact that only odd or only even angular momentum states can be formed as resonances from any two initial state particles. This follows from the conservation of angular momentum, or more specifically isopin, which was introduced in the field of nuclear physics so that the proton and the neutron, which have essentially equal masses, could be treated as two charged versions of the same particle. The Δ-resonances may also be interpreted in this way. The strong interaction is then independent of charge, and separate from the electromagnetic force. In scattering due to the strong interaction it must therefore be ensured that only even isospin resonances or only odd isospin resonances, depending on the initial state particles, are involved. To incorporate conservation of isospin the partial wave amplitudes must be separated such that one contains poles for only odd angular momentum resonances and the other only poles for even angular momentum resonances.

These two functions are written as $a^{\eta=+1}(l,t)$ and $a^{\eta=-1}(l,t)$ and are labelled by their signature factor (η), which is positive for even angular momenta [17]. This slightly alters the expression for the asymptotic behaviour of the scattering amplitude as follows

$$f(s,t) \longrightarrow \frac{(\eta + e^{-i\pi\alpha(t)})}{2}\beta(t)s^{\alpha(t)}.$$

The extra factor equals unity when the resonance may be produced and zero when the resonance would violate conservation of isospin.

To complete the predicted expressions for the total cross section it is necessary to insert the behaviour of the function $\alpha(t)$. It might be expected that the behaviour of this function may be deduced by considering the angular momentum values of the allowed resonances of a particular scattering process. A plot of total angular momentum as a function of mass squared for all particles possessing the same quantum numbers as the Δ-resonances is shown in figure 2.9. Since the spin, or isospin, of the Δ-resonances is 3/2 the first state corresponds to an angular momentum of zero. The states then step up in units of 2 as expected. The Δ-resonances are represented by the first point on the trajectory. Diagrams of this kind were first considered Chew and Frautschi and are referred to as Chew-Frautschi plots [18]. A straight line relationship is in fact obtained for almost all particle groups plotted in this way.

In the process of extracting the high energy behaviour t initially labelled the

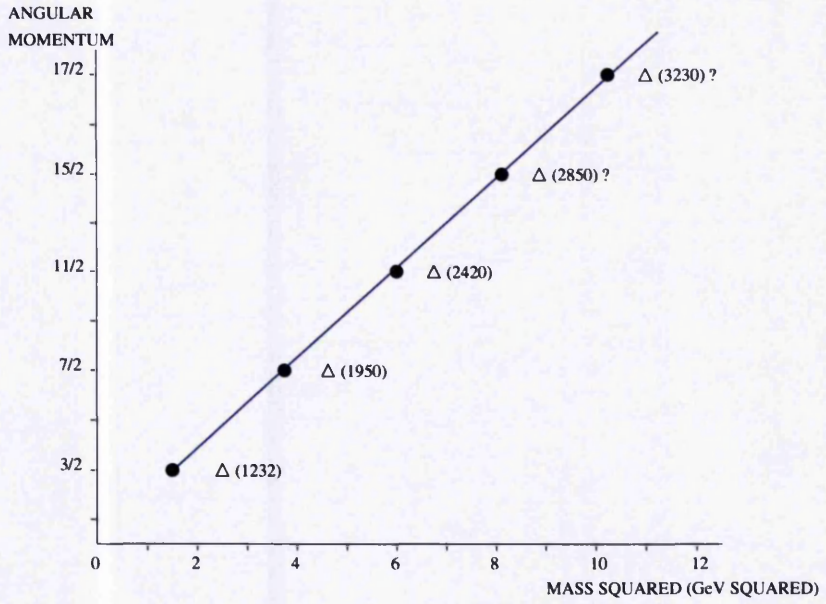

Figure 2.9: Particles possessing the same quantum numbers may be represented on a Chew-Frautschi plot. States with Baryon number 1, strangeness 0, positive parity and isospin 3/2 give a similar straight line dependence as is observed for other particles grouped together by their properties.

centre-of-mass energy squared (see fig. 2.9) and was forced to become negative where it then labelled the momentum transfer squared. This straight line dependence may be used to give predictions for measured cross sections in momentum transfer squared provided the function $\alpha(t)$ extrapolates into the region of negative t. The continuation of the function into negative t has been experimentally verified for certain scattering processes [19]. Regge showed that as the value of t is varied, the position of a Regge pole will move in the complex angular momentum plane tracing out a Regge trajectory. In the region of positive t resonances may appear and t labels a centre-of-mass energy. As the pole passes from positive t to negative t, Regge showed that the pole continues to trace out a smooth trajectory. At negative values of t the pole may pass through several real negative integer values of angular momentum. No resonance can appear at negative t, however, since the mass of the resonance would have to be complex so that, when squared, it gives a negative result. To account for this the scattering amplitude is therefore forced to fall to zero, or

decouple, at these angular momentum values. This is ensured by the $\Gamma(\alpha_i(t))$ factor in the expression for the residue of a Regge pole (and also the signature factor).

The t dependence of a Regge pole may therefore be described for positive and negative t as follows

$$\alpha(t) = \alpha'(t)t + \alpha(t = 0)$$

This means that the scattering amplitude is given by

$$f(s,t) \rightarrow s^{\alpha_1'(t)t+\alpha_1(t=0)}.$$

Therefore the differential cross section is essentially given by

$$\frac{d\sigma}{dt} \sim s^{2\alpha_1'(t)t+2\alpha_1(t=0)-2}$$

and the total cross section is

$$\sigma \sim \frac{f(s,t=0)}{s} = s^{\alpha_1(t=0)-1}.$$

All observed Regge trajectories, formed by considering particles with identical internal quantum numbers, intercept the angular momentum axis at angular momentum values below one. This means that all total cross sections are expected to be falling at some fixed value of the centre-of-mass energy squared s. The typical form of a total elastic cross section is shown for proton-proton and proton-antiproton scattering in figure 2.10 [20]. Here the x-axis corresponds to the centre-of-mass energy. The cross section falls initially as s increases. This suggest that the pole furthest to the right has an intercept of 0.5475. The cross section however begins to rise at higher centre-of-mass energies since the position of the Regge poles have moved in the complex angular momentum plane and a new trajectory now dominates. The leading Regge pole must now have changed to one with an intercept of 1.0808. No trajectory, however, formed from the list of known particle states has an intercept greater than unity. The good agreement at lower centre-of-mass energies however suggests that there may be a family of particles made up from states that have not been detected.

It is interesting to note that the same rise in the total cross section is often repeated in other experiments. This suggests that the same particle family often becomes responsible for the scattering force at high energies (above about 100 GeV), regardless of the properties of the particles which participate in the scattering

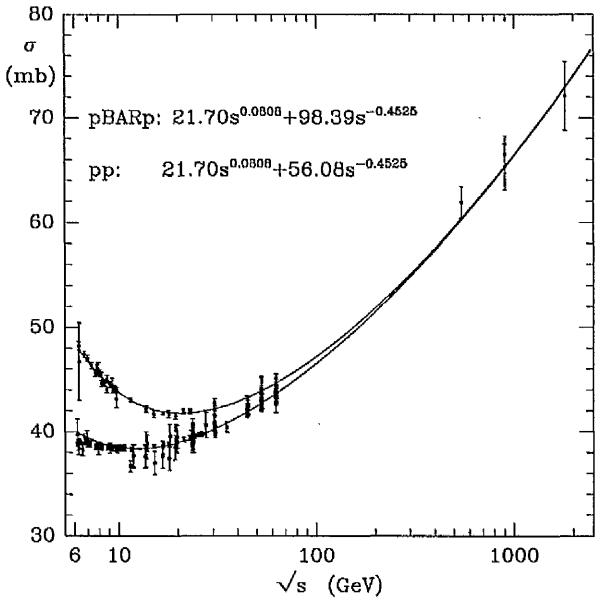

Figure 2.10: The total cross sections for proton-proton and proton-antiproton scattering as a function of centre-of-mass energy have similar behaviours to each other and to many other cross sections measured for different scattering processes.

experiment. Since one version of each particle member of this family must be formed as a resonance in the scattering process, at high energies the only properties that the particles belonging to this family may have are those of the vacuum. This was more rigourously proven by Russian physicist I. Y. Pomeranchuk in 1956 [21] and similarly by Foldy and Peierls [22]. Pomeranchuk was also able to demonstrate that the trajectory must be an even signature trajectory. The states would therefore step up in units of $l = 2$ on a Chew-Frautschi plot, starting with an angular momentum value of 2. The new set of particle states, with Regge intercept greater than 1, is referred to as the pomeron. The gradient of the trajectory may be extracted from fits to differential cross sections and is about 0.25 $\mathrm{GeV}^{-2}\mathrm{c}^{-2}$.

Chapter 3

Perturbative QCD and the Pomeron.

An analysis of the region outside of that which the potential influences yields a great deal of information concerning the behaviour of particle scattering. At higher centre-of-mass energies the member states of the pomeron often become responsible for the scattering force. At these energies it might be suspected that constituent-constituent interactions are occuring. If those particles which participate in scattering processes which tend to the pomeron trajectory all have similar constituents, then an underlying constituent-constituent interaction would explain why these cross sections tend to the same gradient regardless of the external properties of the participating particles (The De-Broglie wavelengths of the participating particles are also shorter at higher energies). To proceed further it is therefore necessary to say something of the likely structure and constituents of strongly interacting particles which might give rise to such a high energy scattering behaviour. It will then be possible to say something of the region close to the target which the potential influences.

It has already been mentioned that the four different charged versions of the Δ-resonances have very similar masses. This method of grouping different particles together in fact gives many such particle sub-groups and suggests that some states may have, for example, four different charged versions, others three, some

two and sometimes only a single charged version appears. Since at high energies the strong interaction is expected to be independent of charge, which is a property of the electromagnetic interaction, it is tempting to argue that the different charged particles that make up a group are effectively identical particles as far as the strong interaction is concerned. Only one state with one mass is of significance.

The Δ-resonances form one such group and have a total isospin of 3/2. The third component of isospin may therefore take the values -3/2, -1/2, 1/2 and 3/2. It is possible to identify each of these different isospin states with one of the four different charged versions of the Δ-resonance. Any constituents that the Δ-resonances may have would therefore have to be, at least partly, fermionic, so that the half-integer values of the third component of isospin are reproduced by the constituents. Fermionic particles are able to take spin up or spin down states, corresponding to third components of isospin of 1/2 and -1/2 respectively. During the 1960s, M. Gell-Mann developed a model in which three identical constituents form the strongly interacting particles of half-integral isospin, referred to as baryon states. In doing so he assumed that these particles do indeed have constituents. Since these constituents are fermionic, the Pauli exclusion principle prevents two of these three particles from occupying the same state at the same time unless one of them is in an isospin-up state and the other is in an isospin-down state. The third constituent then occupies a different quantum energy level. The Δ-resonances therefore have three identical constituents and different combinations of the isospin states that may be formed from these constituents are identified with the four different versions of the Δ-resonances. Clearly the constituents must also reproduce the charge of the larger particle state. A fractional charge of $\frac{2}{3}$e was later assigned to constituents in the up state and a charge of $-\frac{1}{3}$e was assigned to constituents in the down state to preserve this.

Charge, however, has long been believed to be quantised in units of the electron charge e. The introduction of fractional constituent charges would represent a move away from this idea. In 1998 the Nobel prize in physics was awarded to R. Laughlin, H. Störmer and D. Tsui for discovering that electrons, which have integral charges, acting together in strong magnetic fields can form new types of 'particles', with charges that are fractions of electron charges [23]. Clearly the idea that integral charge constituents could somehow reproduce the net integral charges of the large particle states via their interactions with each other cannot be ruled out.

The approach, with the same constituents, may be applied to many baryonic sub-groups. A complication, however, arises when one attempts to apply the idea to particles such as the Λ for which the main decay mode is

$$\Lambda \rightarrow \mathrm{p} + \pi^{-}.$$

This decay process occurs with a lifetime of the order of 10^{-10} seconds which is unusually long in comparison to typical decays via the strong interaction. It is more typical of decays via the weak interaction. Since there are many lighter particle states which the Λ could strongly decay to without appearing to violate any known conservation laws, something must be preventing the Λ from strongly decaying, perhaps a new conservation law. To account for this Gell-Mann allowed the constituents to exist in a third fermionic isospin state, essentially a second type of isospin down state, so that three fermions may then occupy the same energy level. Since this third fermionic isospin state would suggest a previously unobserved type of spin structure was operating at the level of the constituents it was referred to as the strange state. It may, however, then be argued that a strange state conservation law, related to the conservation of isospin, forces certain particles to decay primarily via the weak interaction, when they would normally be expected to decay primarily via the strong interaction. Within the framework of this model the isospin-wavefunction describing strong interaction processes possesses SU(3) symmetry.

Calculations approximating the masses of the constituents in the three states, however, suggest that, although the masses of the up and down states are very similar, the mass of the strange state may not be degenerate with the other two. It could be the case, therefore, that a second type of fermionic constituent exists, with a typically larger mass [24]. If more than one of the larger type constituents are present inside a larger net-particle state then these too are required to be able to exist in isospin-up and isospin-down states to prevent problems with the Pauli exclusion principle. The isospin-up and isospin-down states of the larger mass constituents are distinguished from the isospin-up and isospin-down states of the smaller mass constituents with the names charm (c) and strange (s) respectively. Charm or strange conservation may then still be used to explain why certain particles decay primarily via the weak interaction, when there would normally be no reason why they would not decay primarily via the strong interaction. In this case the number of larger type constituents is preserved in a strong interaction process.

The masses of the charm and strange state, however, may also be too different to treat them as a degenerate particle pair and, although baryons which contain more than one larger constituent in the charm state are predicted within this model, only charmed baryons which, within this model, contain a single charmed state have been discovered. It is possible that particles corresponding to higher charmed states do not exist. A third type of constituent, of typically larger masses still, has also been included, once again to account for decay modes which proceed unusually slowly, but where charm and strange conservation would also not be violated. Its isospin-up and isospin-down states are distinguished from the previous ones with the names top (t) and bottom (b) respectively, although truth and beauty are also common. At present, therefore, up to three different types of constituent may be used to make predictions concerning the behaviour of high energy scattering processes. Each may be able to exist in two different isospin states. This may be represented as follows

$$\begin{pmatrix} u \\ d \end{pmatrix} \begin{pmatrix} c \\ s \end{pmatrix} \begin{pmatrix} t \\ b \end{pmatrix}$$

Alternatively, for example, the up, down and strange states may be taken to be three different 'spin' states of the same particle. The six different isospin states are referred to as quark states. Each different type of constituent is referred to as a quark generation. The procedure may be applied to the integral isospin, or meson, states using the same six constituent quark states. In this case the constituents are grouped together in fermion-antifermion pairs to prevent the net charge of the whole state becoming fractional.

3.1 Perturbation Theory and the S-Matrix.

To obtain predictions for the behaviour arising from constituent-constituent interactions, it is first necessary to consider the region where the potential acts. In this region detailed knowledge of the potential will be required and its form within the model of the previous section may be used. Before this is done, however, the scattering problem may once again be considered in the wave picture as shown previously in figure 2.1 and general expressions for non-relativistic behaviour may once again be derived before extensions to relativistic scattering energies are considered.

The solutions to the Schrödinger equation in the region where the potential operates are now expected to agree with those of the region outside of which the potential operates. A smooth continuation of the solutions from the inner region to the outer region across the boundary where the two regions meet is therefore required. This boundary occurs at a radius given approximately by the effective range of the potential. A steady state situation, however, is no longer the most appropriate if one wants to consider the region where the potential acts. A better method is to consider the time-dependent picture in which only the incoming wave of particles is present some long time before the interaction takes place.

The time-dependent Schrödinger equation in the region where the potential acts is given by

$$\imath\hbar\frac{\partial\Psi(r,t)}{\partial t} = \frac{p^2}{2m}\Psi(r,t) + V(r)\Psi(r,t).$$

The incoming wave will then enter this region for some short time duration τ, before leaving as a scattered and unscattered wave as before. Once again processes such as absorption are not considered here and the process of diffraction will be discussed later. The potential is expected to induce transitions from the initial state to some final state. Of interest is the probability of such a transition occuring.

To agree with the solutions to the outer region of the scattering problem the spatial part of the wavefunction describing the incoming wave, a long time before the interaction takes place, must be taken to be a plane wave. Since the time dependent picture is now being considered some time dependence now needs to be attached to this. In time-dependent quantum theory the time dependence is described by a group of matrix operators which are referred to as propagators. These describe how a general initial-state will change with time (t). In general, a propagator is given by following expression

$$U(t) = \exp\left(-\imath\frac{E}{\hbar}t\right)$$

where E represents the energy of the initial state. A system which is in an energy eigenstate $\Psi(r, t = 0)$ at time $t = 0$ will then be in the state

$$\Psi(r,t) = \exp\left(-\imath\frac{E}{\hbar}t\right)\Psi(r,t=0)$$

at some later time t. The incoming plane wave is therefore given by

$$\Psi(r,t) = \Psi(r)\exp\left(-\imath\frac{E}{\hbar}t\right)$$

where the initial state $\Psi(r)$ corresponds to the plane wave solutions of the free-particle Schrödinger equation discussed in the previous chapter. This is the wavefunction describing the incoming wave before it enters the region of the potential. The wavefunction afterwards has the same form since the sum of the two outgoing waves is also a plane wave (The outgoing plane wave solution to the free-particle Schrödinger equation was written in spherical polars and then separated to obtain the form of the scattered wave in the previous chapter). The probability that the system is in some final plane wave state m after time t is found by first operating from the left with $< \Psi_m(r,t)|$ which gives

$$< \Psi_m(r,t)|\Psi(r,t) >= C_m(t)\exp\left(-\imath\frac{(E_m - E_n)}{\hbar}t\right),$$

where the $C_m(t)$ factor represents the normalisation of the time-dependent plane waves, and squaring, which leads to

$$| < \Psi_m(r,t)|\Psi(r,t) > |^2 = |C_m(t)|^2.$$

The probability then that an outgoing wave, of momentum $\vec{p}_m$, arises from the interaction of the incoming wave, of momentum $\vec{p}_n$, with the potential is then given entirely by the coefficient $C_m(t)$.

A general expression for the coefficient $C_m(t)$ may be derived using perturbation theory if the potential may be assumed to be a small perturbation from the steady state solutions of the previous chapter [25]. This is expected to be particularly true of high energy interactions in which the incoming wave only exists in the prescence of the potential for a short time before leaving as a scattered and an unscattered wave. Time-dependent perturbation theory describes the coefficient by a series which gives a better approximation for the coefficient if more terms are included. The general expression is given as follows

$$C_m(t) = \delta_{nm} + \frac{1}{\imath\hbar}\int \exp\left(+\imath\frac{(E_m - E_n)}{\hbar}t\right) V_{mn}dt' \; + \; \text{Higher Orders}$$

where the V_{mn} factor stands for the matrix element

$$V_{mn} =< \phi_m(r)|V(t)|\phi_n(r) > .$$

Only a single initial plane wave state of one particular momentum is considered in the derivation of this expression. This corresponds, once again, to assuming that all the particles in the beam have the same energy. The first term is simply the statement that the initial and final states are identical. This corresponds to the unscattered wave of the previous chapter. The second term then contains part of the scattering behaviour which is of interest here.

To evaluate the integral in the second term some detailed knowledge of the potential is required. At high energies, however, the incoming projectile would be expected to pass through the region affected by the potential on a time scale shorter than that on which the potential varies. The potential may therefore be assumed to be independent of time and the matrix element V_{mn} may be brought outside the integral to give

$$C_m(t) = \frac{V_{mn}}{\imath\hbar}\int_0^\tau \exp\left(+\imath\frac{(E_m - E_n)}{\hbar}t\right) dt'.$$

The integral can now be performed giving

$$C_m(t) = \frac{V_{mn}}{\hbar}\frac{(\exp(\imath\omega_{mn}\tau) - 1)}{\omega_{mn}}.$$

Since the time dependence of the potential is not known exactly the energy at which this approximation becomes reasonable is not easy to determine. The probability of a transition (P_t), given by the square of this coefficient, is therefore

$$P_t = \frac{|V_{mi}|^2}{\hbar^2}\frac{(\exp(\imath\omega_{mi}\tau) - 1)^2}{\omega_{mi}^2}.$$

If the length of the perturbation were now to be increased the probability of a transition tends to infinity. This is because if the perturbation exists for an infinite length of time eventually a transition will occur. It is more usual, therefore, to consider the probability of a transition per unit time (Γ). This is given by

$$\Gamma = \frac{P_t}{\tau} = \frac{|V_{mn}|^2}{\hbar^2}\frac{(\exp(\imath\omega_{mn}\tau) - 1)^2}{\omega_{mn}^2\tau}.$$

and is referred to as the transition rate. In the limit that τ tends to infinity a delta function may be extracted to give

$$\Gamma = \frac{|V_{mn}|^2}{\hbar^2}\delta(E_m - E_n).$$

This is referred to as Fermi's Golden Rule [26].

An alternative way of obtaining Fermi's Golden Rule is to use the following expression for the coefficient $C_m(t)$

$$C_m(t) = < \Psi_m(r)|S|\Psi(r) >$$

where an element of the matrix operator S is given by

$$S_{mn} = \delta_{mn} + i(2\pi)^4\delta^4\left(\sum_n p_n - \sum_m p_m\right) A_{mn}.$$

This expression relates an element of the operator S to the more familiar amplitude element (A_{mn}) which is written down from a Feynman diagram [27]. When evaluated this then gives Fermi's Golden Rule directly. The operator S, referred to as the S-matrix [28], was introduced by German physicist W. Heisenberg to describe scattering experiments, although the method was not new. The S-matrix method will be used here since it is simple to extend this to relativistic scattering energies.

This expression may now be converted into an expression for the angular differential cross section in a similar way to that discussed in section 2.2. The main difference before this can be divided by the incoming flux of the beam, however, is that the sum of all probabilities for scattering to all final states which lie inside a cone of opening angle $d\Omega$ must be found. This is done by performing a phase space integral to incorporate the density of final states available inside the cone. The angular differential cross section is then given by a Fourier transform in momentum transfer. An alternative expression for the scattering amplitude may then be extracted.

3.2 The Cutkosky Unitarity Condition.

The S-matrix may be shown to be a unitary matrix, that is that it fulfils the condition $SS^\dagger = I$, where I represents the identity matrix and the dagger refers to the adjoint, the transpose and complex conjugate, of S. The unitarity of the S-matrix reflects the need for probability to be conserved, the sum of the probabilities for all individual transitions occuring summing to unity. This is because unitary operators preserve the value of scalar products which in quantum theory are used to calculate probabilities.

The formula for the S-matrix may be written as follows

$$S = I + iT$$

where an element of the T-matrix is,

$$T_{mn} = (2\pi)^4 \delta^4 \left(\sum_n p_n - \sum_m p_m \right) A_{mn}.$$

Substituting this into the condition of unitarity gives

$$(I + iT)(I - iT^\dagger) = I$$

which implies that

$$I + iT - iT^\dagger + TT^\dagger = I$$

The identity matrix appears on both sides and may be cancelled leaving

$$T - T^\dagger = iTT^\dagger$$

The matrix element equation now looks like

$$< m|T|n > - < m|T|n >^* = i < m|TT^\dagger|n >$$

where the * denotes complex conjugation. Since the S-matrix may also be shown to be symmetrical the left hand side can be written as just

$$2\, i\, \mathrm{Im} < m|T|n > .$$

Inserting the completeness relationship on the right hand side and summing over all allowed intermediate states (i) gives

$$2\ \mathrm{Im} < m|T|n > = \sum_i < i|T|m >^\dagger < i|T|n > .$$

Finally, returning to the original definition of the T-matrix element

$$2\ \mathrm{Im} T_{mn} = (2\pi)^4 \delta^4 \left(\sum_n p_n - \sum_m p_m \right) \sum_i A_{ni} A^*_{im}$$

Unitarity thus leads to an expression which relates the imaginary part of the scattering amplitude to a sum over all allowed intermediate states (all possible processes which may occur in the interaction region). This is the Cutkosky unitarity condition [29]. A special case of the Cutkosky formula is the optical theorem. This occurs when the initial and final states are identical (the elastic scattering condition). The agreement with Regge theory therefore is still good. To proceed further it is necessary to know what the intermediate states of a scattering process are.

3.3 Extension to Relativistic Scattering (Quantum Field Theory).

During the 1970s quantum field theory, following its successful description of electromagnetic interactions, was applied to the strong interaction, leading to the development of quantum chromodynamics, or QCD. Within this new framework relativistic quantum equations were re-interpreted as field equations to avoid the introduction of negative energy states and a non-positive definite probability density in the continuity equation. The description of a single particle in terms of its position at a specific time was then replaced by a field which adopted a particular value depending on the particle's four-vector. Relativistic particle interactions could then be described if these scalar fields were subjected to the constraint that they possessed the symmetry of a particular interaction. This constraint is applyed by Noether's theorem [30], which restricts particle interactions to be locally symmetric, charge, for example, being conserved within a single particle interaction and not just in the universe as a whole. The strong interaction was then taken to possess SU(3) symmetry and when this restriction was placed upon the particle scalar fields it became necessary, mathematically, to introduce an associated gauge field, a field which was invariant under a gauge transformation. In analogy to the electromagnetic case where the associated gauge field became a solution to a special case of Maxwell's equations (called the Proca equations) and could be identified with the photon, the gauge field of the strong interaction could also be identified with a massless object of unit spin. This object is referred to as the gluon and is expected to be the propagator of the strong interaction.

The idea may also be applied to the force propagators themselves. This is done using gauge field theory, in which the symmetry of the force is applied to gauge fields. In the case of the strong interaction, this leads to the consideration of triple gluon vertices, interactions in which three gluons may interact together. These are particularly important when considering the behaviour of the pomeron in QCD. Triple photon vertices do not arise from the symmetry of the electromagenetic force. Free individual quarks and free gluons, however, have never been observed. One possible explanation of this is that quarks and gluons possess an additional quantum number, similar to electric charge, and that non net-zero values of this

quantum number are forbidden in the free state. This quantum number is referred to as colour and to account for the observed list of strongly interacting particles it must possess three degrees of freedom. That is to say, there must be three types of strong charge. These are usually labelled red, blue and green. Quark-antiquark or three quark configurations are then required to have net-zero colour values, since these may appear as free-states. A theory of colour confinement would explain each of these missing observations, at present, however, no satisfactory theory of colour confinement exists. The SU(3) symmetry of the strong force arises here from the SU(3) symmetry of the colour wavefunction.

3.4 A Pomeron Exchange Process in QCD.

In QCD it is possible to write down the amplitude for a process directly from the Feynman diagram describing that particular interaction. This is done using Feynman rules. A derivation of the Feynman rules in QCD is not given here. They are stated, however, in Appendix A. Since none of the fundamental particles in QCD possess the quantum numbers of the vacuum, pomeron exchange has to be simulated using combinations of quarks and gluons whose net effect is to exchange the quantum numbers of the vacuum. An extension of QCD to include bound-gluon, or glueball, states, which may also possess the quantum numbers of the vacuum, is not considered here.

To identify the pomeron in QCD the total amplitude calculated from all possible diagrams that exchange these quantum numbers must be considered in the correct kinematic region. This is the high energy, or Regge, limit, in which the centre-of-mass energy squared s is much larger than the momentum transfer squared t. To agree with Regge theory the amplitude in this limit must behave as follows

$$\lim_{s \gg t} A \sim s^{\alpha(t)}.$$

If this is the case the property which is exchanged is said to Reggeize. The diagrams which dominate in this limit contain a $\ln(s/t)$ factor in their calculated amplitudes. Only the diagrams which are important in this limit are considered here. An explanation as to why other exchange diagrams may be neglected may be found in [31]. The expression obtained is a perturbation series in the strong coupling constant α_s.

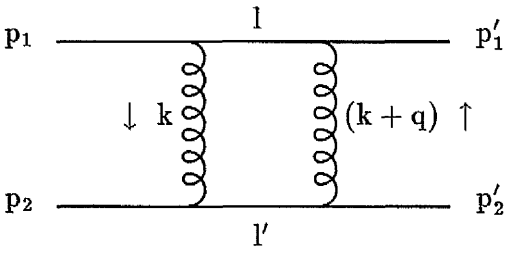

Figure 3.1: The simplest process in which the quantum numbers of the vacuum may be exchanged in QCD corresponds to two gluons exchanged between two incoming quarks. The first gluon alters the colours of the incoming quarks. A second gluon is therefore required to revert the quark colours back to their initial states. No net colour is then exchanged.

The calculation of the first non-zero term in the perturbation expansion (the term proportional to α_s^2) is described here. The extensions to the method required to calculate the higher-order terms in the series are then discussed. Since only those diagrams which contain a ln(s) factor are considered this method for calculating the scattering amplitude is often referred to as the leading log expansion.

The basic, underlying interaction is taken to be quark-quark elastic scattering (This must then later be fitted into a hadron-hadron interaction). To avoid contributions from diagrams in which quarks are exchanged, the incoming quarks are taken to have different colours. The two quarks may also be assumed to approach in opposite directions along the z-axis. If the masses of the two quarks are assumed to be both equal to zero then the centre of mass energy squared (s) is shared equally between them and the components of their four vectors, p_1 and p_2, are

$$p_1 = (\sqrt{s}/2, \sqrt{s}/2, 0, 0)$$
$$p_2 = (\sqrt{s}/2, -\sqrt{s}/2, 0, 0)$$

If an object with the quantum numbers of the vacuum, a colour singlet object, is exchanged between the quarks then they will have the same colours in the out-state as they did before the exchange took place. The simplest process then in which this can be achieved is shown in figure 3.1. The first gluon alters the colours of the two quarks in the intermediate state and a second gluon is then required to alter them back again, so that no net colour is exchanged.

The full amplitude for this process may be calculated from this diagram. A method which is more easily extended to include all the possible diagrams, however, is to begin by calculating the imaginary part of the scattering amplitude using the Cutkosky formula,

$$\mathrm{ImA} = \frac{1}{2}\int \mathrm{d(phasespace)A_0(k)A_0^{\dagger}(k-q)}$$

of section 3.3. The amplitude for just the left-hand side of this diagram is then calculated, inserted together with its hermitian conjugate into the formula and integrated over the phase space of the intermediate quark lines which are cut when the diagram is divided into two halves. The left hand side of this diagram is that of quark-quark elastic scattering via the exchange of a single gluon. The amplitude for this process is given by

$$A_0 = 8\pi\alpha_s\frac{s}{t}\delta_{\lambda_1\lambda_1'}\delta_{\lambda_2\lambda_2'}G_0^{(8)}.$$

and is calculated using the Feynman rules given in Appendix A. Here the colour factor $G_0^{(8)}$ is obtained from the colour generators for the upper and lower quark lines according to

$$G_0^{(8)} = \tau_{ij}^a\tau_{kl}^a.$$

The expression has be simplified using $\alpha_s = g^2/4\pi$. The λ-factors represent the quark helicities, the components of the spin of the quarks along their momentum directions. The elements of the delta matrices are equal to unity when the quark helicities are equal and equal to zero otherwise.

To simplify the expression the condition that s is much larger than t has also already been imposed. In the diagram of figure 3.1, the net momentum-transfer squared is given by $|t| = |q^2|$ and, in the Regge limit, all of the components of the four vector q may be approximated as being equal to zero. This arises since the outgoing quarks of the single gluon exchange process, the intermediate quarks of the complete diagram, are taken to be on-shell in the calculation, their four-vectors squared equalling zero. This simplifies the expression and makes it possible to replace factors such as $\bar{u}(\lambda_1', p_1)\gamma^\mu u(\lambda_1, p_1)$ by the following

$$\bar{u}(\lambda_1', p_1)\gamma^\mu u(\lambda_1, p_1) = 2p_1^\mu$$

since multiplying out the left-hand side gives a four-vector. The factor 2 arises from the choice of normalisation of the spinors u. This approximation is referred to as

the eikonal approximation and applies whenever the exchanged particle is of a low momentum. It can be applied to a gluon exchanged between particles of any spin. Importantly, the approximation can still be used if the quark lines are replaced by gluons.

The hermitian conjugate of A_0 is obtained by taking its complex conjugate and reversing the signs of all the momenta. It is given by

$$A_0^\dagger = 8\pi\alpha_s \frac{s}{t}\delta_{\lambda_1\lambda_1'}\delta_{\lambda_2\lambda_2'}G_0^{(8)}.$$

This gives directly the right hand side of the complete two-gluon exchange diagram. On the right-hand side the momentum transfer squared is given by $t = (k-q)^2$. The imaginary part of the amplitude for the two gluon exchange process is therefore given by

$$\mathrm{Im}A = 32\pi^2\alpha_s^2 \int \mathrm{d(phasespace)} \frac{s}{k^2}\frac{s}{(k-q)^2}\delta_{\lambda_1\lambda_1'}\delta_{\lambda_2\lambda_2'}G_a$$

The integral must be performed over the phase space of the two cut quark lines which have momenta l and l'. This integral is given by

$$\int \mathrm{d(phasespace)} = \int \frac{d^4l}{(2\pi)^3}\frac{d^4l'}{(2\pi)^3}\delta(l^2)\delta(l'^2)(2\pi)^4\delta^4(p_1+p_2-l-l')$$

and may be simplified by combining together the factors of 2π and absorbing the delta function $\delta^4(p_1+p_2-l-l')$ into the integral over d^4l', giving

$$\int \mathrm{d(phasespace)} = \frac{1}{(2\pi)^2}\int d^4k\delta[(p_1-k)^2]\delta[(p_2+k)^2].$$

Absorbing the delta function fixes

$$\begin{aligned} l' &= p_1+p_2-l = p_2+k \\ l &= p_1-k. \end{aligned}$$

Here the integration has also been converted from an integral over the four-vector l to an integral over the four vector k. This is because it is more convenient to integrate over the momentum of the exchanged gluon. No extra factor is picked up when making this conversion. This is because, since p_1 is fixed, the differential of each component of l is given by $dl^\mu = -dk^\mu$ and, since there a four such components, the minus signs cancel giving $d^4l = d^4k$.

The momentum of the exchanged gluon may now written in terms of the incoming quark momenta as follows

$$k^\mu = \rho p_1^\mu + \lambda p_2^\mu + k_\perp^\mu$$

where ρ and λ are parameters and $k_\perp^\mu$ describes the momentum transverse to p_1 and p_2. The four-vector $k_\perp^\mu$ therefore only has two non-zero components

$$k_\perp = (0, 0, \mathbf{k})$$

described by the two-dimensional vector $\mathbf{k}$, which has an x and a y-component only. In terms of the earlier definitions of the quark momenta the four vector of the exchanged gluon becomes

$$k = \left((\rho + \lambda)\frac{\sqrt{s}}{2}, (\rho - \lambda)\frac{\sqrt{s}}{2}, \mathbf{k} \right).$$

This is referred to as a Sudakov parameterisation. In terms of the Sudakov variables the quantities which appear inside the delta functions may be written as

$$\begin{aligned} (p_1 - k)^2 &= -s\lambda(1-\rho) - \mathbf{k}^2 \\ (p_2 + k)^2 &= s(1+\lambda)\rho - \mathbf{k}^2. \end{aligned}$$

and it is possible to convert the integrals over two of the four components of the exchanged gluon momentum to integrals over the Sudakov parameters as follows

$$\int d(\text{phasespace}) = \frac{s}{8\pi^2} \int d\rho d\lambda d^2\mathbf{k} \delta(-s(1-\rho)\lambda - \mathbf{k}^2)\delta(s(1+\lambda)\rho - \mathbf{k}^2).$$

In the Regge limit both ρ and λ are much smaller than one. It is then becomes possible to approximate

$$k^2 = \mathbf{k}^2$$

and similarly

$$(k - q)^2 = -(\mathbf{k} - \mathbf{q})^2.$$

Absorbing the delta functions to perform two of the integrals gives the following result for the imaginary part of the amplitude,

$$\text{Im}A = 8\pi\alpha_s^2 \frac{s}{t} \delta_{\lambda_1\lambda_1'} \delta_{\lambda_2\lambda_2'} G_a \frac{\alpha_s}{2\pi} \int \frac{-\mathbf{q}^2}{\mathbf{k}^2(\mathbf{k}-\mathbf{q})^2} d^2\mathbf{k}. \tag{3.1}$$

The amplitude also, however, has a real part. This may be easily obtained from the imaginary part since it is known that the sum of the real and imaginary parts of the amplitude is given by some expression F multiplied by ln(s/t). As explained on page 68 the exact details as to which diagrams contain the important log factor in their total amplitude is not considered here. Since t is negative the total amplitude may be expanded as follows

$$\mathrm{F}\ln\left(\frac{\mathrm{s}}{\mathrm{t}}\right) = \mathrm{F}\ln\left(\frac{\mathrm{s}}{-1\times|\mathrm{t}|}\right) = \mathrm{F}\ln\left(\frac{\mathrm{s}}{|\mathrm{t}|}\right) - \mathrm{F}\ln(-1).$$

Since minus one can be written as a complex exponential this may be simplified to

$$\mathrm{F}\ln\left(\frac{\mathrm{s}}{\mathrm{t}}\right) = \mathrm{F}\ln\left(\frac{\mathrm{s}}{|\mathrm{t}|}\right) - \mathrm{F}\ln(\exp(i\pi))$$

so therefore

$$\mathrm{F}\ln\left(\frac{\mathrm{s}}{\mathrm{t}}\right) = \mathrm{F}\ln\left(\frac{\mathrm{s}}{|\mathrm{t}|}\right) - i\mathrm{F}\pi.$$

The imaginary part of the amplitude has been calculated and the factor F can be extracted and used to write down an expression for the real part directly. The real part of this amplitude is then given by

$$\mathrm{ReA} = 8\pi\alpha_s^2\frac{\mathrm{s}}{\mathrm{t}}\ln\left(\frac{\mathrm{s}}{|\mathrm{t}|}\right)\delta_{\lambda_1\lambda_1'}\delta_{\lambda_2\lambda_2'}\mathrm{G_a}\frac{\alpha_s}{2\pi^2}\int\frac{-\mathbf{q}^2}{\mathbf{k}^2(\mathbf{k}-\mathbf{q})^2}\mathrm{d}^2\mathbf{k}$$

The sum of the real and imaginary parts gives the one-loop scattering amplitude for colour-singlet exchange in QCD, once the appropiate colour factor $\mathrm{G_a}$ is inserted. The expression is of order α_s^2. There are no lower order amplitudes since a minimum of two gluons is needed to exchange the quantum numbers of the vacuum in QCD. There are no extra corrections to the one-loop diagram.

To obtain the entire first term of the perturbative expansion all other diagrams which contribute expressions of order α_s^2 in the Regge limit must be calculated. These are then summed with the expression already obtained to give the first term. The only additional graph to consider is shown in figure 3.2. The real part of this amplitude can be obtained directly from the real part of the previously calculated process using crossing symmetry. Since crossing symmetry has the effect of reversing p_2 and p_2' it has the effect of twisting the lower quark line of figure 3.1 around so that the diagram matches that of figure 3.2. The real part of the crossed gluon graph is therefore calculated by replacing s by -u. The crossed gluon graph turns out to not have an imaginary part.

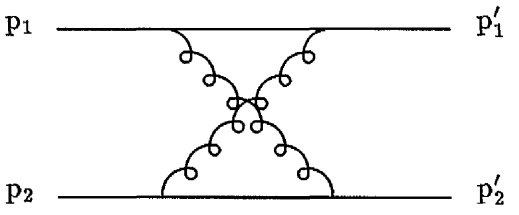

Figure 3.2: At leading order a second colour-singlet exchange diagram is also of significance in the Regge limit. The calculated amplitude for this process is summed with the one-loop amplitude to give the leading-order term of the perturbation series.

The total amplitude at leading order is now given by the sum of these two contributing amplitudes. Since, for colour singlet exchange, the real parts of the two amplitudes are equal and opposite, due to the fact that both amplitudes have the same colour factors, the real part of the total when the two results are added together disappears, leaving a purely imaginary result. The first term of the expansion was therefore already obtained in Equation 3.1. It is purely imaginary and is given by

$$A_1 = 8i\pi\alpha_s^2 \frac{s}{t}\delta_{\lambda_1\lambda_1'}\delta_{\lambda_2\lambda_2'}G_a\frac{\alpha_s}{2\pi}\int \frac{-\mathbf{q}^2}{\mathbf{k}^2(\mathbf{k}-\mathbf{q})^2}d^2\mathbf{k}.$$

3.5 The BFKL Equation.

The process may essentially be continued to higher and higher orders, only keeping the diagrams which would be of importance at high s (those with the important log factor). The full calculation is complicated due to the larger number of diagrams that must be considered at each higher order. A number of simplifications, however, may be borrowed from the calculation which demonstrated that the gluon Reggeizes in QCD. This was performed by, among others, Tyburski [32], Frankfurt and Shermann [33], Lipatov [34] and Cheng and Lo [35] during 1976 and 1977. This work showed that the amplitude for colour-octet exchange has the Regge theory dependence in the Regge limit. An expression for behaviour of the gluon trajectory was extracted. In the calculation of the amplitude for colour octet exchange it was found that the diagrams which contribute to each higher term in the series,

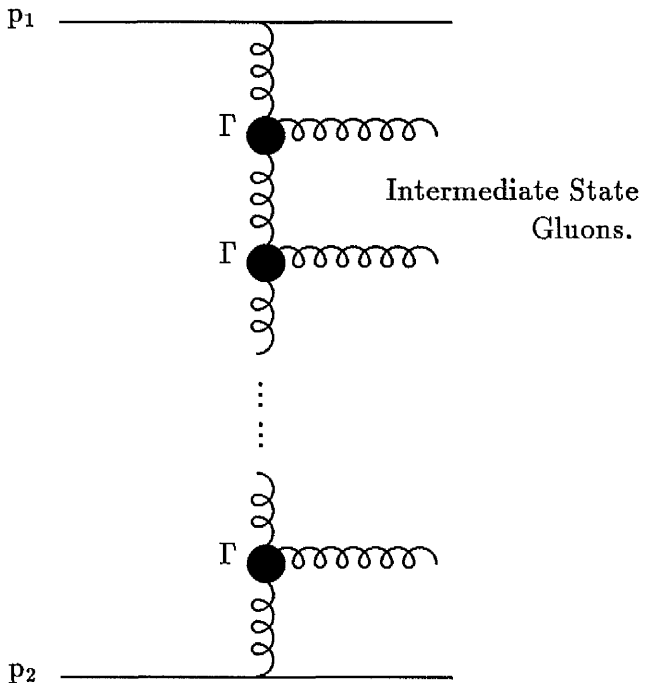

Figure 3.3: Left-hand diagrams at higher orders are combined together to give a single, effective, left-hand diagram to demonstrate the Reggeization of the gluon in QCD. The same process may be applied to Pomeron exchange. The amplitude for the combined left-hand diagrams is then written down directly using Feynman rules for effective vertices (Γ) and effective, or Reggeized, gluons, for the vertical sections of the ladder. An extra rung in the effective diagram appears at each higher order.

except those obtained by 'twisting' another diagram, could all be combined into an effective diagram as shown in figure 3.3. The contributions from the 'twisted' diagrams were calculated afterwards using crossing symmetry. When this effective diagram is paired up with its right-hand diagram it forms a ladder diagram. An extra rung in the ladder appears at each order. The amplitude for all of the contributing processes could then be written down directly from one effective left-hand diagram. The Feynman rules for the factors which arise from the vertices are no longer the normal triple gluon vertices, however, but effective particle vertices Γ which incorporate the effect of combining many left-hand diagrams together. In addition the gluon propagator terms for the vertical sections of the ladder are no longer normal gluon propagators but effective gluon propagators which contain the

effect of all the corrections to the loop diagrams. These are often referred to as Reggeized gluons. To calculate a particular term in the series the expression for the effective left-hand amplitude calculated from the diagram with the correct number of rungs for that particular order, may then be inserted, together with its hermitian conjugate, into the Cutkosky formula as before. The phase space integral will now be performed over several cut lines. It may once again be simplified using a Sudakov parameterisation. Each of the vertical sections of the ladder, however, must now be individually parameterised. It is also necessary to ensure that all of the possible polarisation states of the intermediate gluons are summed over.

The leading log behaviour arises from a region of phase space where the ρ-parameters are ordered such that $\rho_1 \gg \rho_2 \gg \rho_3$ and so on. This strong ordering has the effect of making the four-vectors of the vertical sections of the ladder more transverse as lower and lower sections of the ladder are considered. The ladder diagram, therefore, is sometimes drawn so that it is wider at the top than at the bottom. The result includes additional integrals over the ρ factors, one of which arises from each of the vertical sections which are parameterised. Since the integration limits also contain ρ factors, these integrals are nested inside one another. These integrals may be performed, however at higher orders the number of integrals nested inside each other becomes larger. Since there are an infinite number of terms in the series, the number of nested integrals in fact tends to infinity. It was therefore found to be more convenient to take an integral transform of the expressions for the amplitude converting it into a new integral transformed space. The particular integral transform which was chosen was a Mellin transform since this has the effect of decoupling the nested integrals in each of the terms of the series. The Mellin transform $\mathrm{F}(\omega)$ of a functions f(s) is given by

$$\mathrm{F}(\omega) = \int_1^\infty \mathrm{f(s)} \left(\frac{\mathrm{s}}{\mathbf{k}^2}\right)^{-\omega-1} \mathrm{d}\left(\frac{\mathrm{s}}{\mathbf{k}^2}\right)$$

and maps f(s) into the complex ω-plane. The function f(s) is the expression for a term in the series which contains the nested integrals and the Mellin transform converts this into a simple product. With the nested integrals decoupled the problem of finding the sum of all the terms in the series, which is now written as a series of Mellin transforms, may now be considered. The expression for the sum would then need to be converted back into the original space using an inverse Mellin transform.

The inverse Mellin transform of the function $F(\omega)$ is defined as follows

$$f(s) = \frac{1}{2\pi i}\int_C F(\omega)\left(\frac{s}{k^2}\right)^{\omega} d\omega.$$

Here the contour C is taken to the right of all singularities in $F(\omega)$. At this stage the 'twisted' diagrams may be added to this. The contribution from all of the twisted diagrams together may be calculated by crossing symmetry.

The expression for the sum of the Mellin transform series, however, is not so simple to obtain. It is not possible to easily identify it with a geometric progression, or as the Taylor expansion of some well-known mathematical function. Therefore, to obtain the sum, an integral equation, an equation which contains the same information as the series, is derived [36]. Integral equations have the form

$$\lambda\int K(x,y)f(y)dy + g(x) = f(x),$$

and may be solved, to find the function f(x), by iteration. As a first approximation the function f(x) is taken to be equal to the function g(x). To obtain a better approximation this may be inserted into the left-hand side of the integral equation giving

$$f(x) = g(x) + \lambda\int K(x,y)g(y)dy.$$

This better approximation may then be re-inserted into the left-hand side of the intergral equation to give a third order approximation,

$$f(x) = g(x) + \lambda\int K(x,y)\left[g(y) + \lambda\int K(y,y')g(y')dy'\right]dy,$$

and so on. The solution f to the integral equation is then an infinite series. An integral equation may be written which generates the terms in the Mellin transform series. This equation will contain the same information as the series and essentially describes the complicated pattern that emerges with each successive term. It is given as follows,

$$\omega\, f(\omega,\mathbf{k}_1,\mathbf{k}_2,\mathbf{q}) = \delta^2(\mathbf{k}_1-\mathbf{k}_2) + \frac{\bar{\alpha}_s}{2\pi}\int d^2\mathbf{k}'\left[\frac{-\mathbf{q}^2}{(\mathbf{k}'-\mathbf{q})^2\mathbf{k}_1^2}f(\omega,\mathbf{k}',\mathbf{k}_2,\mathbf{q})\right.$$

$$+\frac{1}{(\mathbf{k}'-\mathbf{k}_1)^2}\left(f(\omega,\mathbf{k}',\mathbf{k}_2,\mathbf{q}) - \frac{\mathbf{k}_1^2 f(\omega,\mathbf{k}_1,\mathbf{k}_2,\mathbf{q})}{\mathbf{k}'^2+(\mathbf{k}_1-\mathbf{k}')^2}\right)$$

$$\left.+\frac{1}{(\mathbf{k}'-\mathbf{k}_1)^2}\left(\frac{(\mathbf{k}_1-\mathbf{q})^2\mathbf{k}'^2 f(\omega,\mathbf{k}',\mathbf{k}_2,\mathbf{q})}{(\mathbf{k}'-\mathbf{q})^2\mathbf{k}_1^2} - \frac{(\mathbf{k}_1-\mathbf{q})^2 f(\omega,\mathbf{k}_1,\mathbf{k}_2,\mathbf{q})}{(\mathbf{k}'-\mathbf{q})^2+(\mathbf{k}_1-\mathbf{k}')^2}\right)\right].$$

This equation is referred to as the BFKL equation after Boritsky, Fadin, Kuraev and Lipatov, although several different approaches in fact led to this result [37]. The parameter $\bar{\alpha_s}$ is given by $\bar{\alpha_s} = N\alpha_s/\pi$. The BFKL equation is the integral equation in Mellin transform space which describes a large amount of the behaviour of the pomeron in QCD. The BFKL equation can now be solved to obtain an expression for the function $f(\omega, \mathbf{k}_1, \mathbf{k}_2, \mathbf{q})$ and this may then be inverted using the inverse Mellin transform.

3.6 Solving the BFKL Equation.

The general procedure for solving the BFKL equation is to first manipulate it so that it is written in the form of a Green's function equation. For zero momentum transfer writing the BFKL equation in the form of a Green's function equation is simply a matter of setting $q^2 = 0$ and rearranging. The BFKL equation then takes the form

$$\omega\, f(\omega, \mathbf{k}_1, \mathbf{k}_2, 0) = \delta^2(\mathbf{k}_1 - \mathbf{k}_2) + \kappa \cdot f(\omega, \mathbf{k}_1, \mathbf{k}_2, 0).$$

The operator κ of a Green's function equation is called the kernel and is an integral operator which acts on the function $f(\omega, \mathbf{k}_1, \mathbf{k}_2, 0)$. The solution for zero momentum transfer corresponds to the intercept of the pomeron trajectory and was actually the first obtained, by Balitsky and Lipatov in 1978 [38]. The solution for non-zero momentum transfer, which gives information on the behaviour of the gradient of the pomeron trajectory, is much more complicated, and was in fact published eight years later by Lipatov in 1986 [39]. Before the BFKL equation could be rearranged here into the form of a Green's function equation it was first necessary to take a two-dimensional Fourier transform of the whole BFKL equation. A two dimensional Fourier transform was needed because, in terms of the Sudakov parameterisation, transverse four-vectors are written in terms of a two-dimensional transverse wavevector. The Fourier transform then re-expresses the BFKL equation in terms of impact parameters. An impact parameter is the distance from the centre of the target particle to the centre of the incoming particle's line of flight. Thus the problem is converted into impact parameter space and needs to be inverted back to Mellin space before an inverse Mellin transform can be taken (The problem is now two spaces away from where it was started).

In both kinematic regions the expression for $f(\omega, \mathbf{k}_1, \mathbf{k}_2, \mathbf{q})$ which is the solution of the Green's function equation is given in terms of the eigenfunctions $\phi_i(\mathrm{k})$ and eigenvalues λ_i of the integral operator κ. The expression which needs to be considered is therefore

$$\kappa \cdot \phi_i(\mathbf{k}) = \lambda_i \phi_i(\mathbf{k}).$$

The eigenvalues turn out to be identical in the non-zero momentum transfer calculation as they do in the zero momentum transfer calculation. Once the solutions to this equation have been found the function $f(\omega, \mathbf{k}_1, \mathbf{k}_2, \mathbf{q})$ may be formed. For zero momentum transfer

$$f(\omega, \mathbf{k}_1, \mathbf{k}_2, 0) = \sum_i \frac{\phi_i(\mathbf{k}_1)\phi_i(\mathbf{k}_2)}{\omega - \lambda_i}.$$

This is the solution to the BFKL equation (for zero momentum transfer) and is equal to the sum of the series in Mellin transformed space (The series is often referred to as the BFKL series).

In the process of solving the eigenvalue equation to find the eigenfunctions $\phi_i(\mathrm{k})$ and the eigenvalues λ_i, the eigenfunctions are each written as a series

$$\phi_i(\mathbf{k}) = \sum_{n=0}^{\infty} \phi_i^n(\mathrm{k}) \frac{e^{in\theta}}{\sqrt{2\pi}}.$$

Since the eigenfunctions of the kernel are required to fulfill a completeness relationship it is necessary to restrict the coefficients $\phi_i^n(\mathrm{k})$ to the following behaviour

$$\phi_i^n(\mathrm{k}) \sim (\mathrm{k}^2)^{-1/2+i\nu}.$$

The imaginary part of the argument, described by the parameter ν, may lie anywhere along the line $\mathrm{Re}(\arg) = -1/2$. The parameter ν is therefore a continuous parameter which may take values ranging from $-\infty$ to $+\infty$. In both kinematic regions the final expression for the function $f(\omega, \mathbf{k}_1, \mathbf{k}_2, \mathbf{q})$ therefore turns out to include an integral over ν. Since this is a continuous variable a cut is obtained in the complex ω-plane. This is the first indication that the QCD hypothesis of quark constituents interacting via gluon exchange does not agree with the more general Regge theory description of scattering processes. The differences between the QCD and Regge theory pomerons will be discussed in more detail at the end of this chapter. To complete the discussion of the QCD approach however, the method of deriving cross section predictions in QCD is now considered.

3.7 Calculating Cross Sections in QCD.

To obtain hadron-hadron cross sections the function $f(\omega, \mathbf{k}_1, \mathbf{k}_2, \mathbf{q})$, which refers to pomeron exchange between quarks, must first be adapted so that it describes pomeron exchange between hadrons. The four external particles (the top and bottom of each leg of the Reggeized gluon ladder) therefore no longer couple to a single constituent quark inside a hadron but may be joined in various different ways to several quark constituents. This coupling is incorporated by calculating an impact factor for each pomeron-hadron vertex (fig. 3.4). The inverted expression will then related to the scattering amplitude. In the high energy limit the inverse transform may be simplified by noting that the n = 0 coefficients of the power series expansions of the eigenfunctions dominate and that the eigenvalues may be described by the first two terms of a power series expansion in ν. This is referred to as the n = 0 azimuthally symmetric approximation. As in Regge theory, the singularity with the largest real part then dominates.

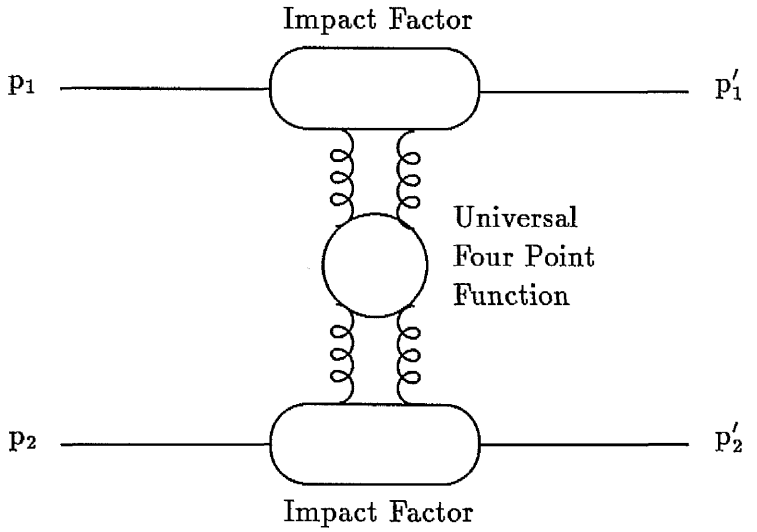

Figure 3.4: To calculate expressions for hadron-hadron interactions, impact factors, represented here by ovals at the upper and lower vertices, must be calculated to describe the coupling of the universal four point function to the quark constituents of each participating hadron. The universal four point function describes pomeron exchange between quarks.

3.8 Comparison of the Regge Theory and QCD Pomerons.

As explained previously the pomeron derived using perturbative QCD is described by a cut in the complex ω-plane instead of a pole. This leads to a number of important distinctions between the QCD pomeron and the Regge theory pomeron.

The amplitude for pomeron exchange in QCD does Reggeize. The function which corresponds to the trajectory may therefore be extracted and has the dependence

$$\alpha(t) = 1 + 4\bar{\alpha}_s \ln 2.$$

The trajectory, however, now has no dependence on t. The singularities for zero momentum transfer were the same as those for non-zero momentum transfer and therefore do not move in the complex-plane as t varies. On a Chew-Frautschi plot the trajectory therefore appears as a constant straight line at some non-physical value of angular momentum. Since QCD did not incorporate the existence of bound particle states with the quantum numbers of the vacuum, this result could have been written down directly since this is the only trajectory which agrees with the initial hypothesis. A trajectory with even the slightest gradient will eventually pass through a physical angular momentum value and a particle state would then exist. The strong coupling constant α_s, however, might be considered to vary, or to run, with t. This would then change the shape of the trajectory such that it does pass through physical particle states. These physical particle states would then be formed using combinations of quarks and gluons.

The intercept of the QCD pomeron trajectory, however, is larger than the value of 1.08 which was extracted from fits to experimentally measured cross sections using Regge theory during the 1960s, even if the coupling constant is allowed to run. If the coupling constant is allowed to run then the QCD intercept corresponds to the value of $\alpha(t)$ when α_s is set to its value at t=0. This means that, according to QCD, the total cross section is expected to rise faster than it actually does. In particular, the total cross section rises too quickly with increasing centre-of-mass energy squared s. It leads to the violation of a certain unitarity bound and therefore probabilities no longer sum to unity. Unitarity bounds were discussed in section 2.3.

Once the coupling constant is allowed to run with t the pomeron trajectory is no longer independent of the properties of the scattering particles. It in fact becomes dependent upon the size of the participating particles. Many measured cross sections, however, tend to the same pomeron trajectory regardless of the size of the participating particles. The pomeron should couple in the same way to quarks as to antiquarks, since it possesses the quantum numbers of the vacuum. The coupling of the pomeron to a hadron should therefore only be proportional to the number of quarks it contains and not related to the size of the larger net hadronic state. This is described by the quark counting rule [40]. For certain processes, however, this rule is violated and the coupling of the pomeron to a hadron suggests that some baryon states do not contain three quarks and some meson states do not contain two, even though this was one the the basic assumptions of the model.

Many attempts have been made to smooth out the differences between the two pomeron behaviours. One possible solution is that the full BFKL series, which was derived for high centre-of-mass energies, may not apply the low centre-of-mass energy region where the pomeron intercept of 1.08 was extracted. The behaviour of the pomeron could therefore vary with centre-of-mass energy tending to the full QCD behaviour as s increases. The behaviour might also, however, vary with t. The perturbative QCD approach, as will be seen in the next chapter, is only expected to be valid when |t| is greater than about 1 GeV^2. Regge theory is valid for all t but the extracted intercept may vary as t is increased. The QCD pomeron may then represent a high energy , high momentum transfer behaviour which reproduces the behaviour extracted using Regge theory at lower values of s and t. The QCD pomeron is then referred to as the hard BFKL pomeron and the lower t behaviour is referred to as soft-pomeron behaviour. A single pomeron description which gives the correct behaviours in both the low and high t limits was proposed by E. M. Levin and C. Tan in 1992 and is referred to as the heterotic pomeron [41].

It has become necessary to reconsider the validity of all the many assumptions in the QCD derivation of the pomeron. Some considerable progress has been made in obtaining 'sub-leading' corrections to the approximation that the leading log expansion is reasonable for deriving the pomeron's behaviour. The problem of unitarity violation has also been addressed using a colour dipole model. The best way, however, to decide if the behaviour of the pomeron varies with t is to experimentally investigate the high |t| region.

Chapter 4

Diffractive Vector Meson Production at high-$|t|$.

When scattering processes are treated in the quantum mechanical wave picture it automatically becomes possible to identify certain scattering processes with effects first observed in optics experiments. One such effect, which is referred to as diffraction, arises when an obstacle is placed in the path of an incoming light wave and the components of the light wave which are not absorbed by the obstacle then interfere with each other creating a pattern on a screen placed some distance behind the obstacle. This process may occur in a scattering experiment when part of the wavefront of the incoming wave is absorbed by the target and the resulting pattern observed in the detectors (the screen) arises from the interference of the components of the incoming wavefront which were not absorbed by the target. It may also occur in colliding beam experiments where it is always possible to work in the rest frame of the target particle. In the quantum mechanical wave treatment of the scattering process discussed in chapter 2 the total flux which left the interaction region equalled the total flux of the incoming wave. There was therefore no absorption of any part of the incoming wavefront by the target. This would be as if there were no obstacle placed in the path of the incoming wave. Diffractive processes are therefore those in which the flux which leaves the interaction region is less than that which entered. The remaining flux is absorbed by the target.

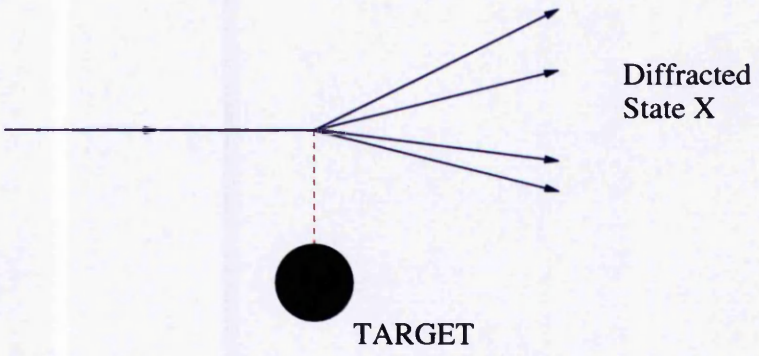

Figure 4.1: A diffractive process arises when the target absorbs part of the wave-front of the incoming wave. This absorption may cause the projectile to dissociate, producing a new, many-particle state X. The produced state, however, may also be comprised of a single new particle. The absorption may also cause the target to dissociate or to be excited into a new single particle state.

All processes in which there is some absorption of the incoming wave by the target are inelastic. All inelastic processes are therefore diffractive. This is true regardless of which family is considered responsible for the scattering force within the framework of Regge theory. In an inelastic scattering process the target particle may change its state and the projectile particle may also leave the interaction region in a different state. A diffraction process in which the projectile is 'diffracted' into a new state X, comprised of several particles, is shown in figure 4.1. It should be noted that a process is defined as being diffractive when there is absorption of the incoming wave by the target. This may occur in a process in which the same particles leave the interaction region as those that entered (in this case the process is often referred to as an elastic diffraction process). Likewise the target may dissociate or be excited into a new, single particle state, but it may also remain intact.

To incorporate absorption in the quantum mechanical treatment of the scattering process the phase shifts in the partial wave expansion, which were previously considered to be real, are now replaced by complex phase shifts

$$\delta \rightarrow \delta + i\beta.$$

The expression for the partial wave amplitudes now alter and become

$$a_l(k) = \frac{\eta_l \sin 2\delta_l}{2k} + i\frac{1 - \eta_l \cos 2\delta_l}{2k}$$

where $\eta_l = \exp -2\beta_l$. The expression for the total cross section arising from the scattered wave now becomes

$$\sigma_{scat} = 4\pi \sum_l (2l+1)\frac{1 + \eta_l^2 - 2\eta_l \cos 2\delta_l}{4k^2}.$$

The total cross section, however, obtained using the optical theorem is now

$$\sigma_{total} = \frac{\pi}{k^2} \sum_l (2l+1)[2 - 2\eta_l \cos 2\delta_l]$$

and this is not equal to the cross section arising from the scattered wave. The difference is the cross section for absorption which does not appear in the final state. It is given by

$$\sigma_{abs} = \frac{\pi}{k^2} \sum_l (2l+1)[1 - \eta_l^2].$$

There is no absorption when the imaginary part of the phase shift is zero, as expected. Absorption is at its maximum when $\eta_l = 0$. This occurs as the imaginary part of the phase shift tends to infinity. When absorption is at its maximum the cross section arising from the scattered wave does not equal zero. There is still some scattering even if the target absorbs all of the part of the incoming wavefront incident upon it.

If one now takes the target to be a disc of radius a and considers the simple case in which there is maximum absorption of the wavefront in the region of target, but no absorption outside of this region, then the scattered differential cross section $d\sigma/d\Omega$ may be shown to tend to a diffraction pattern, as the energy of the incoming beam k is increased. As in diffraction off a black disc in optics the first minimum occurs at $\theta = 1/ka$. The produced diffraction pattern may therefore be used to extract information on the typical size of the target. The extension of quantum theory to relativistic energies was developed within the framework of Regge theory in chapter 2. Here the phase shifts become contained in the residues $\beta_i(t)$ of a Regge pole. Apart from a constant factor the residues have the following behaviour

$$\beta_i(t) \sim a_l(t)(1 - \alpha_l).$$

The residue of a Regge pole will therefore also tend to a diffraction pattern through its dependence on the partial wave amplitude.

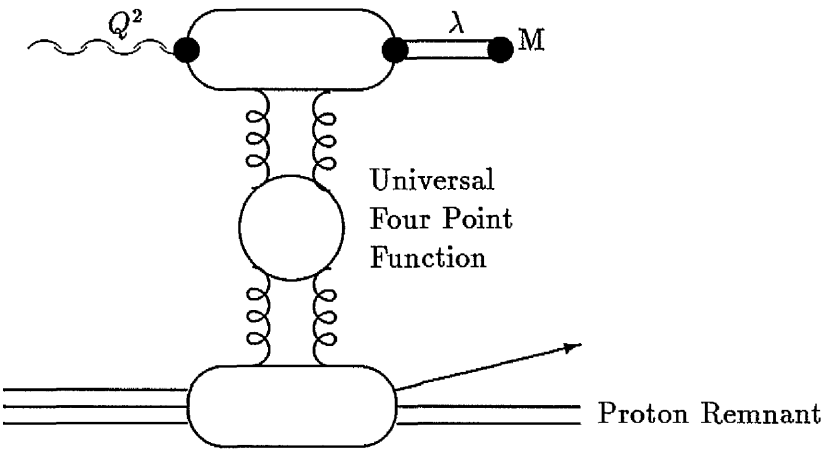

Figure 4.2: The Feynman diagram of the pomeron mechanism of interest in high t vector meson production at HERA. This picture is valid for any vector meson polarisation state λ and for subsequent vector meson decay process, described here by the matrix M. The ovals represent impact factors.

It has already been discussed in chapter 3 that pomeron behaviour in QCD differs from that of Regge theory. The derivation of cross sections in QCD is much more complicated than in Regge theory however some derivations have been completed. It has recently been shown that the QCD differential cross section for the diffractive production of vector mesons is not expected to be restrictively small at those energies accessible to the HERA collider [42].

To derive an expression in QCD for the differential cross section $d\sigma/dt$ at HERA the impact factors for the coupling of the pomeron to the incoming photon and to the incoming proton are needed. At the upper vertex the universal four point function can only be joined to the photon if the photon contains quarks. The photon, however, does not have any quark constituents in the quark model. The photon, however, a somewhat unusual object which sometimes behaves as a point-like particle and sometimes displays hadronic properties. This is accounted for by assuming that the photon is able to fluctuate into vector meson states, quark-antiquark combinations which have the same properties as the photon, in a vector meson dominance model [43]. It is assumed therfore that the photon fluctuates into a vector meson some long time before it interacts with the proton (Fig. 4.2).

A second problem, however, is then that the light-cone wave function of the vector meson is needed to calculate the impact factor. This is the wavefunction of the vector meson written in light-cone coordinates. The form of this wavefunction, however, is not known in any coordinate system (a measurement of the shape of the cross section, however, would give equal insight into this function). In terms of the light-cone coordinate system the p^0 and p^3 components of a four-vector p^μ are replaced by p^+ and p^-, the diagonal axes in the p^0p^3-plane, to give

$$p^\mu = (p^+, p^-, p^1, p^2).$$

The new coordinates are given by

$$p^\pm = (p^0 \pm p^3)/\sqrt{2}.$$

The light-cone coordinate system is particularly useful since, because the covariant square is then

$$(p^\mu)^2 = 2p^+p^- - p_T^2,$$

for a particle on mass shell

$$p^\pm = \frac{p_T^2 + m^2}{2p^\mp}.$$

Therefore p^- and p^+ must both be positive and it becomes a simple matter to extract the on-shell behaviour of particles from the wavefunction. The wavefunction is assumed to be a particular delta function (one which partitions the light-cone momenta and the transverse momenta of the quark-antiquark pair from the photon equally) which is expected to be only valid for heavier vector mesons, such as the J/Ψ and the Υ [44]. With these assumptions in place it is then possible to calculate an impact factor at the upper photon vertex.

The perturbative QCD expansion for the pomeron discussed in the previous chapter is only valid when it is possible to guarantee the dominance of short range physics (so that constituent-constituent interactions may be considered). This becomes true when the legs of the pomeron ladder become close together. The pomeron then only couples to a single quark inside the proton. It may be shown that the occurs when t becomes larger than about $t = -1$ GeV^{2}c^{-2}. At high $|t|$ no further changes are needed at the pomeron-proton vertex. The impact factor is unity since the universal four point function already describes pomeron exchange between quarks.

The impact factors may now be used to derive the differential cross section for vector meson production. The expression will only be valid at high-|t|. At high-|t| the proton will receive a large 'kick' and this is expected to smash the proton apart. The proton dissociative process is therefore expected to dominate over the proton intact process. If the proton changes its state the process is diffractive. The leading log expansion of the previous chapter, however, applies to very high centre-of-mass energies of the photon-proton system ($W_{\gamma p}$). At the HERA collider, however, these centre-of-mass energies take lower values and the cross section calculated using the full BFKL series is therefore not expected to describe HERA scattering processes. Which terms are of importance at HERA energies can be obtained by writing the perturbation series in terms of the rapidity gap (y) between the outgoing struck quark and the outgoing vector meson.

The rapidity gap between the outgoing struck quark and the outgoing vector meson is related to the separation in the polar angles of these two produced particles. The absolute rapidity η of a particle is related to its polar angle θ as follows

$$\eta = \frac{1}{2}\log\left(\frac{p^+}{p^-}\right).$$

Rapidity is a particularly useful quantity for hadron-hadron collisions since it simplifies relativistic calculations involving boosts. Since

$$p^+ = e^{\eta}(p^2 + M^2)^{\frac{1}{2}}/\sqrt{2}$$
$$p^- = e^{-\eta}(p^2 + M^2)^{\frac{1}{2}}/\sqrt{2}$$

when, for example, a boost along the positive z-axis is considered in the centre-of-mass frame the first and second components of a particle's four vector become

$$p^+ \rightarrow e^{w}p^+$$
$$p^- \rightarrow e^{-w}p^-$$

since $\eta \rightarrow \eta + w$. The transverse component remains unchanged. Rapidities can therefore be simply added to consider other relativistic frames of reference. In the high energy limit, in which the particle's mass becomes negligible, the formula for rapidity reduces to

$$\eta = -\log\left(\tan\frac{\theta}{2}\right).$$

In this limit rapidity is referred to as pseudorapidity. Since the energies of the outgoing particles participating in the diffractive process at HERA are expected to be high, their masses may be neglected. The separation in rapidity, or theta, however, between the outgoing struck quark and the outgoing vector meson, is unlikely to be equivalent to the separation of the proton remnant and the vector meson which would be measured in the final state since the struck quark and the unstruck quarks must somehow develop into a broad proton remnant jet and no satisfactory model of how this occurs exists.

Once the BFKL series is expressed in terms of the rapidity gap between the outgoing struck quark and the outgoing vector meson it becomes clear that it is actually a series in $\alpha_s y$. Since the typical size of the rapidity gap increases with photon-proton centre-of-mass energy W, the higher W is, the more the higher terms in the series will become important. At lower values of W only the first few terms are expected to apply. In addition the typical size of the rapidity gap need not be particularly large at these energies. The rapidity gap also depends on the fraction of the target's momentum carried by the parton struck inside the target. If a low momentum object is struck then the rapidity gap is expected to be small, regardless of the value of W. To obtain more realistic approximations for the cross section at HERA the one-loop diagram is taken and iterated using the BFKL equation to generate the first few terms. The diagrams which were neglected in the derivation of the BFKL series may now become important at these lower centre-of-mass energies and so these are once again examined. It appears, however, that they do not need to be included at HERA energies.

In the course of the calculation it becomes useful to define two extra variables. The first variable τ is given by

$$\tau = \frac{-t}{(Q^2 + M_V^2)}$$

and is referred to as the scaling variable. The second, z, is given by

$$z = \frac{3\alpha_s}{2\pi} \log\left(\frac{x_g W^2}{-t + Q^2 + M_V^2}\right)$$

and is referred to as the energy variable. Here Q^2 is the photon virtuality, M_V is the mass of the produced vector meson and x_g is the fraction of the proton's momentum carried by the struck constituent. The QCD predictions for the photon-proton differential cross section $d\sigma/dt$ multiplied by t^4 are plotted as a function of

the scaling variable for different values of the energy variable and for photons which are transversely polarised in figure 4.3. The predictions for longitudinally polarized photons may be obtained from the cross section for transversly polarised photons according to

$$\sigma_L = \left(\frac{Q}{M_V}\right)^2 \sigma_T$$

The extra factor arises from the difference between the calculated flux of transversely polarised photons and longitudinally polarised photons arising from the incoming lepton at HERA. The cross section for longitudinally polarised photons may be neglected for low photon virtualities. The dotted line corresponds to the two-gluon exchange diagram, the dashed line is the result up to the first iteration of the BFKL equation, the solid line represents the result up to the second iteration and the diamonds represent the result up to the third.

The QCD predictions for HERA energies are lower than those of the full BFKL series. They apply to all virtualities of the incoming photon. The dominant contribution to the total lepton-proton cross section at HERA, however, comes from events in which an almost-real photon is radiated from the electron before interacting with the proton. These collisions, in which the virtuality of the photon is small (Q^2 less than about 4 GeV^2c^{-4}), are referred to as photoproduction events. Since a higher cross section would be expected to be measured in this kinematic region it is selected here for analysis. An almost-real photon and a proton then enter the interaction region. Any vector meson may be produced at the photon vertex, however the calculation is expected to be particularly valid for the heavier vector mesons. The J/Ψ vector meson, which has a mass of about 3.1 $GeVc^{-2}$, is chosen here and the region which is then accessible to this analysis lies in the region $0.1 < \tau < 1.0$.

The J/Ψ vector meson is a particularly good choice. This is because the mass of the J/Ψ introduces an additional hard-scale providing a second reason to expect the validity of the perturbative approach. The J/Ψ resonance was discovered in November 1974 in total electron-positron differential cross sections measured at the Stanford Linear Accelerator Centre (SLAC), just outside San Francisco. In the same year the same resonance was observed at Brookhaven National Laboratory (BNL) by forming the invariant mass of final state electron-positron pairs produced when an electron, a proton and Boron come together and interact. Of particular interest was that the resonance peak had a very narrow width.

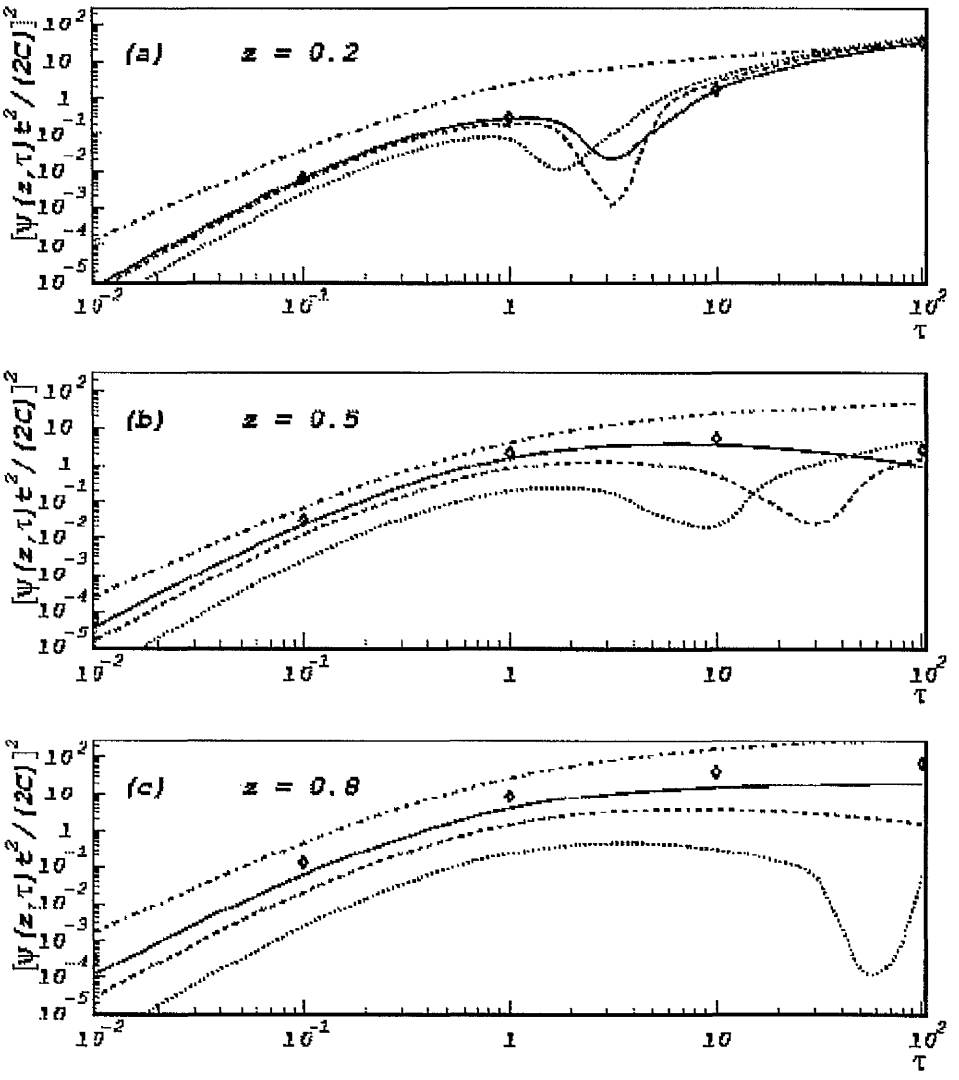

Figure 4.3: Predictions for the differential cross section for diffractive vector meson production divided by t^4 as a function of the scaling variable τ for different values of the energy variable z. The incoming photon is transversely polarised. The dotted line corresponds to the two-gluon exchange diagram, the dashed line is the result up to the first iteration of the BFKL equation, the solid line represents the result up to the second iteration and the diamonds represent the result up to the third. The region accessible to this analysis lies in the range $0.1 < \tau < 1.0$.

The width of a resonance peak is determined from its decay modes. Heavier particles are therefore expected to have larger decay widths than lighter particles because there are a larger number of smaller mass particle states to which they can decay. This general rule, however, is not true of all particle states. Consider, for example, the ω and the ϕ states, both of which are vector mesons states with similar properties and similar decay modes. The ω has a larger decay width than the ϕ, despite the fact that the ϕ has a larger mass. In addition, if just the decays of the ω and the ϕ to three pions are investigated, the ω has a partial decay width of more than an order of magnitude larger than that of the ϕ. There must therefore be something in the underlying dynamics which inhibits the decay of the ϕ to three pions. The exact process which inhibits the decays of certain particle states is not fully understood but it may characterised by a rule, which is referred to as the Zweig suppression rule [23]. The Zweig suppression rule states that if the feynman diagram for a decay process includes disconnected quark lines then the process is inhibited. A diagram contains disconnected quark lines if one or more hadrons can be isolated by a line which does not cut any quark lines. This is the case for the strong decay modes of the J/Ψ. The main decay modes of the J/Ψ are then to an electron-positron pair and to unlike sign muon pairs. The branching ratios of the electron and muon channels are expected to be the same due to lepton universality. The decay of the J/Ψ to the D^0 states is already forbidden due to energy conservation.

4.1 Comparison of the Regge Theory and QCD Predictions.

The QCD prediction for the behaviour of the differential cross section $d\sigma/dt$ as a function of t for diffractive J/Ψ photoproduction may be extracted from figure 4.3. In the region up to $\tau \approx 1.0$ the plotted function is essentially linear with an intercept of zero. This function is therefore essentially proportional τ, and therefore to t, regardless of the value of z. The differential cross section, obtained by dividing this function by t^4, then has a t^{-3} dependence. The cross section will never equal zero. The form of the cross section does not depend on α_s, however the absolute height of the cross section does through the energy variable z. The coupling constant has not been allowed to run in the derivation of this result.

At the beginning of this chapter it was explained that the phase shifts must be replaced by imaginary phase shifts to consider absorption (diffraction) in the quantum mechanical description of the scattering process. In the simple case of diffraction off a black disc it was stated that the differential cross section at high energies is expected to be a diffraction pattern. In the course of extracting the quantum behaviour at relativistic energies using Regge theory, as discussed in chapter 2, the phase shifts become contained in the residues of the Regge poles. A diffraction pattern, becoming clearer as s is increased, multiplied by the asymptotic s-dependence is then expected in Regge theory.

The first major difference between the Regge and QCD approaches is therefore that the diffraction pattern has disappeared in the course of the QCD derivation. A second major difference is that the differential cross section in Regge theory is expected to drop to zero. This occurs firstly at values of t which correspond to integer values of angular momentum. As explained in chapter 2 the residues must equal zero at these values of t so that the amplitude decouples. This was because no physical particles are expected to exist in the region of negative t (since the mass would have to be imaginary so that when squared it gives a negative result). Secondly, there are zeros corresponding to minima in a difraction pattern, which may be extracted by considering scattering at high energies.

Perhaps the most significant difference is that Regge theory bases its predictions on a family of bound-state particles with the quantum numbers of the vacuum. No bound-state particles were included, however, in the extraction of the behaviour of the pomeron in QCD. Should these bound-state particles exist however they would be expected to participate in the diffractive process at HERA energies.

4.2 Selection at the Photon Vertex.

A useful variable which enables events in which only a single particle is produced at the photon vertex to be selected is the elasticity variable z. At HERA this is defined as follows

$$z = \frac{P^\mu \cdot v^\mu}{P^\mu \cdot q^\mu}.$$

Here P^μ represents the four-vector of the incoming proton, q^μ the four-vector of the incoming photon and v^μ the four-vector of the state produced at the photon vertex. The elasticity variable may take values ranging between zero and one. In the rest frame of the incoming proton and for those photoproduction processes in which the outgoing particle is produced almost collinearly with the incoming photon the photon elasticity represents the fraction of the photon's energy which is carried by the produced particle. If z is equal to one in this case then all of the photon's energy is passed to the outgoing colinearly produced particle.

The elasticity variable is a relativistic invariant. This is because it is defined in terms of scalar products of particle four-vectors. Since every such scalar product is a relativistic invariant, the elasticity variable must also be invariant. An expression relating t to the photon elasticity in the lab frame at H1 is required here. At H1 the four vector of the incoming proton is written as

$$P^\mu = (E_p, 0, p)$$

since the photon approaches along the positive z-direction. The second component represents the transverse momentum of the proton and the third the longitudinal momentum. In photoproduction the photon may be assumed to approach the proton head on since the lepton suffers only a small deflection. The four-vector of the incoming photon may therefore be written as

$$q^\mu = (E_q, 0, q).$$

The longitudinal momentum component q is negative since the photon approaches in the negative z direction. Since the outgoing particle may be produced in any general direction its four-vector is written as

$$v^\mu = (E_v, v_t, v_l).$$

The Mandelstam variable t is given by

$$t = (v^\mu - q^\mu)^2$$

and this may be expanded as follows

$$t = v^2 + q^2 - 2v^\mu \cdot q^\mu$$

The third term may be written as

$$2v^\mu \cdot q^\mu = (E_v + v_l)(E_q - q) + (E_v - v_l)(E_q + q).$$

By noting that at high energies the proton's mass will be negligible in comparison to its momentum the factors $(E_q - q)$ and $(E_v - p)$ may be written as

$$(E_q - q) = \frac{q^\mu \cdot P^\mu}{p}$$

and

$$(E_v - p) = \frac{P^\mu \cdot v^\mu}{p}.$$

The third term therefore simplifies to

$$2v^\mu \cdot q^\mu = (E_v + v_l)\frac{q^\mu \cdot P^\mu}{p} + \frac{P^\mu \cdot v^\mu}{p}(E_q + q).$$

Both terms may now be multiplied by unity giving the following expression

$$2v^\mu \cdot q^\mu = (E_v + v_l)\frac{(E_v - v_l)}{(E_v - v_l)}\frac{q^\mu \cdot P^\mu}{p} + \frac{P^\mu \cdot v^\mu}{p}\frac{(E_q - q)}{(E_q - q)}(E_q + q).$$

It is now possible to perform some cancellation giving

$$2v^\mu \cdot q^\mu = (E_v^2 - v_l^2)\frac{q^\mu \cdot P^\mu}{P^\mu \cdot P^\mu} + \frac{P^\mu \cdot v^\mu}{P^\mu \cdot q^\mu}(E_q^2 - q^2).$$

If the produced particle is a vector meson state of mass M_v then

$$E_v^2 - v_l^2 = M_v^2 - v_t^2.$$

Similarly the square of the photon four vector is

$$E_q^2 - q^2 = -Q^2$$

where Q^2 is the magnitude squared of the photon four-vector squared. The third term therefore becomes

$$2v^\mu \cdot q^\mu = (M_v^2 - v_t^2)\frac{1}{z} - zQ^2.$$

The Mandelstam variable t is therefore

$$t = -\frac{1}{z}P_t^2 - (1 - z)Q^2 + (1 - \frac{1}{z})M_v^2.$$

In photoproduction $Q^2 \sim 0$ so

$$t \sim -\frac{1}{z}P_t^2 + (1 - \frac{1}{z})M_v^2.$$

It is clear that when the elasticity variable is close to unity, t is given by

$$t \sim -P_t^2.$$

The photon elasticity may be written for high energies of the incoming proton as

$$z = \frac{(E - P_z)_v}{(E - p_z)_\gamma}.$$

Since energy and momentum are conserved this must be equivalent to

$$z = \frac{(E - P_z)_{J\backslash\Psi}}{\sum(E_i - p_i^z)} \tag{4.1}$$

where the sum runs over all particles found, including the J/Ψ, but excluding the scattered positron [45]. Thus, at HERA, the photon elasticity of a collision may be reconstructed from the four-vector of the detected vector meson and the $(E - p_z)$ of the event.

4.3 Selection at the Proton Vertex.

A similar expression for t may be derived at the proton vertex. Here t is given by

$$t = (P_r^\mu - P^\mu)^2$$

where P_r^μ represents the four-vector of the proton remnant. This may be expanded as follows

$$t = (P_r^\mu)^2 - 2P^\mu \cdot P_r^\mu$$

where the mass of the proton has again been negected. If the proton dissociates then the square of the proton remnant four vector is given by the square of the effective proton remnant mass M_{PR} (obtained by summing all the energies of the particles produced in the jet and subtracting the sum of their momentum components). The elasticity variable z may be rewritten using

$$v^\mu + P_r^\mu = q^\mu + P^\mu$$

giving

$$z = \frac{(q^\mu \cdot P^\mu) - (P_r^\mu \cdot P^\mu)}{(q^\mu \cdot P^\mu)}.$$

The expression for t in terms of z is therefore

$$t = M_{PR}^2 - 2(q^\mu \cdot P^\mu)(1 - z).$$

Since at high energies $E_p = P_z^p$ and since, in photoproduction, the photon is emitted essentially colinearly with the negative z-axis, the final expression for t at the proton vertex is

$$t = M_{PR}^2 - 4E_\gamma E_p(1 - z).$$

At values of z close to unity the expression for t reduces to the proton remnant mass squared.

It has already been stated that the reason this process is known to be diffractive is because the proton changes its state in the interaction. It has also been made clear that the size of the rapidity gap between the proton remnant and the produced vector meson cannot be predicted, since no satisfactory model of how the proton breaks up exists, and since the rapidity gap between the struck quark and the outgoing vector meson cannot be predicted unless the momentum fraction of the struck constituent is known. A selection based on a restriction on the size of the rapidity gap, therefore, would simply select events with a large gap in the final state (the central maximum of the diffraction pattern). The contribution from diffractive events with smaller or moderate rapidity gaps will then be lost. Large rapidity gaps may also occur in other processes in which there is no absorption of the incoming wave but in which a J/Ψ vector meson is also produced at the photon vertex. These non-diffractive events would pass such a selection procedure and contaminate the result. No restriction is made on how wide the rapidity gap in this analysis. Proton-elastic and proton-inelastic final states must therefore be carefully separated after the selection has been made. Since at high-$|t|$ the proton is expected to predominantly dissociate it is expected that the behaviour of the diffractive cross section will be well represented by the cross section measured using only proton-dissociative events.

Chapter 5

The H1 Detector at HERA.

The HERA lepton-proton collider was designed to perform a deeper investigation of the substructure of the proton. It is located in Hamburg at DESY (Deutsches Electronen Synchrotron), the German National Laboratory for Elementary Particle Physics, which was founded in Hamburg on the 18th December 1959. The collider was built at DESY between 1984 and 1989 in a 6.3 kilometre tunnel under part of the city of Hamburg and began operating in 1990-1991. It remains the only lepton-proton colliding beam experiment worldwide. In July 1994 the lepton beam was swapped from an electron to a positron beam. The experiment operated as a positron-proton collider during 1997 during which time it collided beams of 27.6 GeV positrons with beams of 820 GeV protons. The different beam energies are required because positrons radiate more energy than protons, via synchrotron radiation, when confined to a circular orbit.

To reach their required beam energy, positrons are accelerated to 500 MeV in a linear collider. They are then collected in a small storage ring before being injected into a second ring, referred to as the DESY II ring. Here they are accelerated further to 7 GeV before being passed, in bunches, to the PETRA II ring. Here the bunches are accelerated to 14 GeV before being injected into the HERA ring where they are accelerated further to their final energy of 27.6 GeV. To obtain the required 210 bunches in the HERA positron ring the entire process has to be repeated three times. A magnetic field of 0.165 T holds the positrons in their circular orbits. This magnetic field is provided by dipole magnets.

To generate the proton beam, protons are first obtained from Hydrogen atoms. To remove the single electron of the Hydrogen atom a charged foil is used. Protons are initially accelerated to 50 MeV in a linear accelerator. They are then injected into the storage ring DESY III where they are accelerated to 7.5 GeV. From there they are passed in bunches into the PETRA II ring and accelerated further to 14 GeV before being finally passed to the HERA ring itself where they are finally accelerated to 820 GeV. To acheive 210 proton bunches this process also has to be repeated three times. Because of the higher mass of the protons a higher magnetic field of 4.68 T is required to hold them in their circular orbit. This magnetic field is provided by superconducting magnets. A new positron beam has to be generated several times during the time that the proton beam is present in the HERA beam pipe since the positrons in the positron beam eventually lose their energy via synchrotron radiation.

The particles are accelerated to their respective energies in two separate beam pipes within the same tunnel at HERA. The beams circle the tunnel in opposite directions and are brought together into a single beam pipe at four different points. A detector is located at each of these points. The H1 detector observes the product of collisions which then occur at one of these four locations. The positron and proton bunches pass through each other once every 96 nanoseconds. When two bunches pass through each other interactions may, but do not always, occur. A positron-proton collision takes place about once every 10^5 bunch crossings.

5.1 The H1 Detector.

The layout of the H1 detector is shown in figure 5.1. The asymmetry of the detector arrangement is required due to the much larger energy of the proton beam. The axes are defined such that the proton beam is incident in the positive z, or forward, direction. In spherical polar coordinates theta is then zero in the forward direction. The H1 detector is a general purpose detector and the subdetectors and their arrangement are therefore chosen to cover many different final states which may arise from a scattering process. The H1 detector was especially designed to provide good lepton identification, especially electrons, high granularity for jet reconstruction and good hermicity for the recognition of events with missing trans-

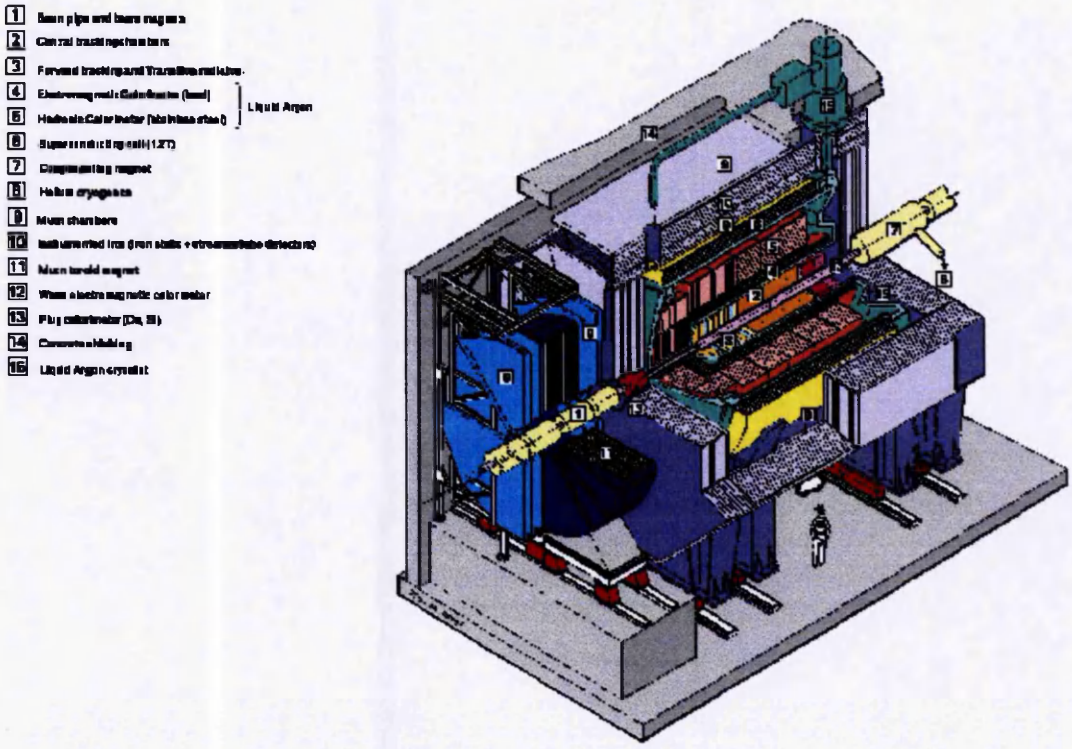

Figure 5.1: An overview of the H1 detector at HERA. Tracking detectors are placed closest to the interaction point surrounded by calorimeter sections. These are both contained inside a superconducting magnet. Muon detectors are placed outside of this magnetic field.

verse energy. A good multipurpose trigger system and good hadron calorimeters are also installed. A superconducting coil of radius 3m provides a magnetic field of 1.15 T at the centre. Within the coil are drift chambers, proportional chambers, electromagnetic and hadronic calorimeters and scintillation counters. The positron beam may be used as a source of photons to investigate photon-proton collisions. At HERA the virtuality of the photon may reach values of up to about two orders of magnitude higher than was previously available. The parts of the H1 detector underwent extensive upgrade during 1994. In particular a new calorimeter was located in the backward region. The H1 collaboration which built and operates the detector is comprised of about 400 scientists from 39 institutes of 12 countries throughout the world.

This chapter describes the general operation and construction of the components of the H1 detector which were used in the analysis presented in this thesis. A more detailed description of these components and the entire H1 detector may be found elsewhere [46].

5.2 Electron and Positron Identification using H1 Calorimeters.

A calorimeter is a form of particle detector which is used to measure the energy of a particle entering it. By inducing, in some way, a particle shower, a calorimeter then periodically monitors the development of that shower. The energy of the particle which entered the detector may then be reconstructed from the quantity which was periodically measured. The material which is used to initiate the shower, and the method of monitoring the shower's development, may vary, however the principle is the same in all different types of calorimeter.

In general a particle shower is initiated in a calorimeter by some active material. The characteristics of the shower which then develops depends upon whether the incident particle was leptonic or hadronic. If a leptonic particle, such as an electron or a positron, with an energy above about 100 MeV enters such a material it will then lose energy predominantly via the brehmstrahlung process, since the cross section for this process dominates in this energy range. The electron or positron then emits a photon which carries off some of the energy of the initial particle. If the photon, however, is emitted with an energy also above 100 MeV then it is expected to eventually produce an electron-positron pair. As long as the produced electrons, positrons and photons have energies above 100 MeV these processes are expected to continue and the number of leptons in the material will increase. A particle shower therefore develops. Eventually, however, the energies of the individual particles produced in the shower will begin to fall below about 100 MeV. These will then start to dissipate energy, predominantly through ionization and excitation processes, via interactions with the atoms of the active material. Eventually all of the energy will be lost through these ionisation processes. A measurement of the total ionisation in the material is then equivalent to the incident particle's energy.

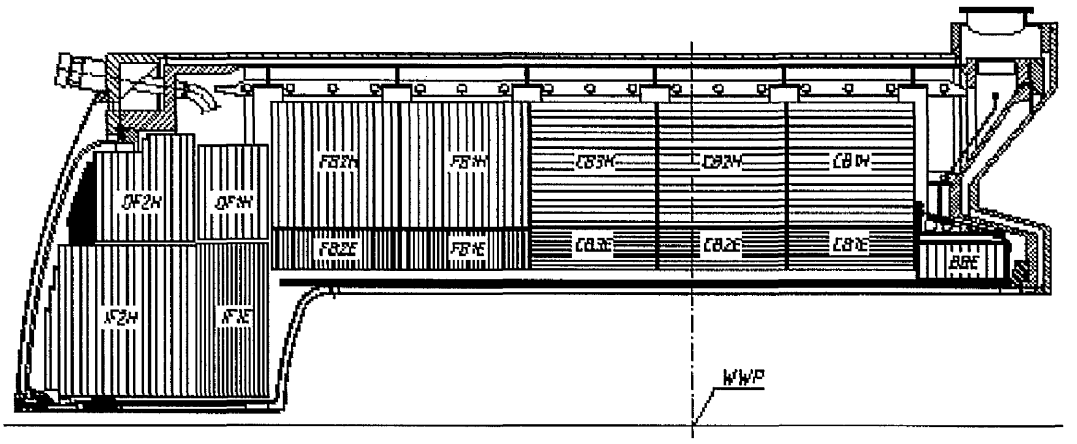

Figure 5.2: The sectioning of the H1 liquid Argon calorimeter. The hadronic sections lie further away from the interaction point (WWP) than the electromagnetic sections. The electromagnetic and hadronic sections are both thicker in the forward region due to the higher energies of the particles expected to be produced in this region.

A hadronic particle entering the active material, however, is expected to form showers predominantly through inelastic nuclear collisions. The particles in the shower then continue to take part in further such collisions until their energies fall once again below a certain threshold. Showers formed by hadronic particles typically take longer to develop and are typically wider than showers formed by leptonic particles (hadronic showers typically contain electromagnetic showers within them). Information as to whether the incident particle was hadronic or leptonic may therefore be obtained from the characteristics of the shower which developed in the active material.

5.2.1 The Liquid Argon Calorimeter.

The main calorimeter at H1 is the liquid argon calorimeter. This covers the polar angular range $4° < \theta < 154°$. Its active medium is argon cooled to a temperature of -183 degrees celsius. The volume of liquid argon used is about $40m^3$.

Steel and lead plates are used to induce showers and charge is collected and read out from rectangular cathode pads. The calorimeter is divided into a number of sections to enhance the speed at which the collected signals can be read out and to enable positional information to be obtained. The sectioning of the liquid-argon calorimeter is shown in figure 5.2. The cathode pads vary in size depending on the expected number of particles that will be produced in a particular region. The electromagnetic part of the calorimeter is also thicker in the forward direction since the particles produced in this region are expected to have higher energies [47].

5.2.2 The Lead-Scintillating Fibre Calorimeter (SPACAL).

During the shutdown over the winter of 1994-95 the H1 detector underwent an extensive upgrade programme. As part of this upgrade a new calorimeter was installed in the backward region. It was installed due to the interest in low-Q^2, deep inelastic scattering events, in which the scattered positron ends up in the backward region of the main part of the detector. An investigation of these events was at that time restricted by the energy and angular resolution of the so-called BEMC calorimeter covering this region. To improve the accuracy with which low-Q^2, deep inelastic scattering events could be analysed, an energy resolution of at least 2% for electrons with energies greater than 30 GeV and an angular resolution of between 1 and 2 milliradians was required. The lead-scintillating fibre technique was chosen because the calorimeter would be operating in a high magnetic field and had to be fitted into the limited space occupied by the existing calorimeter. A lead-fluoride crystal technique was also considered, but was rejected because of the high cost of lead-fluoride crystals and because of their poorer hadronic energy resolution.

The design of the calorimeter pays particular attention to the region near the beam pipe where the scattered electron appears in the transition region from low-Q^2, deep inelastic scattering events to photoproduction events. A plug section covers the low emission angle region. The detector was designed to have a high granularity in anticipation of the increase in HERA luminosity. When a particle enters the calorimeter a shower is initiated by the lead. Scintillation light is read out along fibre optic cables. The position of the SPACAL calorimeter is shown, together with the tracking detectors which will be discussed in the next section, in figure 5.3.

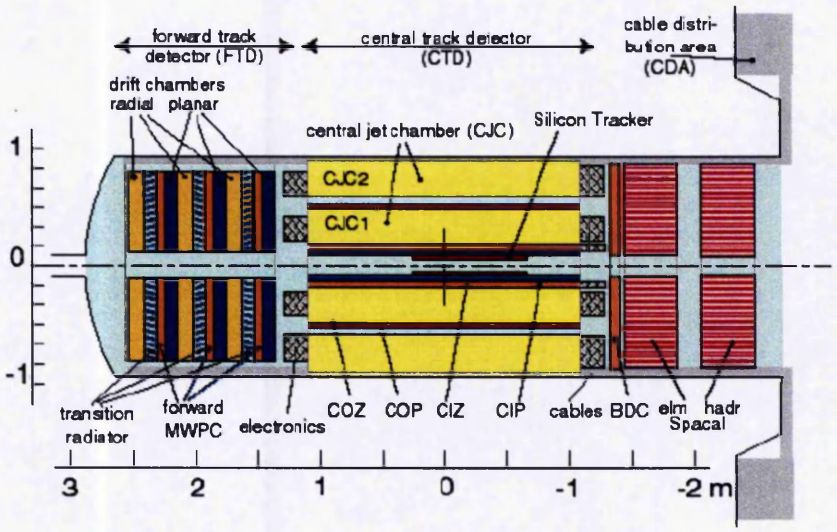

Figure 5.3: The positions of the components of the H1 tracking system and of the SPACAL calorimeter. The tracking detectors are divided into a central and a forward region.

5.3 Electron and Positron Identification using H1 Drift Chambers.

As is typical of many large collision experiments the H1 detector at HERA makes use of a magnetic spectrometer set up. A magnetic spectrometer system is one which contains a series of detectors that measure the position of a particle as it is deflected by a magnetic field. The deflection of the particle as it passes through this region may be used to determine the charge of the particle. In addition, the curvature of the path, or track, that the particle follows may be used to determine the particle's momentum. Position measurements may be made using a segmented calorimeter, however an improved accuracy is obtained when drift chambers are used. In a typical drift chamber a uniform electric field is applied to a region which contains a gas. When a particle traverses the chamber it ionizes gas atoms, freeing electrons which then drift towards the anode and give a signal.

The position at which a particle passed through the drift chamber may be better determined if a series of anodes, for example a series of anode wires, are used. When a signal occurs in one of the anode wires the position at which the particle passed through the drift chamber is then known to within the spacing of the wires. To obtain the distance from the wire at which the particle passed through the detector it is necessary to know the drift velocity and the length of time that elapsed before the ionisation electrons reached the anode. For this reason drift chambers are often used together with scintillation counters which provide a much faster signal when a particle passes through and gives a good initial time measurement. By measuring the difference between the initial scintillation pulse and the time at which the drift chamber pulse occurred it is then possible to calculate the length of time in which the ionisation electrons were drifting.

The drift velocity depends upon the particular gas mixture used. Which particular gas mixture is most appropiate depends strongly on its intended application. Gases with high drift velocities are used in high particle rate environments. Gases with a low specific ionisation would be used to minimise multiple scattering. The minimum requirement of the readout electronics is to be able to distinguish which anode wire gave a signal. It is also often possible however to read the signal from both ends of the wire. If the charge is collected closer to one end of the wire than the other then, since the signal will take longer to reach one end of the wire than the other, the position of the signal along the wire's length may also be measured.

There are essentially three major designs of drift chamber. These are planar chambers, cylindrical chambers and proportional drift tubes. Cylindrical chambers are frequently used in colliding beam experiments since they may be positioned such that they almost completely surround the interaction point. Planar drift chambers are then used to cover any gaps left by the cylindrical chamber. Due to asymmetry of the beam energies at HERA a large number of particles tend to be produced in the forward, or positive z, direction. To improve the accuracy and speed of the triggering system it was therefore decided to divide the tracking detectors into two regions, the central and forward regions, as shown in figure 5.3.

5.3.1 The Central Tracking Chamber.

The main components of the central tracking system are two separate cylindrical drift chambers refered to as central jet chamber 1 (CJC1) and central jet chamber 2 (CJC2). In both these detectors anode wires are strung parallel to the beam axis (the z-axis). By measuring the specific energy loss the particle identification is improved. Both these detectors have independent gas volumes. To measure the z-coordinate with a better accuracy two further drift chambers, the central inner z-chamber (CIZ) and the central outer z-chamber (COZ) are included. These have wires strung perpendicular to the z-axis, and the drift direction is parallel to the z-axis.

5.3.2 The Forward Tracking Detector.

The forward track detector was designed to identify charged tracks in the region $7° < \theta < 25°$. It consists of three identical supermodules each of which contains a planar wire drift chamber, a multiwire proportional chamber, a transition radiation volume and a radial drift chamber. The planar drift chambers contain three modules which measure the position at which a particle passes through the detector using four wires each. The multiwire proportional chamber is used for triggering purposes. Transition radiation X-rays are produced in the transistion radiation volume which are then detected by the radial drift chamber. This is determined from the ionisation charge above the normal energy loss value. This region of the H1 detector is particularly hostile for track reconstruction due to the high track multiplicities in this region. The problem is increased by the prescence of a synchrotron radiation collimator in the beam pipe which produces a large number of secondary particles in the first of the supermodules.

5.4 The Luminosity System of the H1 Detector.

The luminosity system of the H1 detector is used for online determination of the instantaneous luminosity, for measuring the total integrated luminosity of a particular data-taking period and also for identifying photoproduction events.

Luminosity measurements at H1 are made by determining either the rate or the number of events arising from the Bethe-Heitler process

$$e^+ + p \longrightarrow \gamma + e^+ + p.$$

A description of how this is done is contained in the section on the determination of the total integrated luminosity for 1997 running conditions in section 6.11. The methods used involve either the simultaneous detection of the final state electron and photon, or the detection of the photon alone. The luminosity system is therefore made up of two main parts, one for detecting positrons (or electrons) and one for detecting photons. The angular distributions of the scattered positron and the outgoing photon for incoming positron energies of about 30 GeV are strongly peaked at angles of approximately 17 μrad with respect to the incoming positron direction, so the detectors have to be placed as close to the beam pipe as possible, in the negative z direction, and far away from the interaction point. The luminosity detectors are permanently calibrated during data taking. One of the main contributions to the systematic error in the absolute luminosity measurement comes from the dependence of the system acceptance on possible variations in the electron beam angle in the interaction region. This beam tilt is typically of order 100 μrad and is controlled by the position of the beam profile at the photon detector with a high precision of the order of 10 μrad.

At HERA the total positron-proton cross section is dominated by the production of photoproduction events. In photoproduction the incoming positron emits an almost-real photon and scatters through a small angle. The definition of almost-real is somewhat arbitrary, however, at HERA any event in which the virtuality of the photon is less than about 4 GeV^2 is usually referred to as a photoproduction event. The electron-positron detectors of the luminosity system may be used to tag photoproduction events in the region $Q^2 < 0.01$ GeV^2. Only photoproduction events corresponding to certain scattering angles of the scattered lepton may be tagged, however, by the electron-positron detectors of the luminosity system. To avoid Bethe-Heitler events it must also be ensured that no photon is simultaneously detected by the photon detector.

5.4.1 The Electron Tagger at z = −33.4 Metres.

The electron tagger located at z = −33.4 metres may be used to tag photoproduction events in the region $165 < W_{\gamma p} < 233$ GeV. The scattered positrons are deflected by bending magnets and a set of low-β quadrupoles which are located in the region $-5.8 < z < -23.8$ metres so that they pass through a window in the beam pipe at z = −27.3 metres and enter the tagger. The electron-tagger is a 7 by 7 array of crystal Čerenkov detectors covering an area of 154 mm by 154 mm. The hodoscope of crystal Čerenkov counters was chosen for its high radiation resistance, good timing, energy and position resolutions and for its compactness.

5.4.2 The Electron Tagger at z = −44.0 Metres.

This electron tagger was installed during the winter shutdown of 1994/95. It may be used to tag photoproduction events in the range $65 < W_{\gamma p} < 163$ GeV. The scattered positrons once again leave the beam pipe through an exit window. The angle between the exit window and the positron beam direction is thirty degrees. Six Čerenkov crystals of the same type and size as used for e-tagger33 are used here. These are housed inside an anti-magnetic box. The crystal Čerenkov counters were chosen for the same reasons as for the e-tagger at z = −33.4 metres [48].

5.4.3 The Photon Detector.

The photons of the Bethe-Heitler process leave the beam-pipe through a window where the proton beam pipe bends upwards at z = −92.3 metres. They then enter the photon detector which is positioned at z = −102.9 metres. A lead filter is used to protect the photon detector from the high flux of synchrotron radiation in this region. This is followed by a Čerenkov detector which acts as a veto counter to eliminate events in which the photon interacts with the filter. The photon detector is a 5 by 5 array of crystal Čerenkov detectors covering an area of 100mm by 100mm. An iron wall 2m thick protects the photon detector from the proton beam. The veto counter is viewed by two phototubes, one for photon detection and the other for charged particle detection.

5.5 Detectors in the Forward Region.

5.5.1 The PLUG Calorimeter.

The PLUG Calorimeter closes the gap between the forward part of the liquid argon calorimeter and the beam pipe at $\theta \approx 0.6$ degrees. The main reasons for closing this gap were to improve energy flow measurements and improve measurements of the missing transverse momentum of an event, important for events in which neutrinos were produced. In addition, however, this detector may be used to investigate if a narrow proton remnant jet occurred and to veto background arising from interactions between the beam and gas and the beam with the wall of the beam pipe. Since only a small space was available only a very compact calorimeter would fit. A calorimeter with nine copper plates interweaved with eight silicon detectors was chosen. The energy resolution of the PLUG calorimeter is restricted by the large amount of dead material in front of it through which particles must pass before they enter the calorimeter and through energy leakage. The resolution is nevertheless sufficient for the purposes for which it was installed. A cross sectional view of the PLUG is shown in figure 5.4.

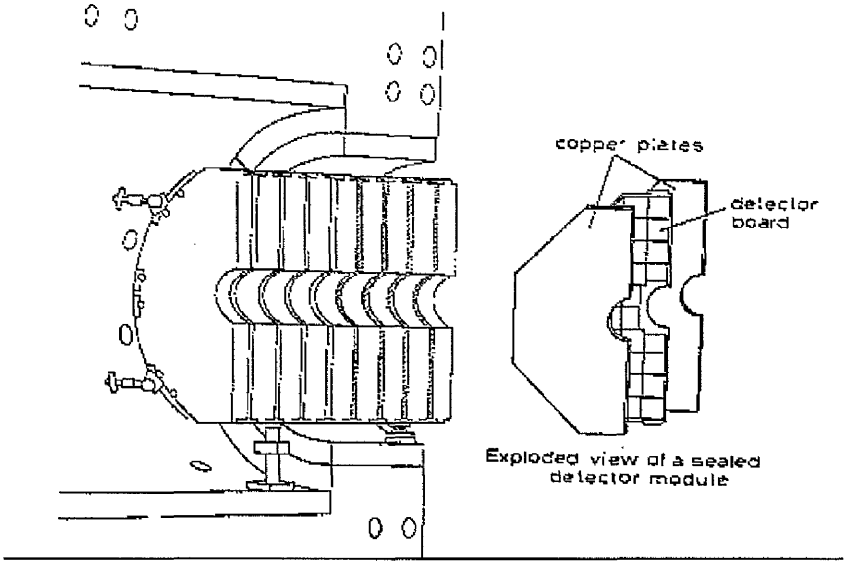

Figure 5.4: A cross section of the PLUG calorimeter together with an exploded view of a calorimeter module.

5.5.2 The Forward Muon Detector.

An additional detector was introduced in the forward region to improve investigations of processes which are identified partly due to the decay of a heavy particle to muons. The distribution of these decay processes are often strongly peaked in the forward region at HERA. Since the proton may dissociate and leave a large number of particle tracks in the forward tracking detectors it is very difficult to isolate which track corresponded to any produced muons. The forward muon detector is a spectrometer that may be used independently of the forward tracker. However, it is usually used to identify which tracks in the forward detectors corresponded to muons. A better measurement of the tracks momenta is made using the forward tracking detectors.

The forward muon detector is positioned outside the instrumented iron return yoke in the forward proton direction. Since it is located in the region outside the magnetic field provided by the H1 superconducting magnet it has a toroidal magnet of its own. Three layers of drift chambers on each side of the toroid obtain the incoming and outgoing directions of the muon and the difference between these directions is used to calculate the muon momentum. The forward muon toroid bends muons in polar angle θ. The orientations of the wires in the drift chambers are rotated with respect to one another to obtain good position measurements. A ϕ layer is sandwiched between two θ layers. A gas mixture of 92.5% argon, 5% carbon dioxide and 2.5% methane is used. The position along a wire is determined from the difference in pulse shapes readout at either end of the wire. The layout of the forward muon spectrometer is shown in figure 5.5.

5.5.3 The Proton Remnant Tagger.

The proton remnant tagger is positioned at z=26 metres. It completely surrounds the beam pipe. It consists of two layers of scintillating material which are sandwiched inside lead shielding.

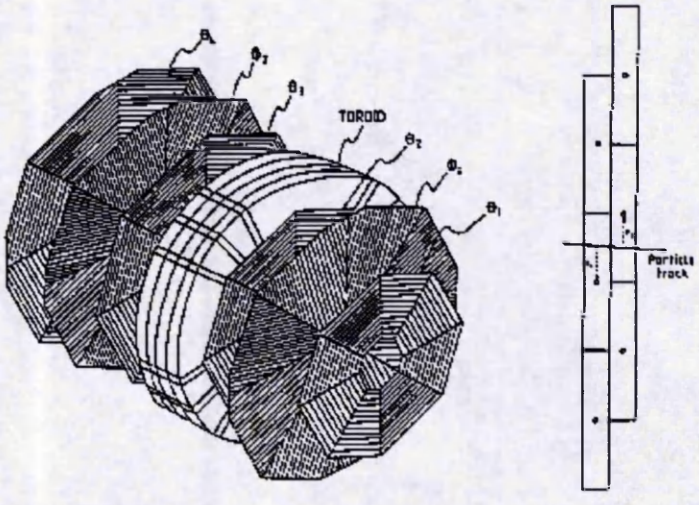

Figure 5.5: The layout of the forward muon spectrometer at H1. Since the forward muon chamber is located outside of the region covered by the H1 superconducting magnet it has a toroidal magnet of its own.

5.6 The H1 Trigger System.

The proton and positron bunches at HERA pass through each other once every 96 nanoseconds. This is much quicker than the typical readout time of the various subdetector elements. In addition, it is not possible to store information from every single collision, some of which will arise from background interactions of the beam with the wall of the beam pipe or the gas in the beam pipe anyway, so some selection as to which collisions are likely to be of interest has to be made.

Each of the various subdetectors of the H1 detector typically provide a trigger element, essentially a logical signal which is ON if something of interest has occured, which is sent to the central trigger. The central trigger then decides whether an event is to be kept. All parts of the detector are synchronised so that the information arrives at the central trigger at the same time. It takes a length of time corresponding to approximately twenty bunch crossings for this information

to arrive at the central trigger. Since the central trigger also needs time to decide all information is stored in a queue, or pipeline, for the length of time it takes for approximately 24 bunch crossings.

To decide if information concerning an event is to be stored the central trigger considers subtrigger elements which are usually comprised of some combination of a few detector trigger elements. If the subtrigger condition is satisfied the event is usually stored. One exception to this general rule occurs when the process which fires the subtrigger occurs fairly frequently. In this case the subtrigger is prescaled with a value P, which varies depending on the frequency of the process, and then in only one of every P firings of the subtrigger is the information stored.

If any subtrigger condition is satisfied, i.e. if an event is recognised which level 1 of the central trigger thinks could be a real event, it sends out a signal which has the effect of freezing all the information stored in the pipeline. This "L1KEEP" signal appears approximately 24 beam crossings after an interesting event actually occured. At this point the second level trigger immediately starts to analyse the subtrigger which caused the "L1KEEP" signal. Within twenty microseconds it decides whether the event should really be stored or not. If the event is then rejected the time lost is only twenty microseconds. Otherwise, the data concerning the interaction is sent from the queue to the central event builder. This takes approximately 2 ms and during this time, since no further information can be stored in the pipeline, collisions are missed.

The central event builder, having collected together all the information concerning the event, makes topological studies of the event after which, if the event is not rejected, passes all the information to the level 4 filter farm which may remove further background processes. Should an event remain after level 4 the event is stored. A four level trigger system is therefore used to select real positron-proton physics events and filter out those events which do not arise from such collisions. A fifth level also exists which may be used once the data has been stored to reduce the data sample further.

Chapter 6

Analysis of the Scattering Force.

Diffractive events which produce a J/Ψ vector meson at the photon vertex are to be selected in the kinematic region of photoproduction. In a photoproduction event the incoming lepton scatters through a small angle, emitting an almost-real photon. At HERA, any event in which the virtuality of the photon is less than about 4 GeV^2c^{-2} is usually referred to as a photoproduction event. There are two methods for identifying photoproduction events using the H1 detector. The first is to demand that a scattered lepton candidate is identified in one of the electron taggers placed far down the beam pipe in the negative z direction. A second method demands that no scattered lepton candidate is identified in the main part of the detector, where it is expected to appear for higher photon virtualities, and to assume that the scattered lepton must have therefore scattered through a smaller angle. The first method is selected here. Photoproduction events are identified by demanding either a scattered lepton candidate in the electron tagger at z=-33.4 metres or the electron tagger at z=-44.0 metres. Since each of these taggers covers a different range of photon-proton centre-of-mass energies, two photon-proton centre-of-mass energy samples are easily identified by sorting the events according to which tagger the scattered lepton hit originated in. A third e-tagger, placed at z=-8.0 metres, is not used here since, because it was installed during 1997, the number of diffractive events it would have selected will be lower than that of the older e-taggers which were present for the entire year. Events with photon virtualities below about 0.01 GeV^2c^{-2} are selected by this method.

Scattered lepton candidates in the e-tagger33 centre-of-mass energy range are defined as being those in which the energy deposited in the tagger was greater than 6 GeV. To remove Bethe-Heitler processes, a maximum energy deposit of 2 GeV is allowed in the photon tagger. These same two values are used to define scattered lepton candidates in the e-tagger44 centre-of-mass range, although the energy resolution of this tagger is poorer. The behaviours in the two centre-of-mass energy ranges, however, are then obtained using essentially identical selection methods and may be compared. If the electron and photon tagger restrictions are met in either centre-of-mass range, but not in both ranges simultaneously, then it is assumed that the scattered lepton did indeed scatter through a small angle and the event is therefore a photoproduction event. Roughly 1.5% of those events which were selected had a hit in both e-taggers and were discarded.

6.1 Selection of Diffractive Events.

Each selected photoproduction event is then analysed to see if it could be a diffractive event and to see if it may contain a J/Ψ vector meson. Before this is done the true interaction point of the event, which is measured by the trigger system by linking tracks to the region close to the nominal interaction point, is considered. If the true interaction point lies near to the nominal interaction point, which corresponds to the origin in the H1 coordinate system, then measurements of track momenta and calorimeter cluster energies will be more reliable. This is because the subdetectors of the H1 detector are orientated in such a way as to cover the region surrounding the nominal interaction point. Only those candidate photoproduction events with a true interaction point which lies within $z = \pm 40$cm are analysed for diffractive J/Ψ characteristics. The number of background interactions of the beam with the beam-gas and of the beam with the walls of the beam pipe, is also expected to be reduced by this restriction since these may occur with interaction points lying outside this range.

If a candidate photoproduction event has a good interaction point the event is then scanned for electron and positron candidates. Electrons and positrons are both expected to deposit almost their entire energy in the electromagnetic part of a calorimeter. In the angular region covered by the SPACAL calorimeter, therefore, a

search is made for isolated electromagnetic clusters. No tracking information is used in this region. In the angular region covered by the liquid-argon calorimeter and the main tracking detectors each track linked to the true interaction point is required to have an electromagnetic cluster associated with it. Since neutral particles do not leave tracks in the tracking detectors, only charged particles will be selected by this procedure. The energy of the electromagnetic cluster is then required to be greater than 70% of the momentum of its associated track.

To determine which two electron-positron candidates most likely originated from the decay of the J/Ψ the following algorithm was chosen. Since in a proton-elastic, diffractive event the final-state proton is lost down the beam pipe, only the two decay products of the J/Ψ should be detected. If the proton dissociates, however, a proton remnant jet will be produced in the forward direction. If this is narrow then the two decay products of the J/Ψ will most likely be the two electron-positron candidates with the largest theta values in the detector. As the proton remnant jet becomes wider then events in which one, or both, of the decay products are produced at angles that place them amongst the particles of the proton remnant are expected to become more important. In many of these events, however the two identified electron-positron candidates with the largest theta values will still originate from the decay of the J/Ψ. The decay products may start to be mis-identified, however, for wider proton remnants if high energy particles arising from the dissociation of the proton are also identified as electrons or positrons. Many of these, however, will produce hadronic clusters. The two lepton candidates with the largest theta values are therefore essentially isolated and assumed to be those that originated from the decay of the J/Ψ. If both of these objects were identified in the SPACAL region then, since no tracking information is available, the charges of the two objects are not known and it is therefore assumed that one cluster was caused by the decay positron and the other was caused by the decay electron. If one of the two largest theta objects was a SPACAL cluster and the other was identified in the tracking region then the charge of one of the objects is measured. It is then assumed that the SPACAL cluster originated from the decay product with the opposite charge of that which caused the track. If there are no SPACAL candidates then the two largest-theta objects will both lie in the tracking region. The negative track with the largest theta value and the positive track with the largest theta value are then taken to be the two decay products. More tracks will appear in events with wider

No of track candidates	No.of spacal candidates	J/ Ψ kinematics based on
0	0	No J/ Ψ candidate
	1	No J/ Ψ candidate
	2	Two spacal candidates
	>2	Two spacal candidates with the largest theta
1	0	No J/ Ψ candidate
	1	Spacal candidate and track candidate
	2	Two spacal candidates
	>2	Two spacal candidates with the largest theta
2	0	Two track candidates provided one is positive, one is negative
	1	Spacal candidate and track candidate with the largest theta
	2	Two spacal candidates
	>2	Two spacal candidates with the largest theta
>2	0	The negative track with the largest theta and the positive track with the largest theta
	1	The spacal candidate and the track with the largest theta
	2	The two spacal candidates
	>2	The two spacal candidates with the largest theta

Table 6.1: The two lepton candidates selected from those reconstructed in each event which are to be used to calculate the kinematics of the J/Ψ.

proton remnants. These events have no J/Ψ candidate if only positive or only negative tracks appear. A minimum of two electron-positron candidates must be found. The selection procedure for identifying the decay products from the list of electron-positron candidates is shown in Table 6.1.

The two most-likely decay products are used to calculate the invariant mass of the parent particle. To do this the four-vectors of the two decay products are constructed first. For decay products in the SPACAL region the measured cluster

energy (E) is converted into a total momentum measurement (P) according to

$$P^2 = E^2 - M_e^2. \tag{6.1}$$

The mass of the electron M_e actually only has a small effect since the cluster energies are typically large. The position of the centre-of-gravity of the cluster is then obtained in the H1 coordinate system and converted to give a theta and phi angle describing the position of the centre-of-gravity with respect to the true interaction point. The P_x, P_y and P_z components of the four vector are then calculated according to

$$\begin{aligned} P_x &= P \sin\theta \cos\phi \\ P_y &= P \sin\theta \sin\phi \\ P_z &= P \cos\theta. \end{aligned}$$

The P_x, P_y and P_z components of decay products identified in the tracking region are those measured via the deflection of the particle by the H1 magnetic field. These are combined to give a total momentum value (P) according to

$$P = \sqrt{((P_x)^2 + (P_y)^2 + (P_z)^2)}.$$

The total momentum is then converted into an energy measurement (E) using Equation 6.1. The energy value obtained from tracking information is expected to be more accurate than the energy of the liquid-argon cluster behind the track since the energy resolution of the calorimeter is poorer than that of the tracking detectors. The invariant mass ($M_{J/\Psi}$) of the parent particle is then obtained according to

$$M_{J/\Psi} = \sqrt{(2M_e^2 + 2(E^a E^b - P_x^a P_x^b - P_y^a P_y^b - P_z^a P_z^b))}$$

where the superscripts a and b are used to distinguish the first and second decay products.

The transverse momentum squared t of the event is to be approximated using the P_t^2 of the vector meson, as explained in section 4.2. The P_t^2 of the J/Ψ is calculated using the already constructed four-vectors of the decay products according to

$$P_t^2 = (P_x^a + P_x^b)^2 + (P_y^a + P_y^b)^2.$$

In addition the $(E - P_z)$ of the J/Ψ is also formed, since it is needed in the construction of photon elasticity z.

To ensure that t, the momentum transfer squared, can be approximated using the P_t^2 of the vector meson, the photon elasticity z must be large. The $(E-P_z)$ value of everything that was produced in the final state, excluding the scattered lepton, is calculated by looping over all the objects which appeared in the detectors. The scattered lepton is automatically excluded because the electron taggers are not considered in this loop. Care is taken to combine tracks and clusters which may have originated from a single produced object in a sensible way, so as not to double count energy and momentum values. The elasticity of the photon vertex (z) is then calculated using Equation 4.1 and required to be greater than $z = 0.8$.

If one of the electron taggers identifies a scattered lepton candidate, a good interaction vertex was found, two likely decay products may be isolated and used to calculate the quantities described and the photon elasticity is high such that the value of t may be constructed, event information is stored. Additional stored information, needed in later stages of the analysis, will be introduced as required in later sections of this chapter.

6.2 Data and Trigger Selection

The selection procedure described in the previous section is designed to select proton-elastic and proton dissociative diffractive events which may include a J/Ψ vector meson. It was run over data taken during 1997 by the H1 detector. HERA collided beams of 27.6 GeV positrons with beams of 820 GeV protons during this period. The total luminosity for data taken during this year was higher than for previous years so the number of events which were diffractive is expected, therefore, to have been higher during this data-taking period. It is expected that this will help reduce the statistical errors on the measurement of the differential cross section.

Only those data runs which were classified, for various reasons, as being of 'good' or 'medium' quality were considered. All 'bad' runs are excluded from the analysis which follows. A run may be classified as being 'bad' if, for example, certain sub-detectors were not on during the run, or not functioning as expected. All of the subdetectors which are used in this analysis have been described in chapter 5 and are required to have been under their expected high-voltage operating conditions when an event occured, before that event is stored.

Two subtriggers were chosen which would be expected to select, amongst other processes, diffractive J/Ψ events. The two subtriggers selected are expected to cover the range of possible placements within the detector of the decay products discussed earlier. The first is a track subtrigger (subtrigger s85) which demands a hit in any e-tagger and at least one negative track in the event for it to fire. The second is a SPACAL subtrigger (subtrigger s81). The subtriggers have the following definitions at H1,

s81: etag_all && (SPCLe_IET > 1 || SPCLe_IET_CEN_2)
s85: etag_all && DCRPh_TNeg.

The notation, SPCLe_IET, stands for the SPACAL Inclusive Electron Tagger. The subtrigger element SPCLe_IET considers energy deposits in the SPACAL calorimeter. The SPACAL is divided into three separate regions, an inner region close to the beam axis, a region of medium separation from the beam axis and a region of large separation from the beam axis. Different energy thresholds, which must be exceeded for the subtrigger to fire, are defined for each region. Each region has a low energy threshold, a medium energy threshold and a higher energy threshold. The notation SPCLe_IET $>$ 1 requires that at least one hit in the electromagnetic part of the calorimeter was greater than the medium energy thresholds corresponding to that region of the detector where the hit occurred. This was set at 2 GeV for the inner medium, and outer regions during 1997 running conditions. The trigger element SPCLe_IET_CEN_2 demands a hit of greater than 2 GeV in the central region of the calorimeter ($-16 < x < 8$ cm and $-8 < y < 16$ cm). The regions are shown in more detail in figure 6.1.

The efficiency of each of these subtriggers for selecting diffractive events will need to be calculated so that the number of events which were actually produced before the subtriggers selected them may be estimated. Each of the chosen triggers includes the electron-tagger trigger element. The expected efficiency of the electron-tagger trigger element will be included later with the acceptance functions of these detectors. For this reason only the efficiencies of the track and SPACAL parts of each subtrigger will need to be investigated later. So that this may be done events which fired subtrigger s80 are also stored. Subtrigger s80 has the definition

s80: etag_all.

and therefore fires if hits are obtained in any e-tagger.

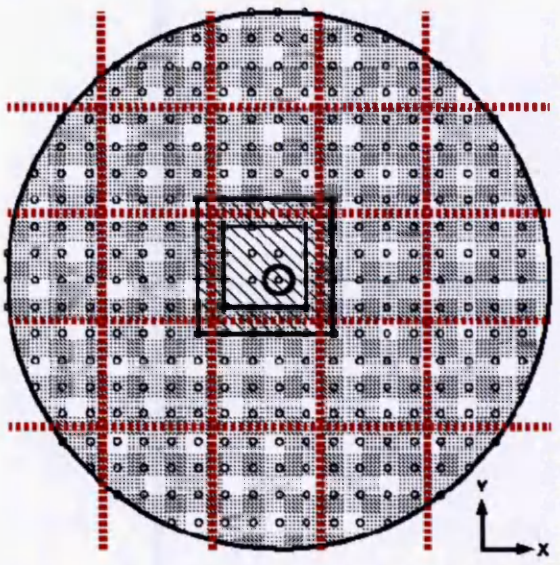

Figure 6.1: The SPACAL calorimeter is divided into several different regions with different trigger settings. The hashed region in the centre represents the region covered by the central card. The square shaded regions are covered by IET $> 1, 2$. The red lines represents the card limits. Cluster bits are represented by open circles.

During 1997 approximately 37 million events were collected. Some of these were collected by a minimum-bias run for which the trigger settings were altered. This run makes up only a small fraction of the year's data. It is neglected since alternative triggers would then have to be chosen for a small part of the sample, leading to a result which arises partly from one choice of triggers and partly from another. To reduce the number of events which the selection must consider, and to reduce the size of the output files to a manageable size, only those events which are stored in the J/Ψ event class were considered. An event stored in this class has already been identified as having either

1. greater than or equal to two 'electrons',
2. greater than or equal to one 'electron' and less than or equal to five tracks,
3. or greater than or equal to one 'electron' with a tranverse momentum greater than 1 GeV,

or some combination of these.

In the central region an electron is defined as having at least ten hits in the CJC and a track start radius within 30cm of the vertex. In the forward region an electron tracks are identified as having a track fit with a chi-squared value less than 10, a chi-squared vertex fit less than 20, a total track momentum greater than 1 GeV, and an R_0 fit less than 5 which fired greater than one module. The process of classifying an event occurs at the fourth level of the trigger system. To reach the fourth level trigger elements must have fired at the first level. The triggers applicable to this event class include the track and SPACAL trigger elements described previously.

6.3 Subtraction of DIS and Beam-Background Interactions

The selected events were first investigated to verify that the various measured quantities were behaving as expected. One region where this appeared not to be the case was in the measured $(E - P_z)$ of the final state, where the scattered positron is also included. The $(E - P_z)$ of the final state is expected to equal the $(E - P_z)$ of the initial state due to energy and momentum conservation. Since its initial value is twice the incoming positron energy, the total $(E - P_z)$ of the final state, including the scattered positron, is expected to equal 55.2 GeV. The experimentally measured distributions for events selected by the e-tagger at z=-33.4 metres and by the e-tagger at z=-44.0 metres are shown separately in figure 6.2. The e-tagger33 selected events show a good peak centred at about $(E - P_z) = 55.2$ GeV as expected. The e-tagger44 selected events, however, do not show this expected form.

To see if the poorer resolution of this electron-tagger was responsible the expected values of Bjorken y for these events were considered. Bjorken y may be reconstructed from the final state of the event, where the scattered positron is excluded, according to the method of Jacquet-Blondel;

$$y = \frac{(E - P_z)_{\text{Final State}}}{2E_e}.$$

The $(E - P_z)$ of the final state is obtained by the selection code since it is used in the determination of the photon elasticity z. Since the e-tagger at z=-44.0 metres

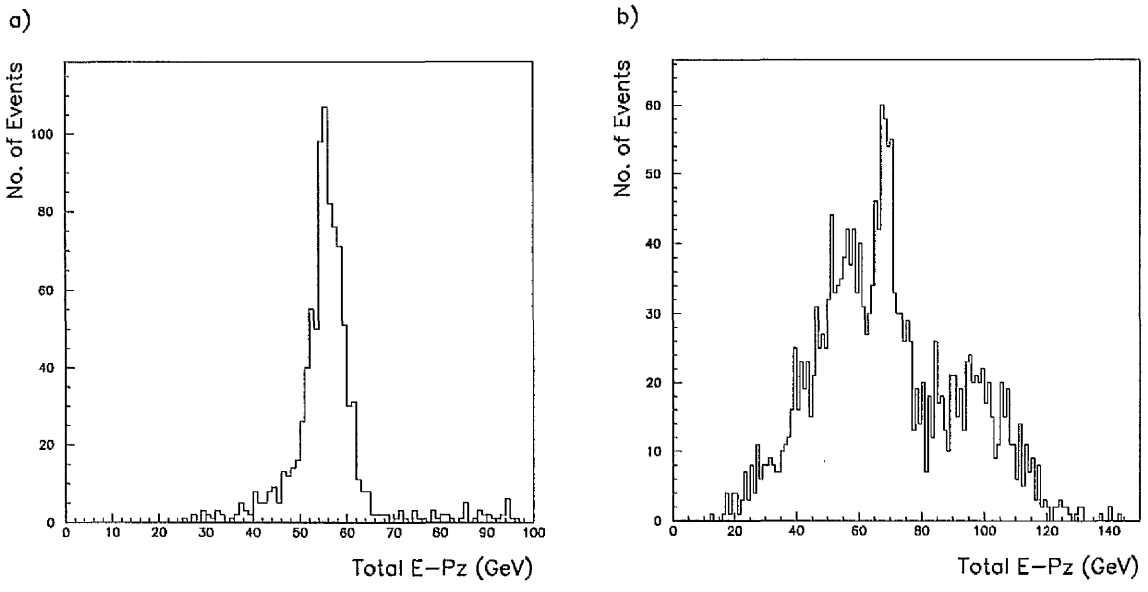

Figure 6.2: The $(E - P_z)$ of the final state, including the scattered positron, for events selected by a) e-tagger33 and b) e-tagger44.

covers the range $0.04 < y < 0.24$, the $(E - P_z)$ of the event, excluding the scattered positron, is expected to lie in the range $2.208 < (E - P_z) < 13.248$ GeV. The $(E - P_z)$ distribution of these events is shown in figure 6.3. A second peak appears at values above the expected range of this variable.

The second peak is positioned at $(E - P_z) \sim 55.2$ GeV and suggests that the entire final state, including the scattered positron, was produced in the main part of the detectors. This is expected if the virtuality of the photon was large, placing the scattered positron in the main part of the detector. To see if this was indeed the case the energy distributions of the 'decay' electrons were investigated. The energy distribution of the first 'decay' products found in the SPACAL region in each event is shown in figure 6.4. The peak at high energies does indeed suggest that the high energy scattered positron has entered the main part of the detector.

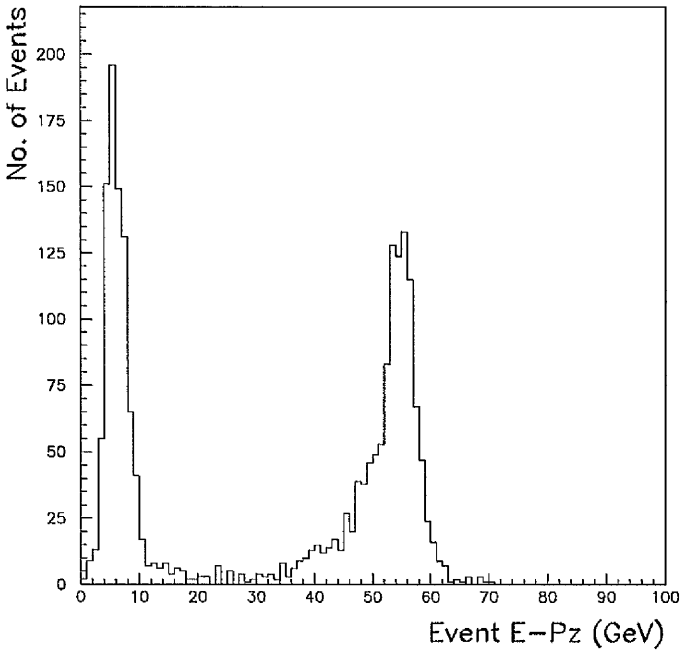

Figure 6.3: The $(E - P_z)$ of the final state, excluding the scattered positron, for events selected by e-tagger44.

It is most probable that a beam-gas interaction or an interaction of the beam with the walls of the beam pipe placed an unrelated object in the e-tagger such that the event entered the selected sample. The energy distribution of the 'scattered positrons' which entered e-tagger44 is also shown in figure 6.4. The expected scattered positron energy is about 22 GeV. This follows because Bjorken y may also be calculated from the energy deposit (E') in the tagger according to

$$y = 1 - \frac{E'}{E_e}.$$

The range in y covered by e-tagger44 gives a typical energy deposit of this value. A peak appears as this energy, however, it sits on top of a background which falls as

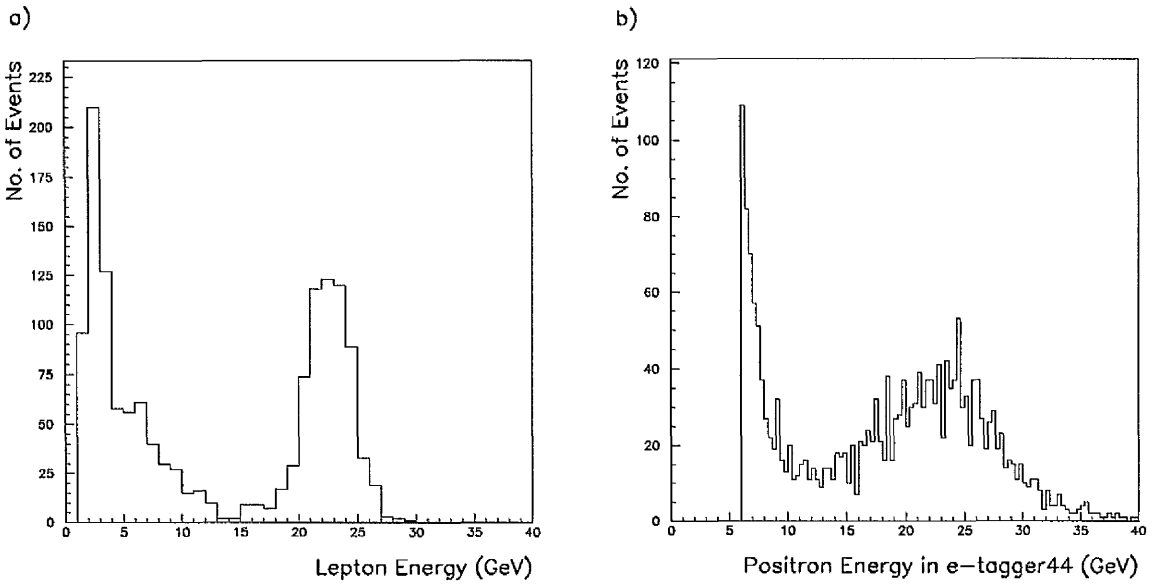

Figure 6.4: The energy distribution of a) the largest theta decay lepton identified in the SPACAL region and b) the energy of the scattered positron in e-tagger44.

energy increases. The cutoff at 6 GeV arises from the restriction in the selection code. This background probably arises from predominantly low-energy objects entering the tagger from background interactions.

The unwanted contributions to these graphs are removed by restricting the measured value of Bjorken y to be essentially within its expected range. Only those events selected by e-tagger44 which lead to y values in the range $0.0395 < y < 0.245$ are kept. The reason for allowing events with values of y slightly lower and slightly higher than the nominal range of the e-tagger is to allow for the resolution in this variable. This will be discussed later. The value of y measured using the method of Jacquet-Blondel is used when making this restriction.

6.4 Separation of Elastic and Inelastic Events.

The differential cross section in Mandelstam t is to be measured for proton dissociative diffraction. Events in which the proton remained intact must therefore be identified and removed from the selected sample. To do this information on the number of tracks and clusters that were produced in each event was also obtained by the selection code.

It has already been mentioned that in a proton-elastic event only the two decay products of the J/Ψ are expected to appear in the main part of the detector. Events in which only two electron-positron candidates were found are therefore now identified in the selected sample and investigated to see if only tracks corresponding to decay products were produced. If this is the case then the only charged particles which were produced in the tracking region are expected to be decay products and, since the total number of decay products is now equal to two, this places a restriction on the number of electromagnetic clusters which appeared in the SPACAL region. The total number of clusters which were used in the calculation of the $(E - P_z)$ of the final state is required to be less than three. In the calculation of the $(E - P_z)$ of the final state care is taken to match clusters and tracks produced by the same object in a careful way. Sometimes the cluster will not be used in the calculation of $(E - P_z)$, and the track will be used instead. This occurs if it is felt that a better energy or momentum measurement will be obtained by the track. For this reason the number of clusters used may be zero, but is not expected to be greater than two in a proton elastic event. Clusters which most likely arose from random noise in the calorimeters are not included in this list.

This essentially isolates events in which the proton probably remained intact. Inelastic events, however, in which the produced proton remnant jet is narrow enough to be contained inside the beam pipe still remain in this sample. Some of these events may be removed, since secondary scattering caused by interactions between the proton remnant and the wall of the beam pipe, or with the material of the collimators, sometimes appears in the forward detectors. Proton elastic events are therefore also required to show 'no activity' in the forward region. The selection code flags an event as having 'no forward activity' if the energy in the first six layers of the PLUG calorimeter is less than 3.0 GeV, there are no forward muon pairs in the first three layers of the forward muon detector and there are no hits in the first

three scintillators of the proton remnant tagger. Events which meet the track and cluster conditions and have been flagged are then assumed to be elastic and every other event is assumed to then be inelastic. Inelastic events with proton remnants of mass greater than about 1.6 $GeVc^{-2}$ are selected by this method.

6.5 The Monte Carlo Event Generator HITVM.

Two Monte Carlo generators HITVM and RHODI have been written to describe the diffractive production of vector mesons at large t. Both of these generators describe proton dissociative interactions and are based on the QCD description of the pomeron. The main difference between the two is the way in which they model the proton remnant. In HITVM, the parton which is struck inside the proton can be either a valence quark, gluon or sea quark and the proton remnant is then either a di-quark, quark or quark-baryon combination respectively. This is based on the method used by the PYTHIA event generator and in each case the resulting particles are passed to the JETSET package to hadronize. The modelling of the proton remnant in RHODI is based on results from the UA5 experiment [49].

The monte carlo event generator HITVM is used here. It incorporates the calculations discussed in chapter 4 with a input value of $\bar{\alpha}_s = 0.2$. The angular decay distribution of the J/Ψ decay products is taken according to s-channel helicity conservation. The produced vector meson then has the same helicity, or polarisation, as the photon. Since the decay products of the J/Ψ are also expected to be able to radiate photons before reaching the detectors the brehmstrahlung process is also included in the event generation.

Each event produced by the event generator was subjected to a simulation of the H1 detector response. The behaviour of the electron taggers, however, was not included in this detector simulation. The electron taggers will not detect the scattered lepton every time that it enters them. The number of scattered leptons that are detected by the taggers may be described by acceptance functions. The acceptance functions for the electron tagger at z=-44.0 metres and the electron tagger at z=-33.4 metres are shown in figure 6.5. The ability of the taggers to detect the scattered lepton varies as a function of Bjorken y. Each of the events generated are therefore weighted so that the number of events reconstructed by the

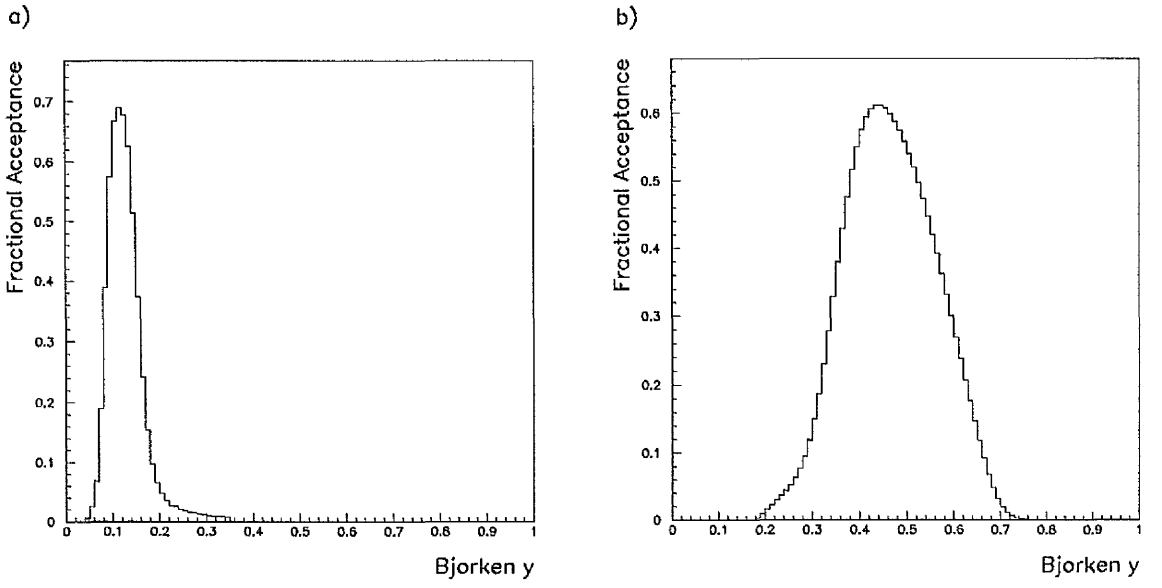

Figure 6.5: The acceptance functions, as a function of Bjorken y, for a) e-tagger44 and b) e-tagger33.

detectors is corrected for the number of scattered leptons that are expected to be reconstructed by the electron taggers.

For the purposes of this analysis the electron taggers are only used to identify photoproduction events. The energy deposits in the taggers are not used in the reconstruction of any quantity. The energy resolution of e-tagger44 does not allow a measurement of the energy deposited there in any case. For this reason the energy deposits are not smeared to account for the resolution of these detectors. The energy deposit would be smeared after it had been decided if the scattered lepton would be reconstructed or not, and becomes necessary if the energy deposits are then used in some way.

6.5.1 Resolution in Bjorken y

As discussed previously the resolution in Bjorken y was used to determine the range in which events selected by the e-tagger at z=-44.0 metres would be

restricted, to avoid a contribution from a DIS and beam-gas background. The value of Bjorken y in such an event is reconstructed according to the method of Jacquet-Blondel, and compared to the true generated value in figure 6.6. The full width at half maximum is 0.01. The resolution in Bjorken y represents the typical separation of the true and reconstructed values and may be calculated by dividing the full width at half maximum by 2.35. The resolution is good. Events in which a scattered lepton candidate appeared in e-tagger44 were restricted to have a y value in the range $0.0395 < y < 0.245$. This is because events produced at the edges of the nominal y-range of this tagger may be measured at values which are separated by typically about 0.005 above or below the nominal values. The wider y range is used to account for this effect. Events which have measured y values lying outside of this range are most probably not photoproduction events.

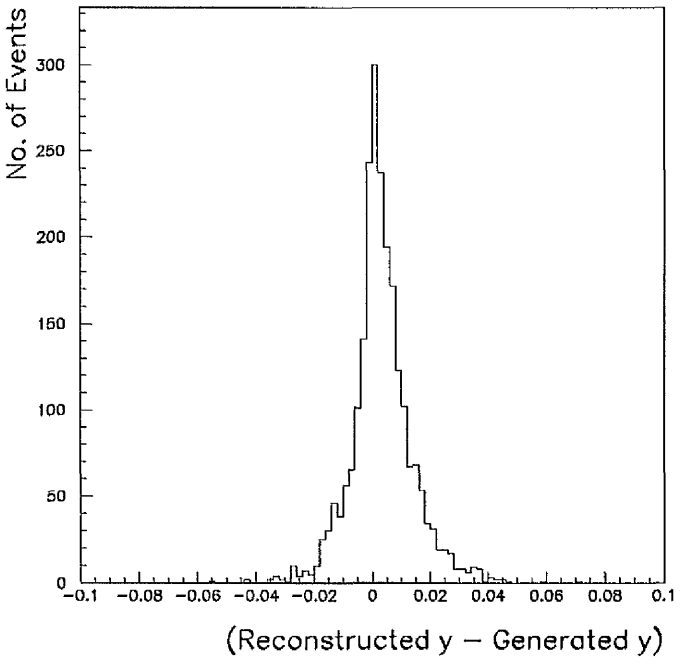

Figure 6.6: The separation of the reconstructed and generated values of Bjorken y for events selected by e-tagger44. The reconstructed values are obtained according to the method of Jacquet-Blondel.

6.5.2 Resolution in Mandelstam t.

In the selected kinematic region the momentum transfer squared t may be approximated by the transverse momentum squared of the J/Ψ. The reconstructed values of t are compared to their generated values in figure 6.7. The full width at half maximum for events selected by e-tagger44 is 0.36 GeV^2c^{-2}. Similarly the full width at half maximum for events selected by e-tagger33 is 0.6 GeV^2c^{-2}. The resolutions in t for e-tagger33 and e-tagger44 selected events may be obtained by dividing the full widths at half height by 2.35.

The range $|t| = 1-10$ GeV^2c^{-2} in which the differential cross section $d\sigma/dt$ is to be investigated is now divided into nine equally spaced bins, each 1 GeV^2c^{-2} wide. These bin widths must be at least as wide as the full widths at half maximum to ensure that the majority of events produced at the central value in each t-bin are captured in that bin. To make it easy to compare the two final differential cross sections the same bin widths are chosen in both centre-of-mass energy ranges.

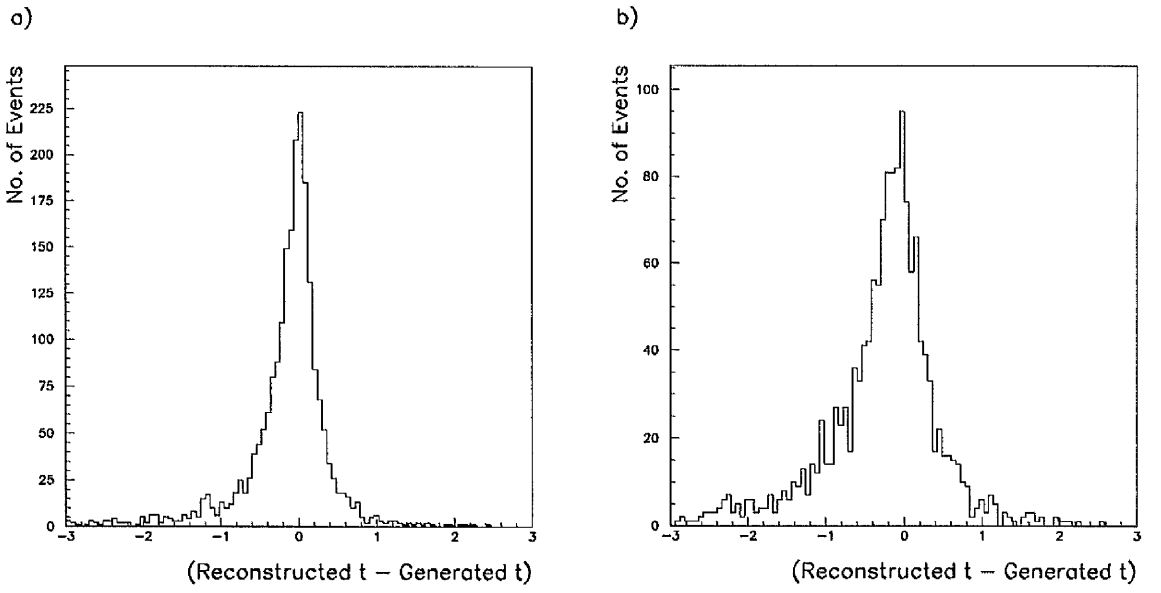

Figure 6.7: The separation of the reconstructed and generated values of t in GeV^2c^{-2} for events selected by a) e-tagger44 and b) e-tagger33.

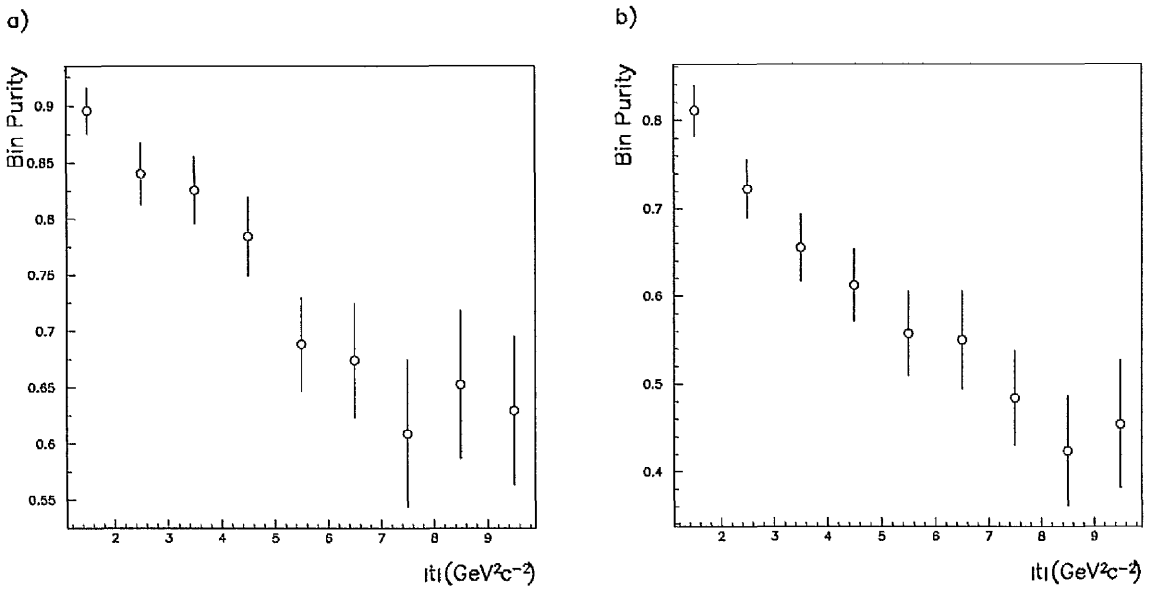

Figure 6.8: The purities of the chosen t-bins for events selected by a) e-tagger44 and b) e-tagger33 as a function of |t|.

To see if the t-resolution varies with t the purity of each bin is calculated. The purity (p) of a bin is obtained according to

$$p = \frac{N_{GR}}{N_R}$$

where N_{GR} is the number of events reconstructed in a bin that were also generated with t values in that bin, and N_R is the total number of events reconstructed in that bin, regardless of whether they were generated there or not. The bin purities for events selected in both centre-of-mass energy ranges are shown in figure 6.8.

It is now clear that the resolution in t, not only becomes worse with increasing values of the photon-proton centre of mass energy, but also worsens with increasing t. This follows because the bin purities fall as t is increased, the number of events reconstructed with larger separations from their generated values than the typical separation, becoming more significant. As the centre-of-mass energy is increased it is expected that the decay products will become more likely to emit photons in the final state. Since the photon is expected to be emitted predominantly co-linear with the decay product, the clusters created by the decay products

should also include the energies of the emitted photons. In the tracking region the four-vectors of the decay products are calculated using tracking information. Neutral photons will not be included in the measurements of the P_x and P_y components of the four-vector. The four-vectors of decay products identified in the SPACAL region are calculated using the SPACAL cluster and should include the photon. If one, or both, of the decay products appear in the tracking region and photons are emitted it will lead to an underestimate of the value of t. This is clear from the higher tail on the left-hand side of the resolution plot in figure 6.7. The smearing effect in the t-distribution will be considered in section 6.10.

6.5.3 Mass Distribution as a Function of t

To remove those sources of background that remain in the proton dissociative diffraction sample, and to obtain the number of diffractive events produced in each bin of t, the J/Ψ mass peak is to be identified above a distribution which arises from background processes. The reconstructed mass distributions in each bin of t for events selected by the electron tagger at z=-44.0 metres are shown in figure 6.9. The mass distribution has a similar form in each bin of t. The position of the maximum appears at about 3.1 $GeVc^{-2}$ and a radiative tail, which arises when events in which decay products which have radiated photons and are identified in the tracking region are used to calculate the invariant mass, appears on the left-hand side. A function that describes the shape well is

$$f(m) = \begin{cases} A\exp\left(-\frac{|\bar{m}-m|}{a}\right) & m < \overline{m} \\ A\exp\left(-\frac{(m-\bar{m})^2}{2\sigma^2}\right) & m > \overline{m} \end{cases}$$

where $\bar{m}$ is the position of the peak of the mass distribution. The constant which pre-multiplies the function in each region is chosen to be equal to A in both regions, so that the function joins smoothly at the intersection of the two different regions. It is fitted to the first four bins in this centre-of-mass energy range.

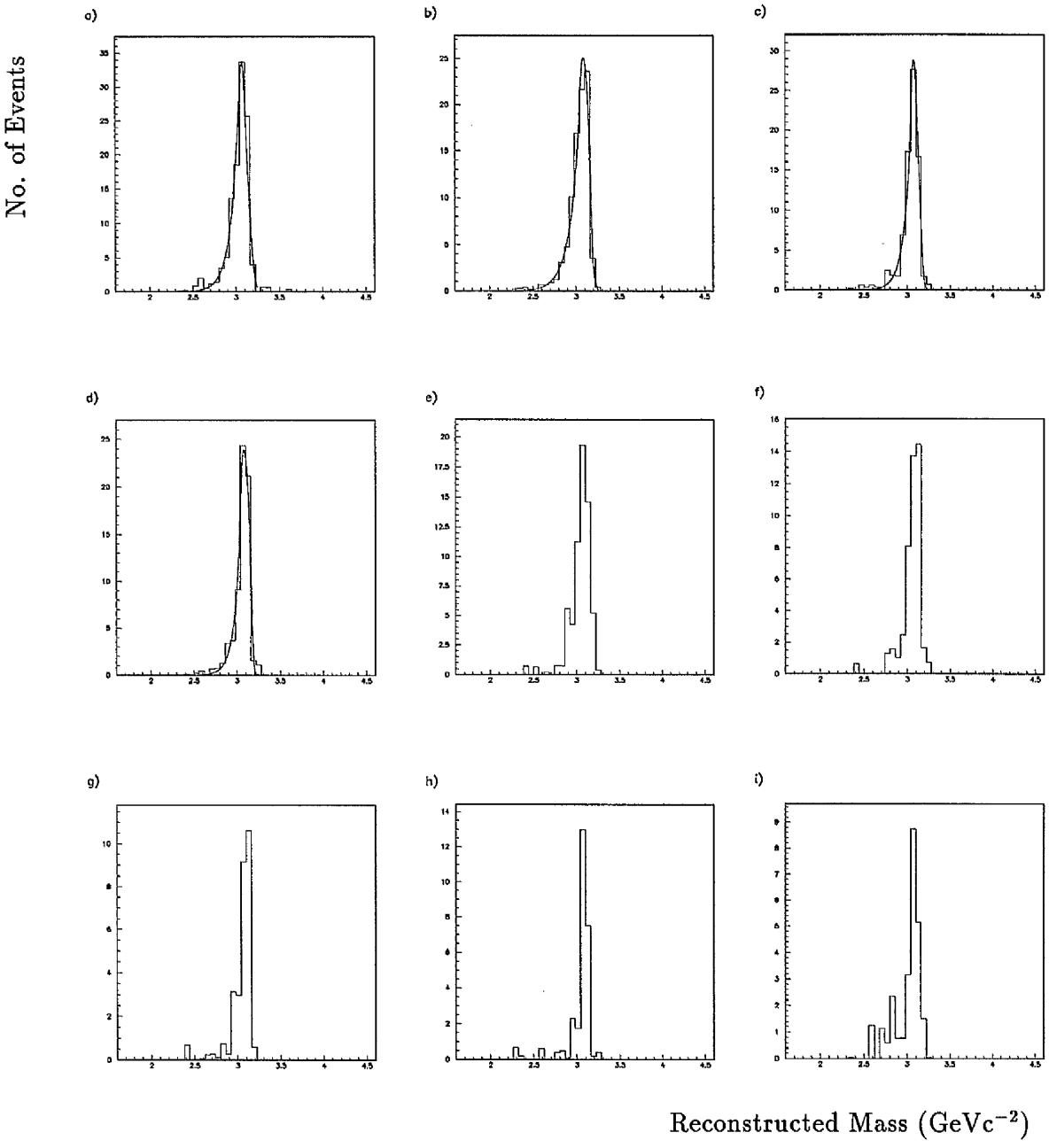

Figure 6.9: The reconstructed mass distributions for events generated in the e-tagger44 centre-of-mass energy range. Bin a) covers the range $1.0 < |t| < 2.0$ GeV^{2}c^{-2}, b) the range $2.0 < |t| < 3.0$ GeV^{2}c^{-2} and so on. The results of the functional fit to the first four bins are shown.

The area under the function, found by integrating the function from minus infinity to plus infinity (the functions only tend to zero but never actually reach zero), is equal to the number of events in the peak (N) multiplied by the bin width (w) used to plot the distribution

$$\mathrm{Nw} = \mathrm{A}\left(\mathrm{a} + \sqrt{\frac{\pi}{2}}\sigma\right).$$

The result does not depend on the mean mass, therefore it is possible to vary this to achieve the best fit. This is because both of the functions fitted are even functions about $\mathrm{m} = \bar{\mathrm{m}}$. The total statistical error is then given by the summing the errors in the parameters A, a and σ in quadrature according to

$$\sigma^2(\mathrm{N}) = \left(\frac{\partial \mathrm{N}}{\partial \mathrm{A}}\right)^2 \sigma^2(\mathrm{A}) + \left(\frac{\partial \mathrm{N}}{\partial \mathrm{a}}\right)^2 \sigma^2(\mathrm{a}) + \left(\frac{\partial \mathrm{N}}{\partial \sigma}\right)^2 \sigma^2(\sigma)$$

Parameters a and σ, and their errors, may be fixed by the fits to the reconstructed mass distributions. The values of these parameters together with their associated uncertainties are presented in Table 6.2. The reconstructed mass distributions in each bin of t for events selected by e-tagger33 are shown in figure 6.10. Once again the shape of the mass peak is similar in each bin of t. The same function is chosen to describe the shape of the mass plot. It is fitted to the mass distributions of the first four t-bins. The best values of the parameters a and σ, together with their associated uncertainties, are also presented in Table 6.2.

Events Selected By	Bin Number	σ	Constant a
E-tagger44	1	0.052 ± 0.005	0.11 ± 0.01
	2	0.044 ± 0.006	0.12 ± 0.01
	3	0.023 ± 0.003	0.08 ± 0.01
	4	0.067 ± 0.006	0.06 ± 0.01
E-tagger33	1	0.050 ± 0.004	0.11 ± 0.01
	2	0.072 ± 0.008	0.14 ± 0.02
	3	0.067 ± 0.009	0.15 ± 0.02
	4	0.050 ± 0.002	0.109 ± 0.003

Table 6.2: The values of the a and σ parameters, together with their associated uncertainties, obtained from a least squares fit to the reconstructed mass peak in the first four bins of each centre-of-mass energy range.

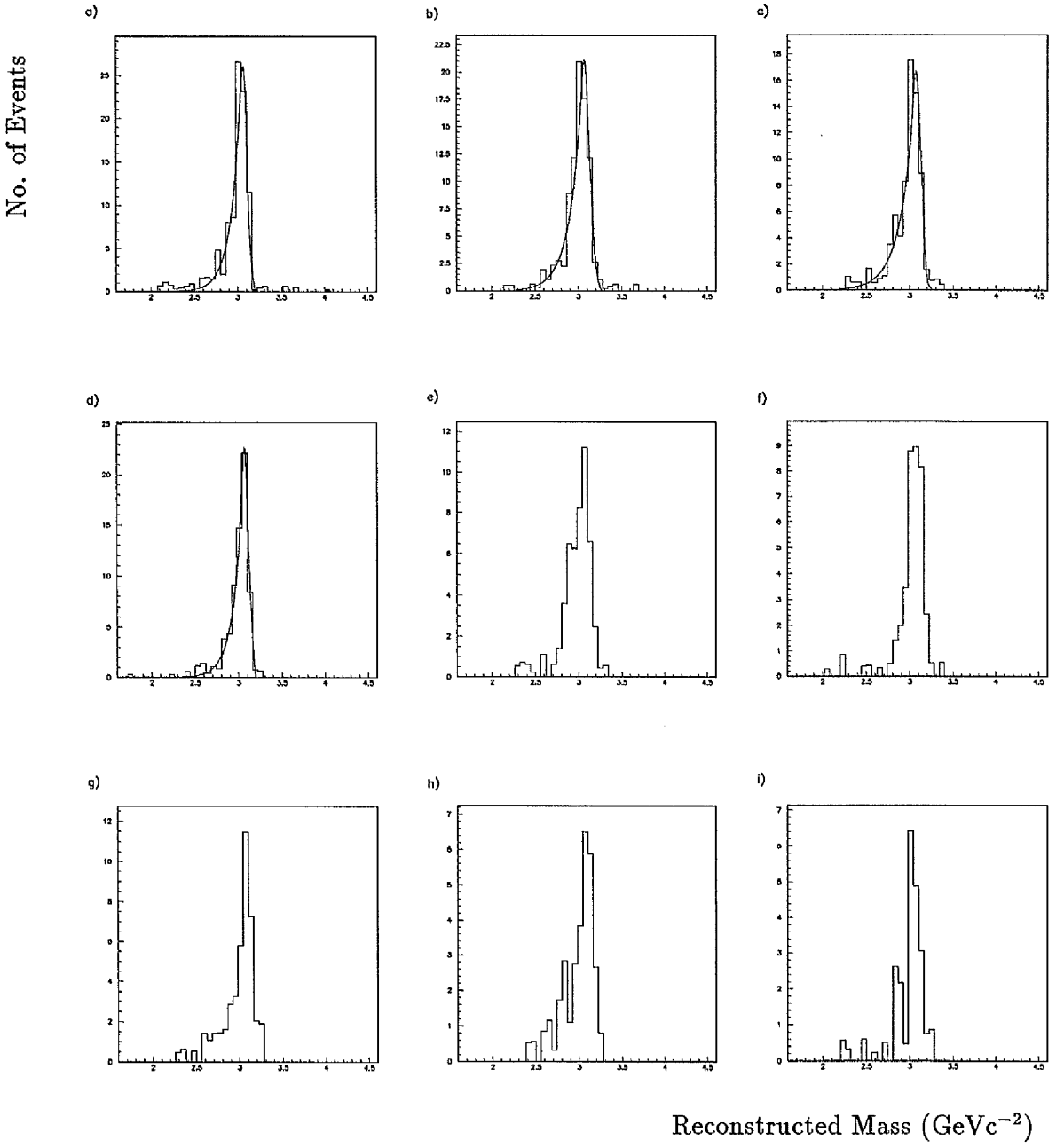

Figure 6.10: The reconstructed mass distributions for events generated in the e-tagger33 centre-of-mass energy range. Bin a) covers the range $1.0 < |t| < 2.0$ GeV^{2}c^{-2}, b) the range $2.0 < |t| < 3.0$ GeV^{2}c^{-2} and so on. The results of the functional fit to the first four bins are shown.

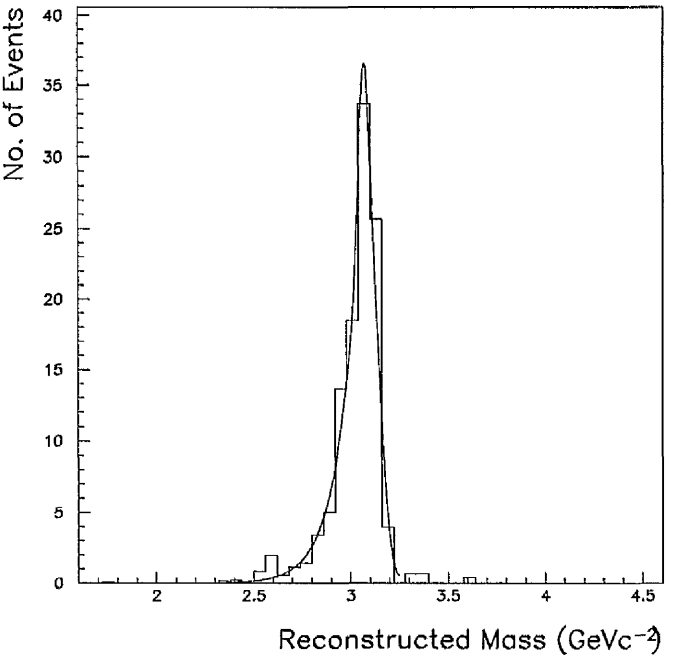

Figure 6.11: The result of the normalised functional fit to the $1.0 < |t| < 2.0$ GeV^2c^{-2} bin for events selected by e-tagger44.

Correlations between the a and sigma parameters have been neglected in performing these functional fits. This is justified since if one normalises the function and performs the fit with the normalised function no difference appears in the result. The fit of the normalised function to the first bin in the e-tagger44 centre-of-mass energy range is shown in fig. 6.11. Here the function has been normalised such that the area under the function fitted above the position of the peak $\bar{m}$ and the area under the function below the position of the peak both equal a half. The number of events reconstructed above and below the peak are now given entirely by the factors which premultiply the functions in the two regions. Since the number of events reconstructed above the peak may not be equaivalent to the number reconstructed below different factors are chosen in the two regions. The best estimate of the a parameter is 0.1 ± 0.02 and the best estimate of the sigma parameter is 0.068 ± 0.007.

6.6 Sources of Background.

6.6.1 Production of Higher Mass Charmonium States

It has already been mentioned that any vector meson may be produced at the photon vertex of the diffractive process, although the calculation is expected to be most valid for heavier vector mesons. The reconstructed mass distribution in Monte Carlo shows sensible properties and peaks at the expected J/Ψ mass. When the selection code was run over data, however, it is possible that it may have also selected diffractive events in which other vector meson states were produced. Of particular concern is the production of other states which belong to the charmonium system, since these have masses close to the J/Ψ mass. Many of these states are also able to decay down to the J/Ψ state and the code may sometimes therefore select the correct vector meson when it was not the object produced at the photon vertex. Some events in which this occured will not be selected if the $(E - P_z)$ of the identified J/Ψ leads to a photon elasticity value below 0.8.

The states of concern are the $\Psi(2S)$, or Ψ', state and the χ-states. The Ψ', which has a mass of about 3.7 $GeVc^{-2}$, may decay directly into an electron-positron pair or alternatively to give a J/Ψ and electron-positron pair. The direct process has a branching ratio of $(8.5 \pm 0.7) \times 10^{-3}$ and the second has a higher branching ratio of $(10.0 \pm 3.3) \times 10^{-3}$. The χ-states decay directly to the J/Ψ according to

$$\chi \rightarrow \gamma J/\Psi$$

There are three χ-states each with masses of approximately 3.42, 3.51 and 3.56 $GeVc^{-2}$. Peaks corresponding to higher mass charmonium states may therefore appear close to the J/Ψ peak.

6.6.2 Electromagnetic Production of Leptonic Pairs.

The incoming positron and the incoming proton may both emit photons which then interact leading to an electron-positron pair in the final state. The Feynman diagram representing this process is shown in figure 6.12. The proton may dissociate or remain intact. The essential feature of the cross section for this process

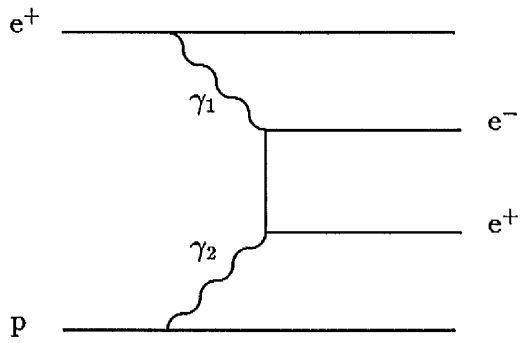

Figure 6.12: The Feynman diagram for the electromagnetic production of lepton pairs via two photons. The electron may also be produced at the lower vertex. The proton may also dissociate.

is that it is peaked at low values of momentum transfer squared. Nevertheless, at values of t in the range considered here the selection code may locate electrons and positrons in the final state which arose from this process, and form an invariant mass from these particles. The background arising from this process is expected to decrease for higher values of t.

To investigate how events which arose from two-photon processes will be reconstructed the event generator LPAIR was used [50]. Its generated differential cross section behaves essentially as $t_1^{-1}t_2^{-1}$ where t_1 represents the squared four-vector of photon 1 and t_2 represents the squared four-vector of photon 2. The reconstructed t distributions for events selected by e-tagger44 and by e-tagger33 are shown in figure 6.13. The reconstructed t-distributions do indeed peak at low t, and fall-off as t is increased. Fewer events are expected in the higher centre-of-mass energy range and the fall-off is also slightly sharper here. The reconstructed mass distributions for both centre-of-mass energy ranges are shown in figure 6.14. These both rise to a peak at a mass of about 2.2 $GeVc^{-2}$ then fall-off as the mass is increased above this value. The fall-off is again sharper in the e-tagger33 centre-of-mass energy range.

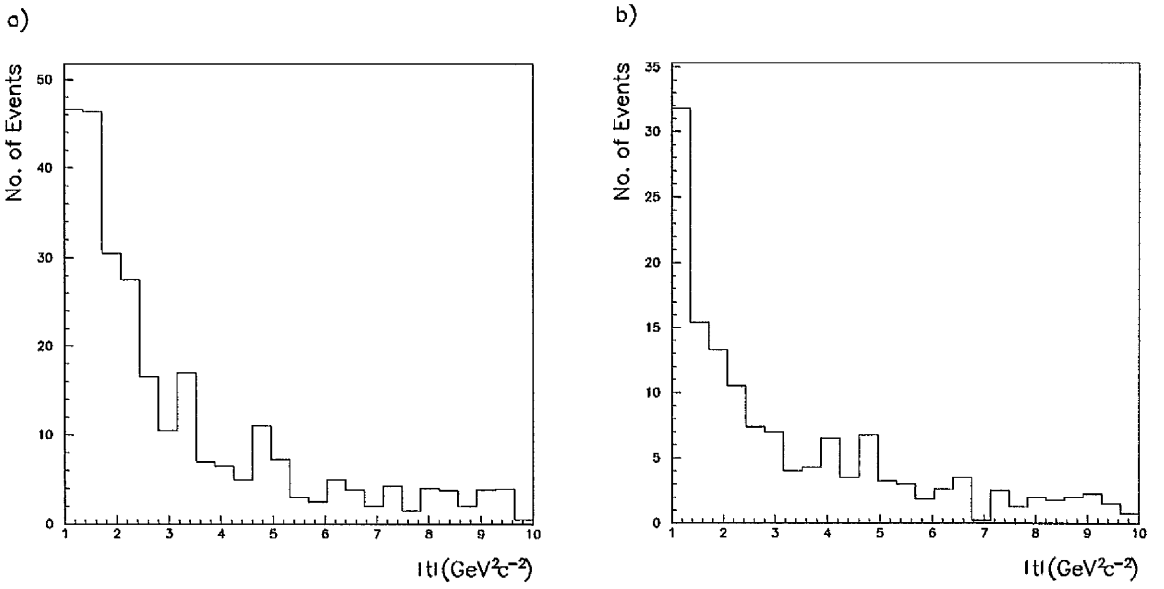

Figure 6.13: The reconstructed |t|-distributions for lepton pair production in a) the e-tagger44 and b) the e-tagger33 centre-of-mass energy ranges.

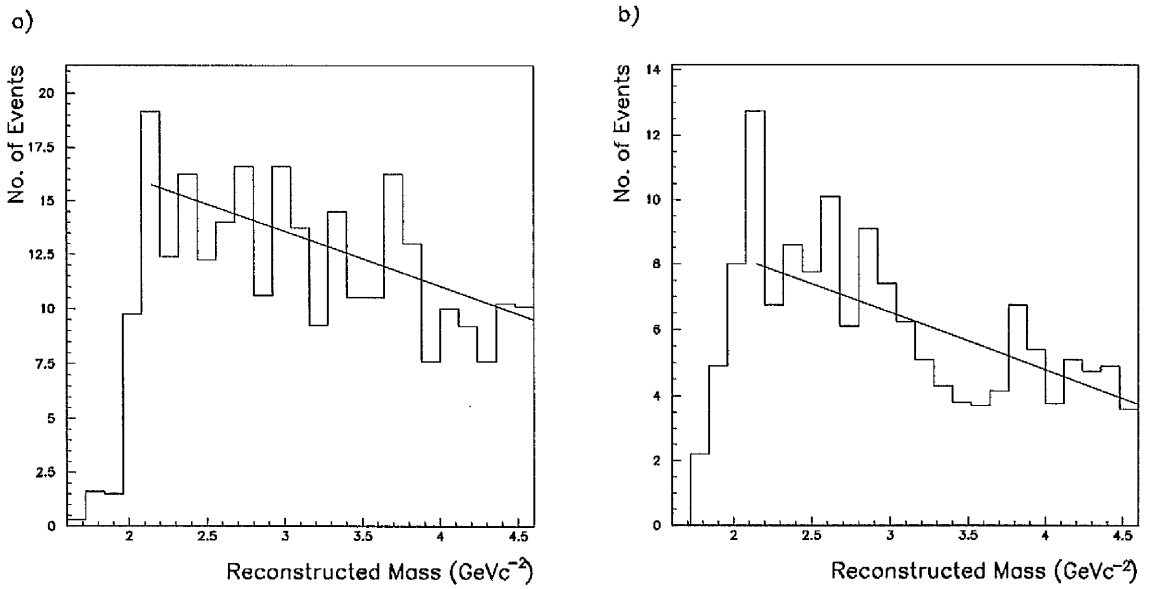

Figure 6.14: The reconstructed mass distributions for lepton pair production in a) the e-tagger44 and b) the e-tagger33 centre-of-mass energy ranges.

6.7 Background Subtraction in Data.

The reconstructed mass distributions in each bin of t for events selected from data by e-tagger44 are shown in figure 6.15. These were selected using the track subtrigger s85. As expected from the cross section predictions the statistics are low, particularly in the higher t-bins. In the first t-bin a peak at the expected J/Ψ mass appears which sits on a background which appears to be high at a mass of about 2.2 $GeVc^{-2}$. The background appears to originate from the production of lepton pairs via the two-photon process. Two smaller peaks appear above the J/Ψ mass, which may well correspond to the production of higher mass charmonium states. The number of events in the J/Ψ peak is identified using the function chosen in section 6.5.3. A falling straight-line dependence is chosen to describe the background in the mass region greater than 2.2 $GeVc^{-2}$. The parameters of the peak function a and σ were fixed using the higher statistics of the monte carlo event generator. The value of the parameter A that was obtained, together with its associated uncertainty, is shown in Table 6.3. The number of events may be calculated, together with the total statistical error which includes the additional uncertainty in fitting the function, according to the method described. The results are also shown in Table 6.3.

Bin Number	Constant A	chi-squared	No. of Events (N)
1	18 ± 4	0.5528	26 ± 6
2	10 ± 3	0.7182	14 ± 4
3	12 ± 4	3.580	11 ± 4
4	8 ± 3	4.258	10 ± 3
5	-	-	7 ± 3
6	-	-	6 ± 2
7	-	-	4 ± 2
8	-	-	2 ± 1
9	-	-	2 ± 1

Table 6.3: The number of events selected in each bin of |t| for the e-tagger44 centre-of-mass energy range .

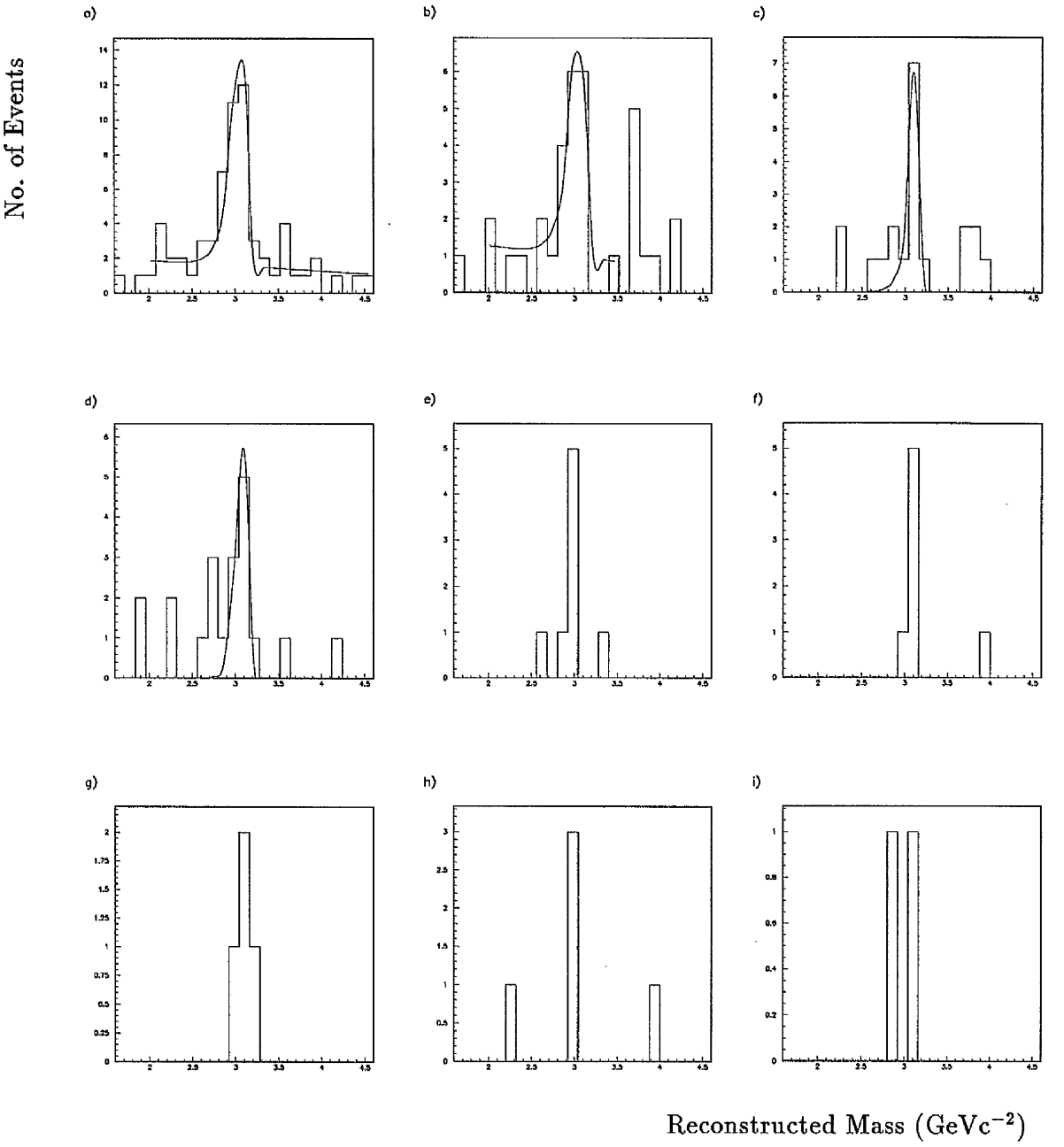

Figure 6.15: The reconstructed mass distributions in bins of t for events selected in the e-tagger44 centre-of-mass energy range. Bin a) covers the range $1.0 < |t| < 2.0$ GeV^{2}c^{-2}, b) the range $2.0 < |t| < 3.0$ GeV^{2}c^{-2} and so on. The results of the functional fit to the first four bins are shown.

In the second t-bin the background arising from lepton pair production has fallen off as expected. The height of a second peak, above the J/Ψ peak, most probably arising from Ψ'-production, is now comparable to the height of the J/Ψ peak. It was chosen once again to fit the leptonic pair background with a straight line dependence. The mass region where the higher mass peak appears is avoided, however, so as not to overestimate the height of the leptonic pair background. The a and σ parameters are once again fixed using the higher monte carlo statistics. The number of events obtained, together with the associated statistical error, are also shown in Table 6.3.

In bins three and four the background from lepton-pair production appears to have almost disappeared. Sporadic events might be expected however in these bins, sometimes perhaps appearing under the J/Ψ peak. The peak is therefore, once again, identified using the function of section 6.5.3, and the a and σ parameters are once again fixed using the higher monte carlo statistics. A function is not used to describe leptonic pair background in these two bins. For the remaining t-bins it becomes more sensible to count the events. This is done using a mass window of $2.44 < m < 3.16$ GeVc^{-2}.

The reconstructed mass distributions in each bin of t for events selected from data by e-tagger33 are shown in figure 6.16. These were selected by both the track subtrigger s85 and the SPACAL subtrigger s81. These may be interpreted in a similar way to those distributions in the e-tagger44 centre-of-mass energy range. In the first bin a straight line dependence is chosen once again to describe the background at masses above 2.2 GeVc^{-2}. The t-distribution of leptonic pair events is expected to fall-off more rapidly in this centre-of-mass energy range. This background appears to have already reduced to the production of sporadic lepton-pair events by the second bin. A background function is therefore not used in this bin. The a and σ parameters are once again fixed using the higher monte carlo statistics in bins 1 and 2. The result of the fit and the number of events obtained, together with their associated uncertainties are shown in Table 6.4. A peak is identified in bins three and four, also in case sporadic events appear in the peak region.

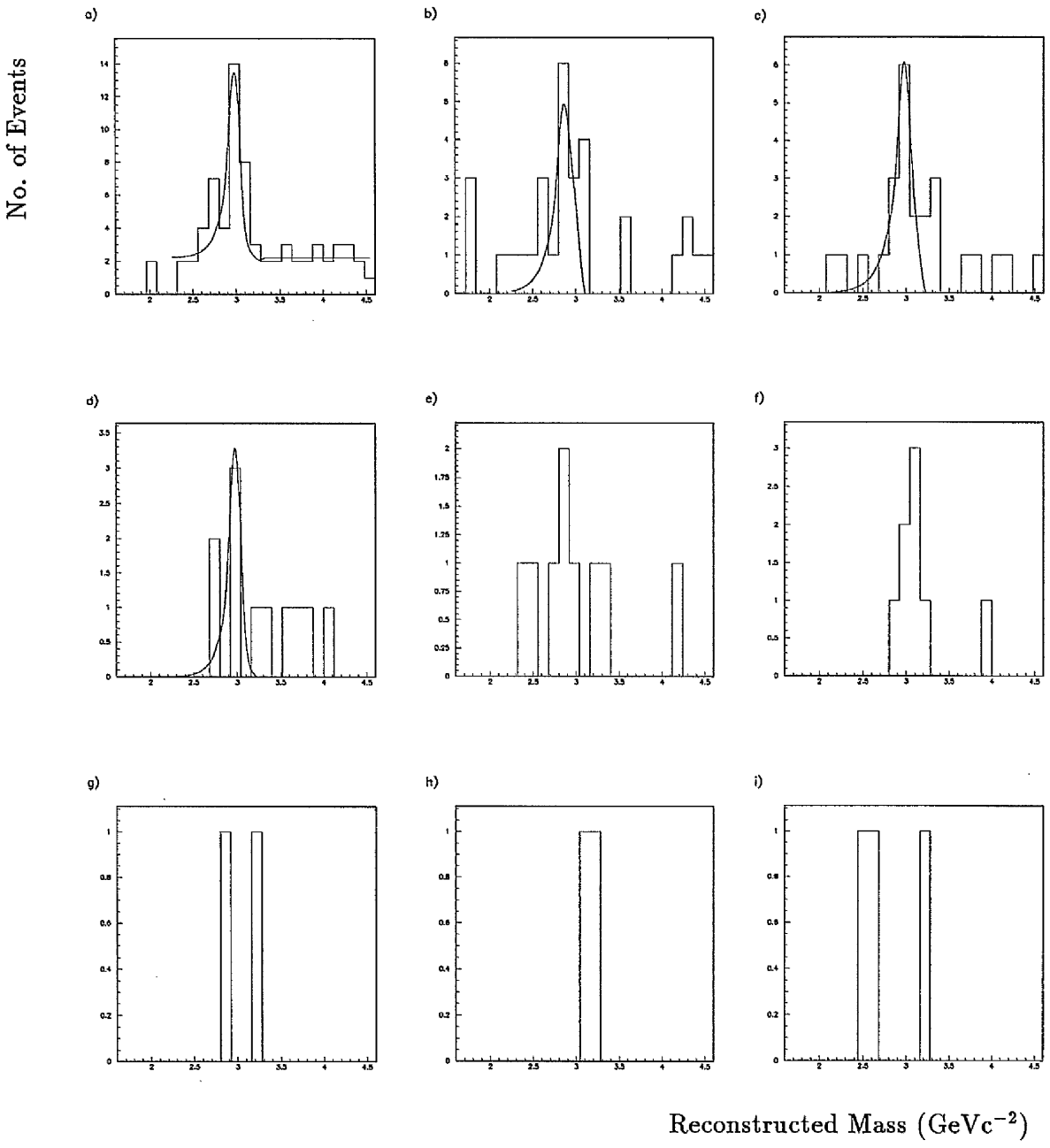

Figure 6.16: The reconstructed mass distributions in bins of t for events selected in the e-tagger33 centre-of-mass energy range. Bin a) covers the range $1.0 < |t| < 2.0$ GeV^{2}c^{-2}, b) the range $2.0 < |t| < 3.0$ GeV^{2}c^{-2} and so on. The results of the functional fit to the first four bins are shown.

Bin Number	Constant A	Chi-Squared	No. of Events(N)
1	13 ± 4	0.6727	19 ± 6
2	6 ± 2	2.398	12 ± 4
3	7 ± 2	1.792	13 ± 4
4	4 ± 2	7.369	6 ± 3
5	-	-	5 ± 2
6	-	-	7 ± 3
7	-	-	2 ± 1
8	-	-	2 ± 1
9	-	-	2 ± 1

Table 6.4: The number of events selected in each bin of |t| for the e-tagger33 centre-of-mass energy range.

In the highest five bins, however, the events are counted. This is again done using a mass window of $2.44 < m < 3.16$ GeVc^{-2}. The number of events obtained in each bin are listed in Table 6.4.

6.8 Calculation of the Trigger Efficiencies.

The efficiencies of the subtriggers used to select diffractive events from data collected in 1997 are needed to map the number of events obtained in each bin of t back to the number of events that were actually reconstructed by the detection system. Not every event produced will fire the triggers used. The efficiency of each subtrigger for selecting J/Ψ events is calculated using the number of data events found in the mass region $1.6 < m < 4.6$ GeVc^{-2}, which surrounds the J/Ψ peak. To do this a subtrigger s80 is chosen to act as a 'reference' trigger. A record of the number of events found in the same mass range, in each bin of t, by subtrigger s80 was also obtained by the selection code. Subtrigger s80 fires if an event causes a hit in one of the e-taggers. In the e-tagger44 centre-of-mass energy range the track subtrigger s81 was used to select events. The fraction of events which fired subtrigger s80 which also fire subtrigger s85 gives a measurement of the track trigger element's efficiency for identifying events from the sample collected by subtrigger s80. Subtrigger s85 also requires a hit in the e-taggers, however, since it also requires

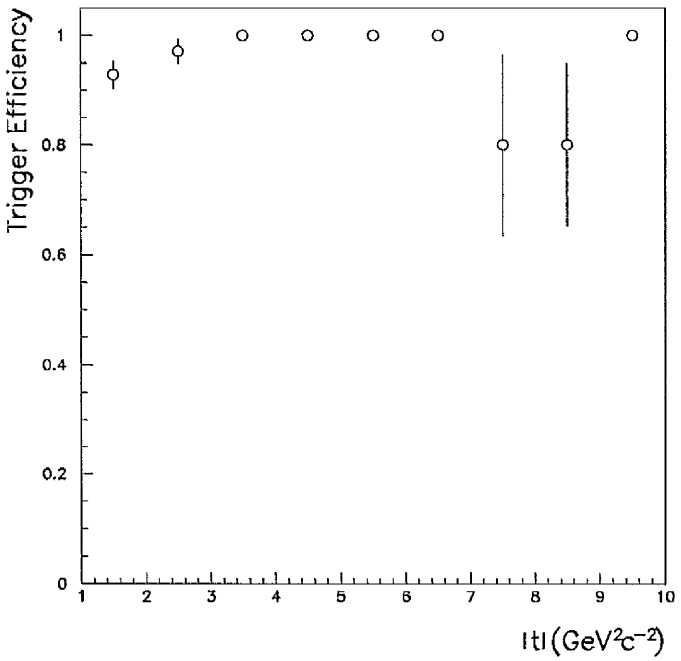

Figure 6.17: The efficiency of the track trigger element as a function of |t| in the e-tagger44 centre-of-mass energy range.

a negative track in an event, a smaller number of events is expected to fire s85. The efficiency of the e-tagger trigger element is already included in the e-tagger acceptance functions.

The subtriggers s80 and s85 have different prescale factors, however, and these need to also be incorporated into the calculation of the luminosity. The definition of a trigger prescale factor was given in section 5.6. The prescale factors of both subtriggers may vary from one data run to the next. An average prescale factor was calculated by finding a weighted average, the prescale factors weighted according to the luminosity of each run. The general expression for best estimate of the weighted mean is given by

$$\mu = \frac{1}{\mathrm{w}} \sum_{\mathrm{i}=1}^{\mathrm{n}} \mathrm{w_i x_i}$$

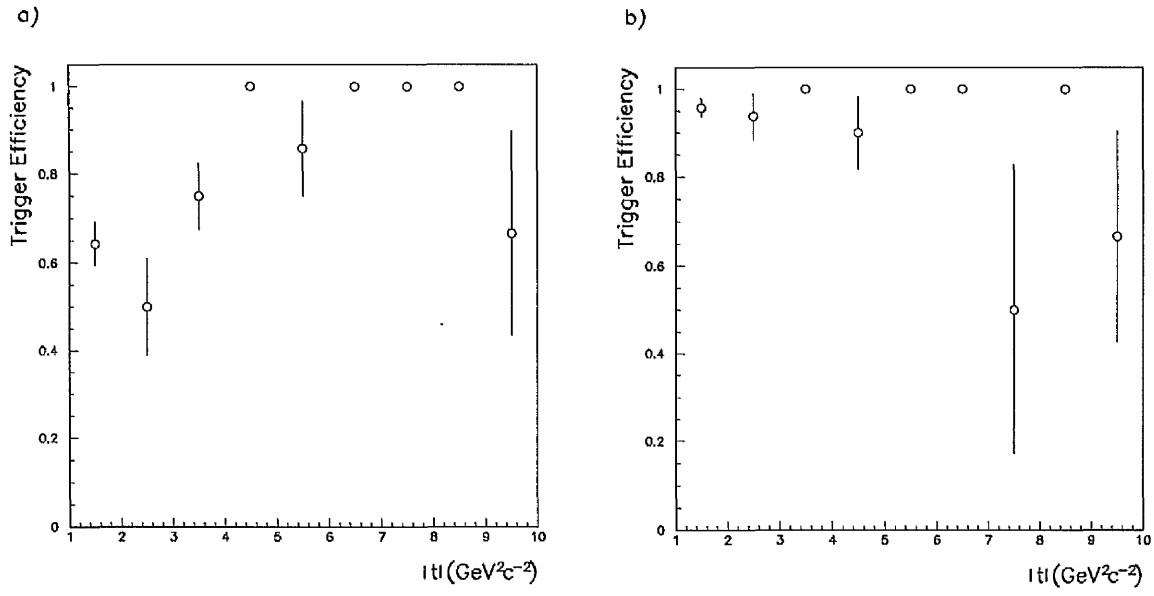

Figure 6.18: The efficiencies of a) the SPACAL and b) the track trigger elements as a function of |t| in the e-tagger33 centre-of-mass energy range.

where

$$w_i = \frac{1}{\sigma_i^2}$$

and w is just the sum of the w_i terms. The average prescale factor of subtrigger s80 was 332.61 and the average prescale factor of subtrigger s85 was 189.84. The trigger efficiency is independent of the trigger prescales and is calculated according to

$$\epsilon = \left(\frac{N_{80+85}}{N_{80}}\right)$$

The binomial uncertainties in the trigger efficiencies are obtained in each t-bin acording to

$$\frac{\sigma_\epsilon^2}{\epsilon} = \frac{(1-\epsilon)}{N_{80}}$$

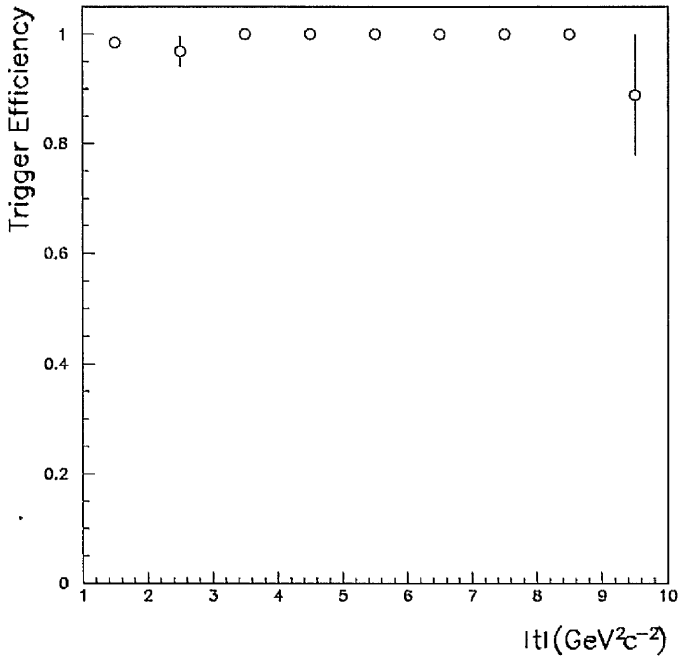

Figure 6.19: The combined efficiency of the track and SPACAL trigger elements as a function of |t| in the e-tagger33 centre-of-mass energy range.

The uncertainities in the prescale factors are given by $\frac{1}{\sqrt{w}}$ and are neglected in the calculation of the luminosity. The efficiency of the track trigger element as a function of t is shown in figure 6.17. The efficiency of the track trigger element in the range $|t| = 0 - 1$ GeV^{2}c^{-2} was 0.88 ± 0.02.

The same procedure is then applied to find the efficiencies of the track and the SPACAL trigger elements in the higher centre-of-mass energy range. The average prescale factor of the SPACAL subtrigger s81 was 109.52. The efficiencies of the track and the SPACAL trigger elements are both shown in figure 6.18. The efficiency of the track trigger element in the $|t| = 0-1$ GeV^{2}c^{-2}-range was 0.56 ± 0.03 and the efficiency of the SPACAL trigger element was 0.56 ± 0.03 in this range. The trigger efficiencies are then combined, in each bin, to give a single trigger efficiency

according to

$$\epsilon_c = 1 - (1 - \epsilon_{85})(1 - \epsilon_{81})$$

The combined uncertainty is obtained from the uncertainties on the individual sub-triggers by summing in quadrature according to

$$\sigma_c^2 = \left(\frac{\partial \epsilon_c}{\partial \epsilon_{81}}\right)^2 \sigma_{81}^2 + \left(\frac{\partial \epsilon_c}{\partial \epsilon_{85}}\right)^2 \sigma_{85}^2$$

The combined trigger efficiency is shown in figure 6.19. The combined trigger efficiency in the range $|t| = 0 - 1$ GeV^{2}c^{-2} was 0.81 ± 0.02.

Inspection of figure 6.17 suggests that the trigger efficiency of the track trigger element does not vary with t in the e-tagger44 centre-of-mass energy range above $|t| \sim 4.0$GeV^2. The slight fluctuations at larger values of t are introduced since the available statistics decrease at larger t. A single value for the trigger efficiency is therefore used across the range $|t| > 4.0$GeV^2. It is obtained by taking a weighted average of the trigger efficiencies obtained in each bin and is given by 0.9999 ± 0.0004. The individual trigger efficiencies of the first three bins are used, together with their individual uncertainties, in the calculation of the cross section later.

In the higher centre-of-mass energy range the efficiency of the track trigger element also shows no t-dependence. The efficiency of the SPACAL trigger element, however, shows a dip at low values of t. When the two trigger efficiencies are combined this is removed by the track trigger efficiency. A single value for the combined trigger efficiency is taken over the entire t-range. It is once again formed by taking a weighted average, and is given by 0.9999 ± 0.0002.

6.9 Smearing Effect in the t-Distribution.

6.9.1 Smeared Acceptances.

It has already been mentioned when examining the purities of the chosen t-bins that events which are produced in a particular t-bin may be reconstructed at a value which places them in a different t-bin to the one in which the event

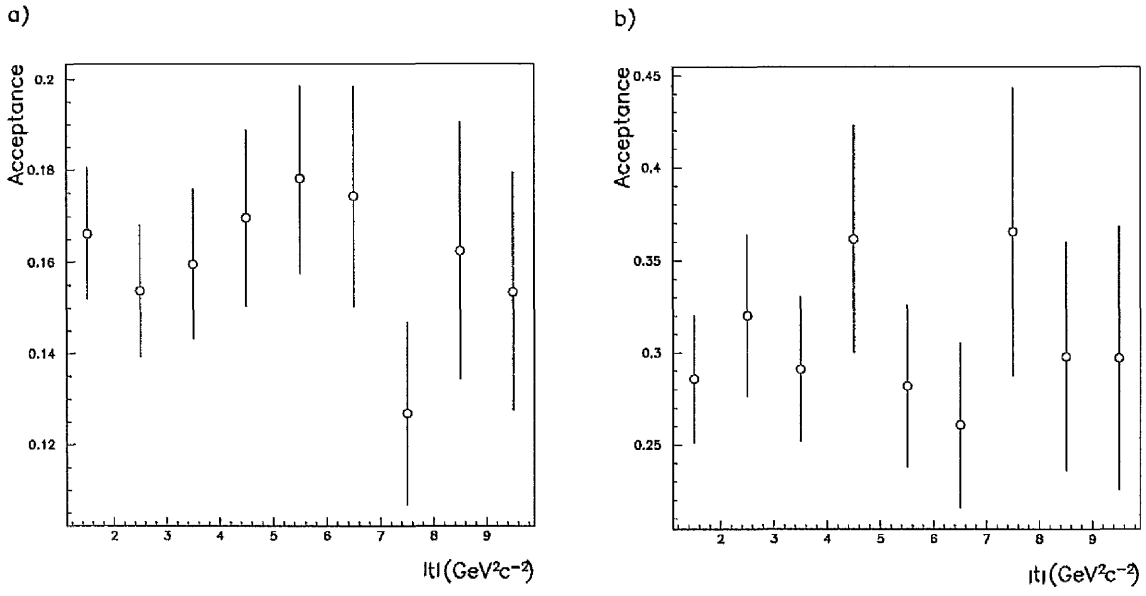

Figure 6.20: The smeared acceptances as a function of |t| for events selected in a) the e-tagger44 and b) e-tagger33 centre-of-mass energy ranges.

was actually produced. At this stage, therefore, the number of events which have been reconstructed in each bin of t will include events which were actually produced elsewhere. To account for this smearing effect it is possible to either adjust the error in the height of the cross section in each bin, or alternatively correct the number of events reconstructed. The second method is used here. The 'smeared' acceptances of the selection code for reconstructing diffractive J/Ψ events in each bin of t are however also presented for events selected in both centre-of-mass energy ranges in figure 6.20 (HITVM with an input value of $\alpha_s = 0.2$ is used here). The acceptances are calculated according to

$$A = \frac{N_R}{N_G}$$

where N_R is the number of events reconstructed in a particular t-bin, regardless of where they were generated, and N_G, as before, is the number of events generated in the bin. The errors are calculated from the expression for the acceptance written in terms of independent quantities. This method is described later.

6.9.2 Smearing Effect Corrections in t.

The number of events that smear into a particular bin depends upon the form of the t-distribution. In any particular bin a certain percentage of events in neighbouring bins will be reconstructed there. If the number of events produced in a neighbouring bin is larger than described by the monte carlo then the number of events which smear into other bins will be also be larger. There is no reason to assume that the generated t-distribution, based on the QCD calculation, is correct. The distribution by which events generated in each t-bin are reconstructed by the selection code may, however, be described by a matrix. Each element of the matrix represents the fraction of events produced in one particular bin that are expected to be reconstructed in a particular bin. The diagonal elements of the matrix describe the fraction of events that are expected to be reconstructed in the same bin. The off-diagonal elements therefore describe the smearing effect. Each off-diagonal element A_{ij} then describes the fraction of events generated in bin j that are expected to be reconstructed in bin i.

When the matrix operates on the column vector $\bar{n}_G$ constructed from the number of events generated in each bin it produces a column vector $\bar{n}_R$ of the number of events reconstructed in each bin as follows

$$A\bar{n}_G = \bar{n}_R$$

Writing out the first row in full, for example, gives

$$A_{11}n_G^1 + A_{12}n_G^2 + \ldots = n_R^1$$

The number n_R^1 that are reconstructed in this bin is obtained by summing the number that were generated and reconstructed in this bin with the extra numbers of events that enter from other bins.

The matrices describing how the generated events will be reconstructed are shown in figures 6.21 and 6.22. The matrices include the smearing of events from t-values in the range $0 - 1$ GeV^{2}c^{-2} into the region in which the differential cross section is to be measured. The matrices are therefore 10×10 matrices. Expanding the first row of the matrix gives an expression for the number of events reconstructed in the $0-1$ GeV^{2}c^{-2} t-range. The second row then corresponds to the $1-2$ GeV^{2}c^{-2} t-range and so on. The distribution of events generated in the first column are cal-

.16763	.01002	.00460	.00006	0	0	0	0	0	0
.00316	.14883	.01868	.00177	0	0	0	0	0	0
0	.00769	.12919	.01670	.00136	.00027	0	0	0	0
0	.00023	.00684	.13173	.02361	.00080	0	0	0	0
0	0	0	.01222	.13305	.02214	.00017	.00083	0	0
0	.00077	0	.00104	.00875	.12266	.05136	.00735	.00100	0
0	0	0	0	0	.01202	.11753	.03715	.00797	.00093
0	0	0	0	0	.00013	.01823	.07728	.02886	.00914
0	0	0	0	0	0	.00072	.01341	.10604	.03160
0	0	0	0	0	.00007	0	.00164	.01518	.09665

Figure 6.21: The acceptance matrix describing the smearing effect in the t-distribution in the e-tagger 44 centre-of-mass energy range.

.18200	.02905	0	0	0	0	0	0	0	0
.00432	.23174	.05802	.00262	.00097	.00328	.00255	0	0	0
0	.02687	.23137	.05809	.00488	0	0	0	0	0
0	.0013	.02381	.19074	.06779	.02175	.00662	.00195	0	0
0	0	0	.02896	.22137	.09398	.01416	0	.00405	0
0	0	0	0	.02667	.15701	.08894	.02603	.00560	.00672
0	0	0	0	0	.02362	.14333	.08603	.01966	.00341
0	0	0	0	0	.00337	.02755	.17696	.13286	.02767
0	0	0	0	0	0	.00222	.04981	.12629	.09659
0	0	0	0	0	0	0	0	.02600	.13508

Figure 6.22: The acceptance matrix describing the smearing effect in the t-distribution in the e-tagger 33 centre-of-mass energy range.

culated using the monte carlo event generator DIFFVM. This is based on the Regge theory pomeron. A proton dissociative version of DIFFVM for J/Ψ production is chosen.

The number of events reconstructed in each bin of t was determined in section 6.7. The matrix equation now needs to be inverted so that the number of events produced before smearing can be calculated from the number of events reconstructed. The inverse of the matrix A needs to be obtained. An iterative procedure was used to approximate the inverse acceptance matrices. The matrices are both close to being diagonal matrices. The acceptance matrix is therefore written as follows

$$A = T + \Delta$$

where the T-matrix contains only the diagonal entries and the matrix Δ contains all the off-diagonal elements. The matrix equation may therefore be written as

$$T\bar{n}_G = \bar{n}_R - \Delta\bar{n}_G \tag{6.2}$$

As a first approximation one may take the number of reconstructed events to be dominated by the diagonal elements. The column vector of generated events is then given by the inverse of T operated on the column vector of reconstructed events

$$\bar{n}_G = T^{-1}\bar{n}_R$$

The diagonal matrix T is easy to invert. The inverse matrix is also diagonal and contains the reciprocal of each diagonal entry in T as its diagonal components. If this first approximation is then substituted into the right hand side of Equation 6.2 a better approximation for $\bar{n}_G$ is obtained. This is given by

$$\bar{n}_G = (T^{-1} - T^{-1}\Delta T^{-1})\bar{n}_R$$

The process may be repeated, substituting this into the right hand side of equation 6.2 to give a third approximation as follows

$$\bar{n}_G = (T^{-1} - T^{-1}\Delta T^{-1} + T^{-1}\Delta T^{-1}\Delta T^{-1})\bar{n}_R.$$

	σ	a	N	A	χ^2
e-tagger44	0.061 ± 0.01	0.127 ± 0.003	122 ±12	72 ± 7	1.28
e-tagger33	0.055 ± 0.04	0.138 ± 0.007	191 ± 19	84 ± 8	2.61

Table 6.5: The results of the fit, together with the number (N) of reconstructed events obtained, in the e-tagger44 and e-tagger33 centre-of-mass energy ranges.

To use this procedure the number of events reconstructed in the range $|t| = 0 - 1$ GeV^{2}c^{-2} needs to be found. This is possible since the selection code makes no restriction on the value of t. The same function is used to fix the a and σ parameters as was used in the other bins. The function is then fitted to the data, including a straight-line dependence to describe the lepton-pair background, which peaks at a mass of 2.2 GeVc^{-2}. The results of the fits to the monte carlo and data distributions, are shown in figures 6.23 and 6.24, for e-tagger44 and e-tagger33 selected events respectively. The values of the parameters and the number of events obtained, together with their associated uncertainties, are listed in Table 6.5.

The results of the iteration procedure are shown in Tables 6.6 and 6.7. The procedure is stopped after five iterations since the size of the changes in the components of the column vector $\bar{n}_G$ with each iteraction start to become smaller than the size of the statistical errors on the components in the first approximation. The column vector $\bar{n}_G$ is clearly converging on a particular value with each iteration. The off-diagonal components of the acceptance matrices must therefore be small in comparison to the diagonal components.

The errors on the elements of the acceptance matrices are calculated using the normal binomial expression. These, together with the statistical errors on the first approximation are propagated through the iteration procedure to obtain a statistical error on the fifth iteration values, together with a systematic error arising from the uncertainties in the matrix elements. This is done by first propagating the errors on each matrix element through the series expansion to fifth order to give a single fifth order inverse matrix with errors on each component. When two components are multiplied along the way their percentage errors are added in quadrature. If two values added, for example when a row and a column are expanded, the actual errors are added in quadrature. This operation was performed by a computer subroutine which was checked to third order by hand.

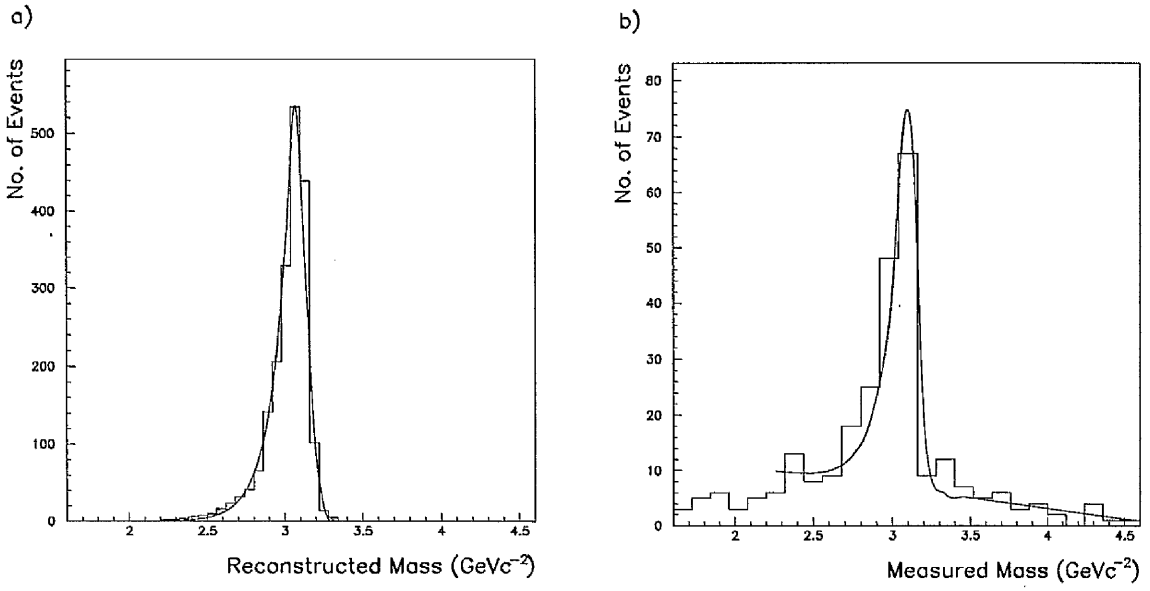

Figure 6.23: The result of the functional fit to the e-tagger44 mass distributions for a) monte carlo events and b) events selected from data in the $0.0 < |t| < 1.0$ GeV^{2}c^{-2} bin.

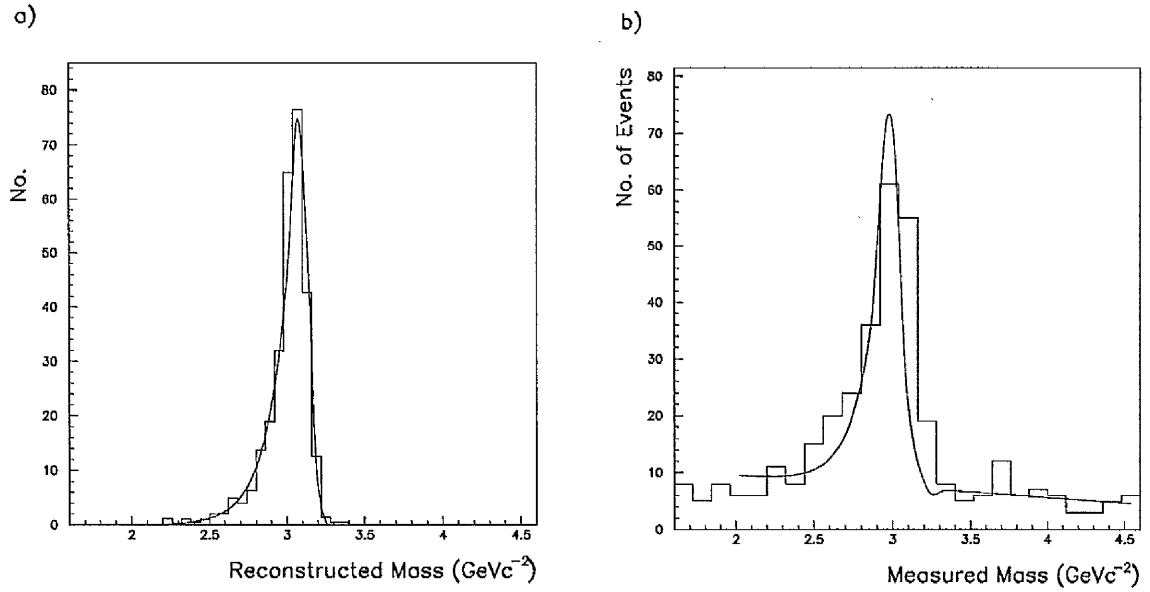

Figure 6.24: The result of the functional fit to the e-tagger33 mass distributions for a) monte carlo events and b) events selected from data in the $0.0 < |t| < 1.0$ GeV^{2}c^{-2} bin.

Rec. Events	1st Approx	2nd Approx	3rd Approx	4th Approx	5th Approx
121.97	727.67	714.49	715.35	716.43	716.33
26.23	176.24	163.05	148.54	149.52	149.31
13.60	105.28	92.73	85.18	86.57	86.37
11.49	87.22	74.74	71.01	71.87	71.36
9.71	72.98	60.50	58.40	60.75	60.30
7.00	57.07	44.59	32.54	34.87	34.47
6.00	51.05	38.57	33.57	34.41	34.99
4.00	51.76	39.28	39.23	37.36	38.43
2.00	18.86	6.38	11.18	8.01	8.46
2.00	20.69	8.21	18.99	18.25	18.78

Table 6.6: The results of the acceptance matrix iteration procedure for the e-tagger44 sample. A better approximation for the number of events actually produced is obtained with each iteration.

Rec. Events	1st Approx	2nd Approx	3rd Approx	4th Approx	5th Approx
191.23	1050.81	1037.27	1039.43	1042.26	1041.76
19.66	84.83	71.29	53.57	56.67	55.84
12.34	53.33	41.95	30.09	33.05	31.23
13.31	69.78	58.40	55.43	60.83	59.17
5.63	25.43	14.05	6.63	11.71	12.80
5.00	31.85	20.46	7.95	4.09	5.07
7.00	48.84	37.46	44.82	44.75	51.81
2.00	11.30	-0.78	1.20	-7.46	-0.61
2.00	15.84	4.46	12.59	3.91	8.52
2.00	14.81	3.43	13.94	12.38	14.05

Table 6.7: The results of the acceptance matrix iteration procedure for the e-tagger33 sample. A better approximation for the number of events actually produced is obtained with each iteration.

Finally the errors on each element $\bar{n}^i_G$ of the column vector of events actually produced before smearing is obtained according to

$$\sigma^2(\bar{n}^i_G) = \sum_j \left[(A_{ij})^2\sigma^2(\bar{n}^j_R) + (\bar{n}^j_R)^2\sigma^2(A_{ij})\right].$$

The first term describes the statistical error and the second describes the additional systematic error arising from the uncertainty in the matrix elements.

6.10 Smearing of Inelastic and Elastic Events

To see if inelastic events are sometimes thrown out by the method of separating elastic and inelastic events the total energy of the event, excluding the scattered positron energy, is compared to the energy of the J/Ψ. In elastic events the total energy of the final state, where the scattered positron is excluded, is expected to approximately equal the energy of the J/Ψ. The two quantities are therefore subtracted from each other. A peak is then expected at zero for elastic and low mass inelastic events.

The difference in these two quantities, for events which were selected as being elastic, of events generated by HITVM is shown in figure 6.25. All the events generated by this monte carlo were inelastic. It can be seen that the number of inelastic events that are defined as being elastic is small. The same distribution for those events that were considered as being inelastic is also shown in figure 6.25. The long tail towards higher values contains a much larger number of events. Inelastic diffractive events are therefore not expected to be mis-identified as being elastic in a very large number of cases.

The same distributions are essentially then plotted using elastic events generated by DIFFVM. Those events which were considered to be elastic, over the whole generated t-range starting at a t-value of zero, are shown in figure 6.26. Those events which were considered to be inelastic, in the range of t greater than $|t| = 1.0\ GeV^2c^{-2}$, are also shown in this figure. Approximately 9% of the generated elastic events are therefore expected to smear into the inelastic distribution.

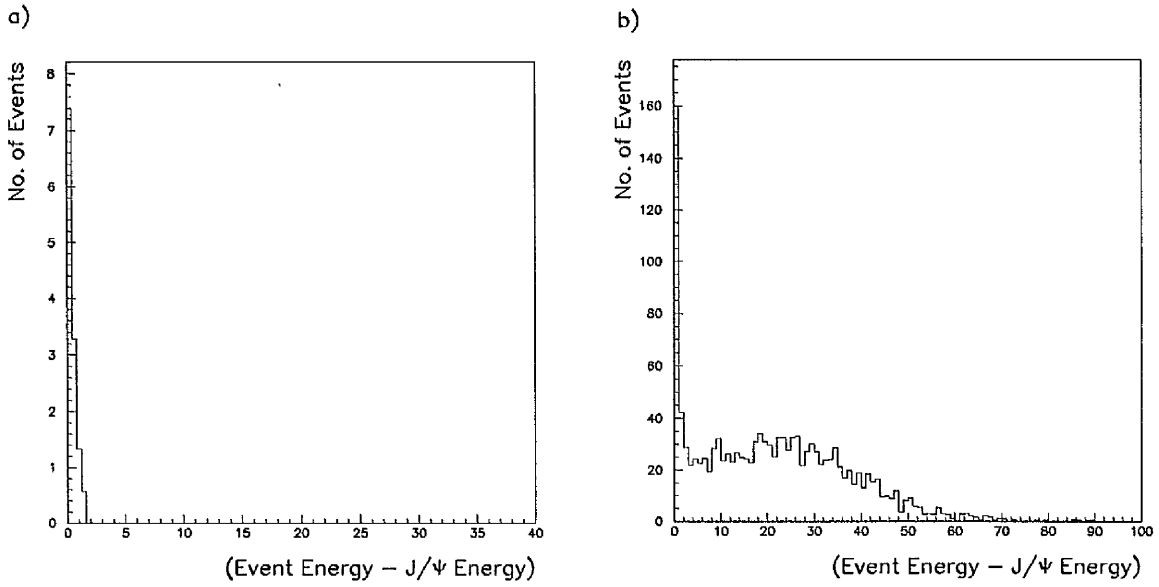

Figure 6.25: The energy of the final state (excluding the scattered positron) minus the energy of the J/Ψ (GeV) for a) elastic and b) inelastic selected HITVM events.

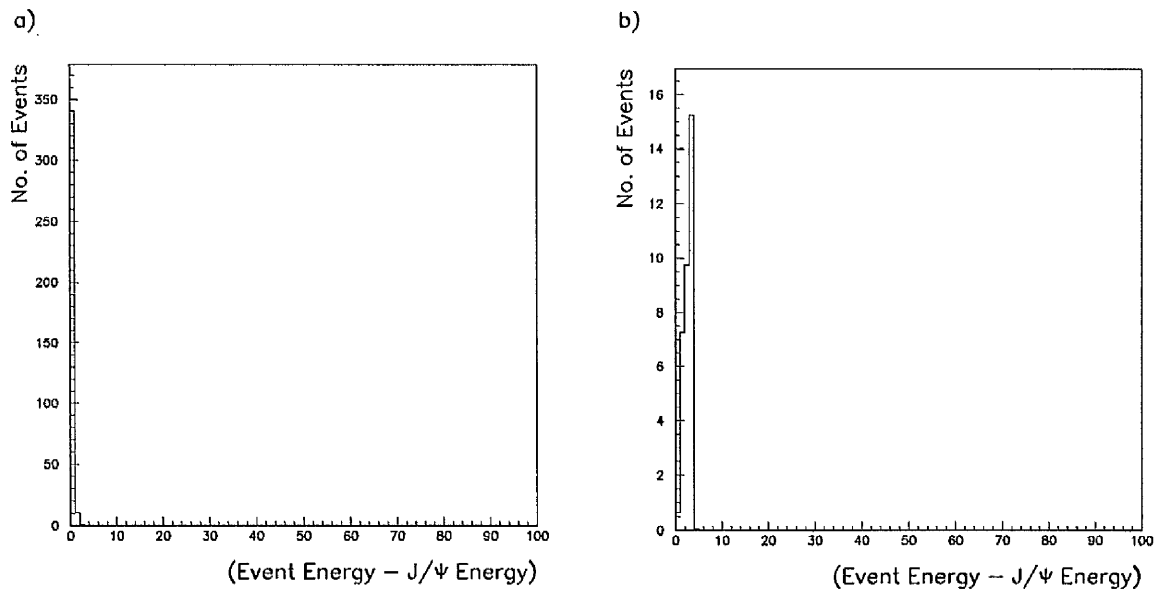

Figure 6.26: The energy of the final state (excluding the scattered positron) minus the energy of the J/Ψ (GeV) for a) elastic and b) inelastic selected DIFFVM events.

6.11 Luminosity Measurement

The total luminosity for 1997 data is measured by the luminosity system of the H1 detector. The components of the luminosity system were described in section 5.4. This is done by selecting Bethe-Heitler events. The cross section of the Bethe-Heitler process

$$e^+ + p \longrightarrow \gamma + e^+ + p$$

is well understood. The instantaneous luminosity (L) is calculated from the rate (R) of Bethe-Heitler events as follows

$$L = \frac{R}{\sigma}$$

The integrated luminosity (L) of a data run is calculated at the end of a run from the total number (N) of Bethe-Heitler events which occured according to

$$L = \frac{N}{\sigma}$$

In both cases σ describes the cross section of the Bethe-Heitler process. There are several different methods for determining the rate and the number of Bethe-Heitler events. The coincidence method requires the simultaneous detection of the outgoing scattered positron and the photon. The single photon method counts the rate or the total number of photons above a certain energy threshold in the photon detector. The coincidence method is used for the online determination of the luminosity whereas the single-photon method is used to obtain the final value of the integrated luminosity. The integrated luminosity for the 1997 data-taking period was determined according to the single-photon method. The value obtained includes only those runs which were classified as 'good' or 'medium', since these were the only runs considered in the analysis. It is also corrected for the prescale of subtrigger s80 to which the other subtriggers were normalised when calculating the trigger efficiencies. It is also corrected for the acceptance of the e-taggers. The value obtained for the integrated luminosity was 21.5 inverse picobarns.

6.12 Differential Cross Sections in t.

The measured quantities of the previous sections are now all brought together to calculate the cross section in each bin of t. The cross section in each t-bin is calculated according to

$$\sigma = \frac{N_G}{\epsilon b L}$$

where N_G represents the number of events produced in the bin and found by the matrix iteration procedure, ϵ represents the trigger efficiency for that bin, L is the total integrated luminosity for 1997 data, corrected for the effects described in the previous section and b is the branching ratio for the J/Ψ to decay into an electron-positron pair. The branching ratio is included since the cross section for J/Ψ production is required for all decay modes, not just the contribution from the e^+e^- decay mode. The branching ratio for the decay of the J/Ψ to an electron-positron pair is 6.02%. The bin widths are all 1 GeV^2c^{-2} wide and so there is no need for an additional correction for the bin width. The differential cross sections for electron-proton scattering are shown in figure 6.27. Both centre-of-mass energy ranges are shown on the same plot. The cross sections in the range $|t| = 0 - 1$ GeV^2c^{-2}, not shown on this plot, are given by $0.611 \pm 0.061|_{stat} \pm 0.064|_{sys}$ nb $GeV^{-2}c^4$ in the e-tagger44 centre-of-mass energy range and $1.01 \pm 0.11|_{stat} \pm 0.10|_{sys}$ nb $GeV^{-2}c^4$ in the e-tagger33 centre-of-mass energy range. The bin centres in the higher centre-of-mass energy range have been slightly offset in figure 6.27 so that the errors may more easily be distinguished from those in the lower centre-of-mass energy range.

An additional error in the height arises from the quantities which take the same value in each bin. It is calculated according to

$$\left(\frac{\sigma_\sigma}{\sigma}\right)^2 = \left(\frac{\sigma_L}{L}\right)^2 + \left(\frac{\sigma_\epsilon}{\epsilon}\right)^2 + \left(\frac{\sigma_b}{b}\right)^2.$$

The error in the luminosity is 1.5 percent, the error in the trigger efficiency, calculated according to a weighted average is stated previously, and the error in the measured branching ratio is 0.03%. Combining all of these together gives an additional error of 1.5% in the height of the e-tagger44 centre-of-mass energy distribution from bin number 4 upwards. The errors in the trigger efficiencies in the first three bins, where the bin efficiencies were used, are shown together with the errors on these points in the plot. An additional error of 1.5% in the height of the e-tagger33 centre-of-mass energy distribution is obtained.

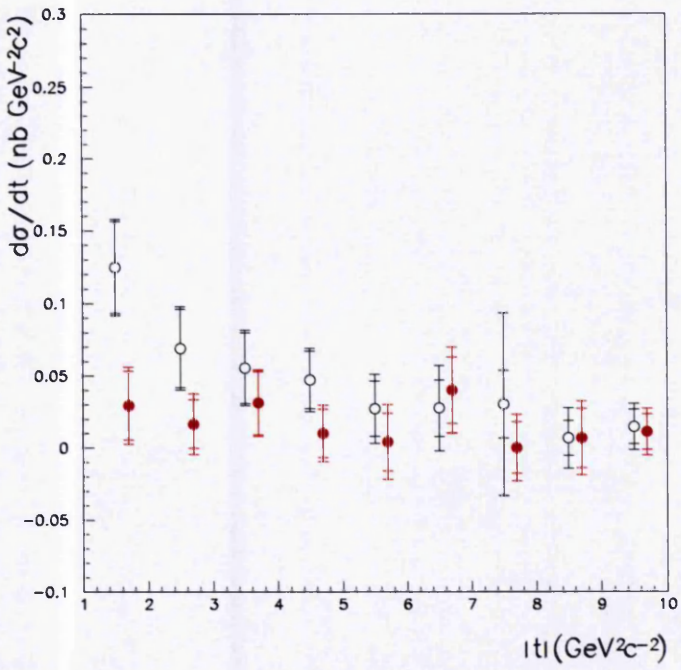

Figure 6.27: The differential cross section $d\sigma/dt$ as a function of the $|t|$ for $e^+p \rightarrow J/\Psi$ Y. The centre-of-mass energy range 60 GeV $< W_{\gamma p} <$ 147 GeV is shown in black and the centre-of-mass energy range 165 GeV $< W_{\gamma p} <$ 233 GeV is shown in red. The outer error bars represent the systematic uncertainties.

The Regge theory and QCD calculations are performed for two particles entering and two particles leaving the interaction region. These measurements therefore need to be converted into photon-proton differential cross sections. This may be done by dividing by the incoming flux of transversely polarised photons. The flux is calculated by integrating

$$\Gamma_T = \frac{\alpha_{em}(1 - y + \frac{y^2}{2})}{\pi y Q^2}$$

over the y-range to which the measurements apply. The fluxes are 0.01 in the e-tagger33 range and 0.03 in the e-tagger44 range. The photon-proton differential cross sections in both centre-of-mass energy ranges are shown in figure 6.28. The cross sections at low $|t|$ are $20.3 \pm 2.0|_{stat} \pm 2.1|_{sys}$ nb $GeV^{-2}c^2$ for e-tagger44 events and $101.3 \pm 10.9|_{stat} \pm 10.3|_{sys}$ nb $GeV^{-2}c^2$ for e-tagger33 events.

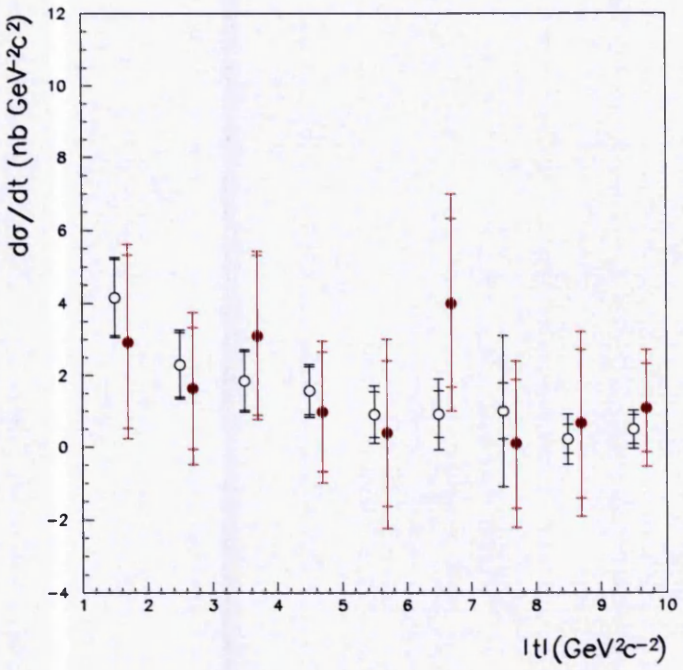

Figure 6.28: The differential cross section $d\sigma/dt$ as a function of the |t| for $\gamma p \rightarrow J/\Psi$ Y. The centre-of-mass energy range 60 GeV $< W_{\gamma p} <$ 147 GeV is shown in black and the centre-of-mass energy range 165 GeV $< W_{\gamma p} <$ 233 GeV is shown in red. The outer error bars represent the systematic uncertainties.

The centre-of-mass energy of the photon-proton system squared ($W^2_{\gamma p}$) to which these measurements correspond may be calculated from the Bjorken y range of the e-taggers. In photoproduction the photon-proton centre-of-mass energy squared is calculated at a particular value of Bjorken y according to

$$W^2_{\gamma p} = ys$$

where s is the centre-of-mass energy squared of the positron-proton system. This is approximately equal to 90530 GeV^2 at HERA. The energy range covered by e-tagger44 is then given approximately by 60 $< W_{\gamma p} <$ 147 GeV and the energy range covered by e-tagger33 is given approximately by 165 $< W_{\gamma p} <$ 233 GeV.

Chapter 7

Analysis of the Centre-of-Mass Energy Dependence.

It was explained in chapter 2 that at low centre-of-mass energies net particle states scatter via the exchange of Reggeons with intercepts less than unity. Scattering processes which proceed via the exchange of the same Reggeon may be related by crossing symmetry. The five processes related to π^+-proton elastic scattering, which all proceed via the exchange of the Delta trajectory, were then identified. It was explained that one charged version of the Delta resonance, the first point on the Delta trajectory, is produced as a resonance in each of these related processes. At slightly higher centre-of-mass energies each of these processes then produce one charged version of the $\Delta(1950)$-resonance, the second point on this trajectory, and so on. The Regge trajectory which begins with the Delta resonance was shown in figure 2.9. At higher centre-of-mass energies the pomeron trajectory dominates many scattering processes. This is interpreted as being due to the similar constituents inside the larger hadronic states interacting with each other at these energies. At higher centre-of-mass energies six crossed constituent interactions could describe the many related scattering processes. At these energies, if a trajectory of bound states exist, then one version of the first state on pomeron trajectory is expected to be produced as a resonance in each process which tends to the pomeron trajectory. As the centre-of-mass energy is increased one version of the second particle on the pomeron trajectory should then be produced, and so on.

In this chapter the differential cross section $d\sigma/dW^2_{\gamma p}$ is investigated as a function of $s = W^2_{\gamma p}$ for processes in which a J/Ψ vector meson was once again produced at the photon vertex but in which the proton remained intact at the other vertex. No pomeron states are incorporated in the QCD calculation for pomeron exchange, however since a pomeron trajectory could exist with a non-zero gradient, it is necessary to use bin widths in $W^2_{\gamma p}$ which are as small as possible (as the gradient of the pomeron trajectory is allowed to become steeper the pomeron states become closer together in mass). This represents the first time that the differential cross section $d\sigma/dW^2_{\gamma p}$ has been investigated in this way.

The procedure for selecting events in which a single J/Ψ vector meson was produced at the photon vertex was described in the previous chapter. Here a proton dissociative sample was of interest and so events elastic at the proton vertex were removed in section 6.3. Those events which were defined as being proton dissociative in the previous chapter are now ignored and the events which were defined as being elastic are selected. The procedure for then extracting the differential cross section in $W^2_{\gamma p}$ is essentially identical to that used to extract $d\sigma/dt$ with the exception that, since the scattered lepton was tagged, no matrix correction method is used to correct for any potential smearing effect in $W^2_{\gamma p}$. Events produced outside of the ranges covered by the e-taggers would also be needed to do this. The analysis therefore particularly relies upon a correct modelling of the smearing effect in the monte carlo. This simplication is justified because the analysis aims to determine whether the method could be used to experimentally identify the pomeron states.

7.1 The Monte Carlo Event Generator DIFFVM.

The monte carlo event generator DIFFVM is chosen to describe proton elastic diffractive production of the J/Ψ vector meson. This generator is based on the non-perturbative calculations of Chapter 2. Proton intact and proton dissociative versions of this event generator have been written. The generated differential cross section $d\sigma/dt$ for photon-proton collisions in which the proton remains intact is given by

$$\frac{d\sigma}{dt} \sim W^{4\epsilon}_{\gamma p} e^{bt}.$$

For processes in which the proton dissociates the form is

$$\frac{d\sigma}{dt}dM_Y^2 \sim W_{\gamma p}^{4\epsilon} e^{b't} M_Y^{\beta}.$$

The parameters ϵ, b, b' and β are determined from fits to J/Ψ diffractive events at t values less than 1 GeV^2c^{-2}. The parameters of the proton dissociative event generator used in the analysis of the previous chapter were equal to $\epsilon = 0.225$, $b' = 1.6$ GeV^2c^{-2} and $\beta = 0.0808$. The parameters of the proton elastic event generator used here are equal to $\epsilon = 0.225$ and $b = 4$ GeV^2c^{-2}. Once again the decay distribution of the J/Ψ to an electron-positron pair is taken according to s-channel helicity conservation, as described for the event generator HITVM. A proton-intact version of DIFFVM, which covers the range in Bjorken y of $y < 0.4$, was selected. Each event was then subjected to a simulation of the H1 detector response. The acceptances of the electron taggers were added afterwards as described in the previous chapter.

7.1.1 Resolution in Bjorken y

The centre-of-mass energy squared ($W_{\gamma p}^2$) of the photon-proton system may be reconstructed from a measurement of the Bjorken scaling variable y. In the kinematic region of photoproduction the relationship is given by

$$W_{\gamma p}^2 = ys$$

where s is the centre-of-mass energy squared of the positron-proton system, equal to about 90530 GeV^2 at HERA. The energy resolution of the e-tagger at z=-44.0 metres is poor, so Bjorken y was constructed from a measurement of the $(E - P_z)$ of the final state, excluding the scattered positron, according to the method of Jacquet-Blondel in both e-tagger centre-of-mass energy ranges. The generated and reconstructed values of y for events in which the proton remained intact are compared in figure 7.1. Here events selected by e-tagger33 and e-tagger44 are presesented on the same plot. The full width at half height is about 0.0035. Bin widths in y must be at least as wide as the full width at half maximum. The width is chosen to be equivalent to $y = 0.0050$. Each y-bin therefore corresponds to a $W_{\gamma p}^2$-bin of about 450 GeV^2.

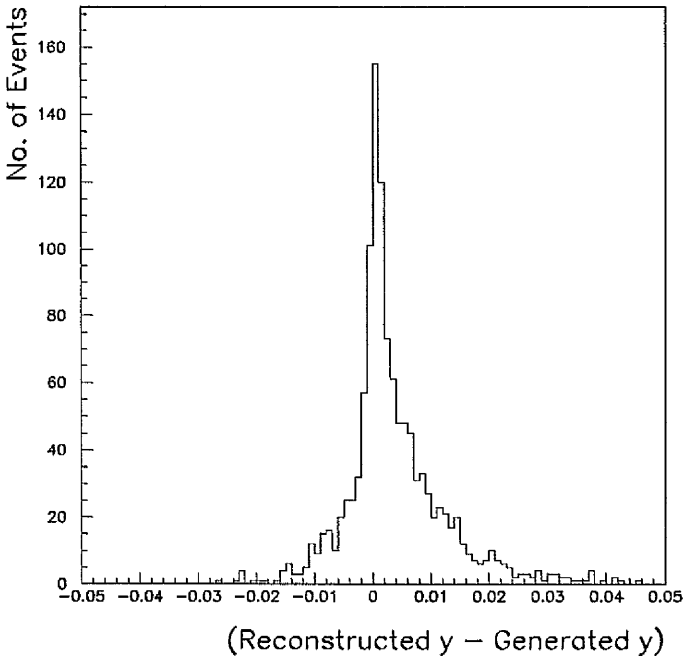

Figure 7.1: The separation of the reconstructed and generated values of Bjorken y for events selected by e-tagger33 and e-tagger44. Bjorken y was reconstructed according to the method of Jacquet Blondel.

7.1.2 Smeared Acceptances and Bin Purities.

The expression for the smeared acceptance (A) in each bin of t was presented in section 6.9.1. It was given by

$$A = \frac{N_R}{N_G}$$

where N_R is the number of events reconstructed in a particular bin, regardless of whether they were actually generated there, in which N_G events were actually generated. The smeared acceptances in each bin of $W^2_{\gamma p}$ for events selected by e-tagger44 are shown in figure 7.2. The distribution follows closely the acceptance function of e-tagger44. This is expected since the acceptance function selects events from the

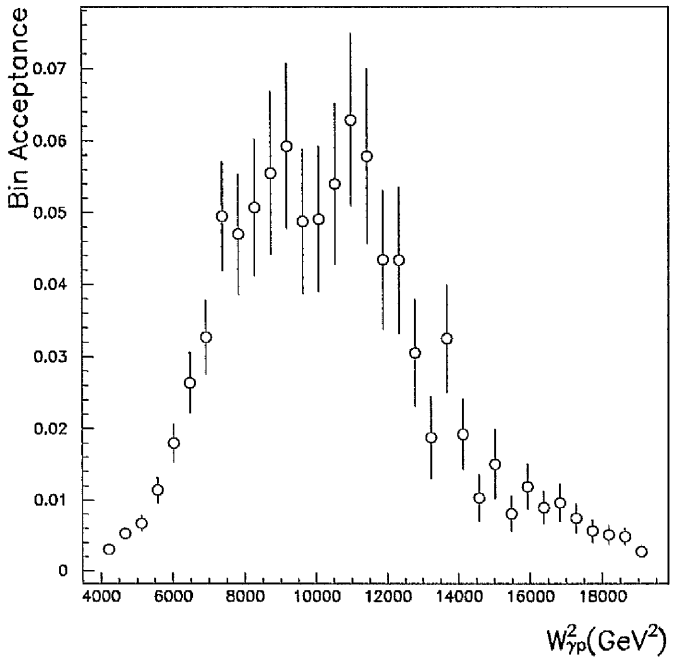

Figure 7.2: The smeared acceptances as a function of $W^2_{\gamma p}$ for events selected in the e-tagger44 centre-of-mass energy range.

smooth $W^2_{\gamma p}$-distribution generated by the monte carlo. Small deviations from the acceptance distribution are introduced by the selection code. The smeared acceptances in each bin of $W^2_{\gamma p}$ for events selected by e-tagger33 are shown in figure 7.3. The y-range covered by the monte carlo ends below the region where the acceptance of this e-tagger becomes high. The smeared acceptances are used to calculate the cross section $d\sigma/dW^2_{\gamma p}$ in each bin of $W^2_{\gamma p}$. The errors in the smeared acceptances are therefore to be incorporated in the total systematic error on the cross section. The number of events reconstructed in a particular bin, however, includes the number of events that smear in from other bins. The method of calculating errors by summing in quadrature can therefore not be used until the expression for the smeared acceptance has been expanded in terms of independent quantities.

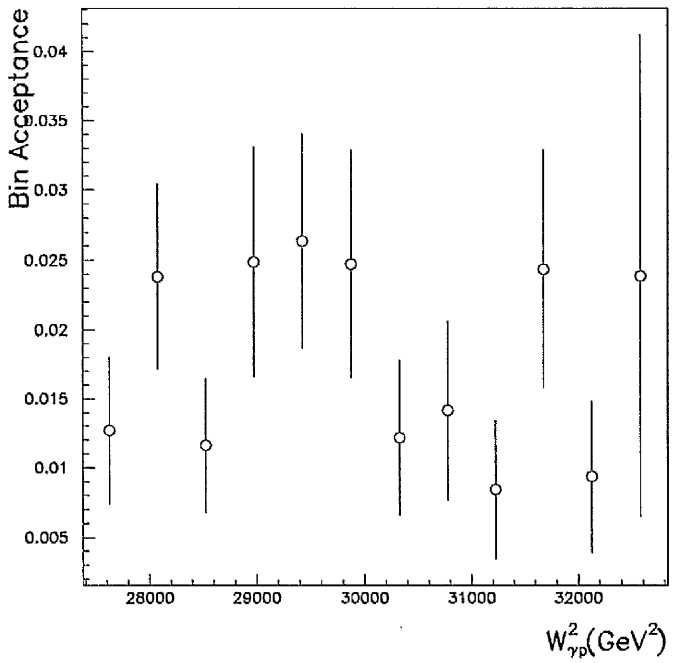

Figure 7.3: The smeared acceptance as a function of $W^2_{\gamma p}$ for events selected in the e-tagger33 centre-of-mass energy range.

The number of events reconstructed in a particular bin may be written as the sum of the number of events which were generated and reconstructed in that bin (N_{STAY}) and the extra amount (N_{ENTER}) that were reconstructed there but were generated in other bins, as follows

$$N_R = N_{STAY} + N_{ENTER}.$$

Since N_{STAY} is given by the number of events generated minus all those events which were generated but not reconstructed there (N_{LEAVE}) the expression for the acceptance may be written as

$$A = 1 - \frac{N_{LEAVE}}{N_G} + \frac{N_{ENTER}}{N_G}.$$

Using the original expression for the acceptance to replace N_G in the second term and rearranging gives

$$A = \frac{(1 - A_E)}{(1 + A_L)}$$

where $A_E = (N_{ENTER}/N_G)$ and $A_L = (N_{LEAVE}/N_R)$. These fractions are independent of each other. The number that enter a bin is independent of the number that were generated in that bin. The number that enter depends on the number that were generated in other bins. The number that leave a particular bin is also independent of the number that were reconstructed there. The fractional error in the acceptance may therefore be obtained by combining the errors on A_E and A_L in quadrature. The expression for doing this is given by

$$\left(\frac{\sigma_A}{A}\right)^2 = \frac{\sigma^2_{A_E}}{(1 - A_E)^2} + \frac{\sigma^2_{A_L}}{(1 + A_L)^2}$$

The uncertainty in A_E is given by

$$\sigma^2_{A_E} = \frac{\sigma^2_{N_{ENTER}}}{(N_G)^2} + \frac{N^2_{ENTER}}{N^4_G}\sigma^2_{N_G}.$$

Similarly the uncertainty in A_L is given by

$$\sigma^2_{A_L} = \frac{\sigma^2_{N_{LEAVE}}}{(N_R)^2} + \frac{N^2_{LEAVE}}{N^4_R}\sigma^2_{N_R}.$$

The uncertainty squared in the number of events generated is taken to be N_G since the monte carlo makes a decision as to what will happen to each generated event in turn. The squared uncertainties in the other quantities are obtained by summing the weights squared of each event. The events were weighted according to the acceptances of the e-taggers.

The bin purities, calculated in the same way as for the t-distribution in section 6.5.2, for events selected by e-tagger44 are shown in figure 7.4. The bin purities for events selected in the e-tagger33 centre-of-mass energy range are shown in figure 7.5. To calculate the errors in the bin purities a similar method was used as that described for the smeared acceptances. Some of the chosen bins in the e-tagger33 range have zero purities. The events which are obtained in these bins (the acceptances are not zero in these bins) were therefore all generated in other bins.

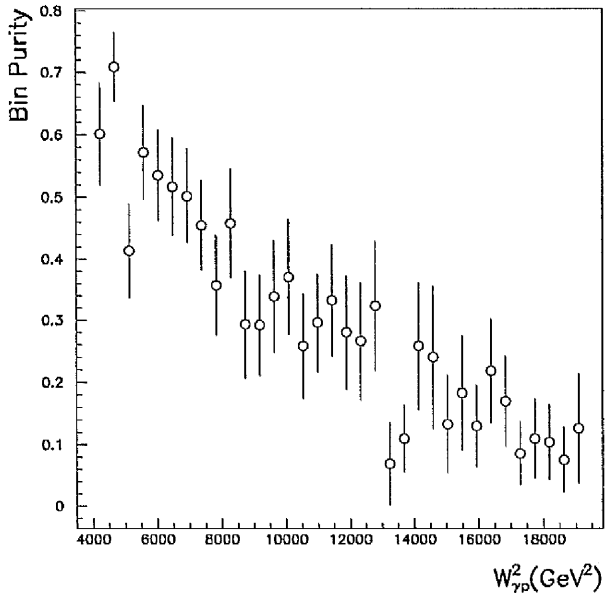

Figure 7.4: The purities in each bin of $W^2_{\gamma p}$ for events selected by e-tagger44.

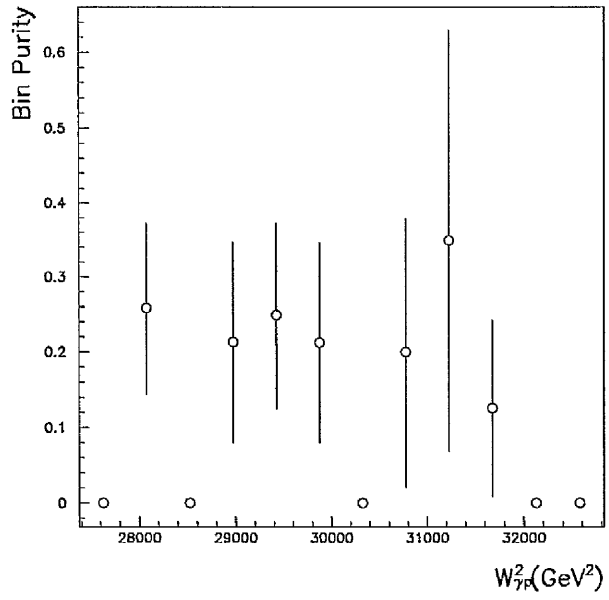

Figure 7.5: The purities in each bin of $W^2_{\gamma p}$ for events selected by e-tagger33.

7.2 Calculation of the Trigger Efficiencies

The trigger efficiencies will once again be needed for a calculation of the cross section in each bin of $W^2_{\gamma p}$. They are constructed using the same method described in section 6.8. Once again subtrigger s85 is used to select events in the e-tagger44 centre-of-mass energy region and this subtrigger together with subtrigger s81 are used to select events in the higher centre-of-mass energy region. The tagger subtrigger s80 is once again used as a reference. The efficiency of the track trigger element of subtrigger s85 is shown, for events selected in the e-tagger44 centre-of-mass energy range, in figure 7.6. The efficiency of the track trigger element appears to show no variation with $W^2_{\gamma p}$. The small variations are once again most likely due to the small numbers of events obtained. No events were reconstructed at the edge of this centre-of-mass energy range.

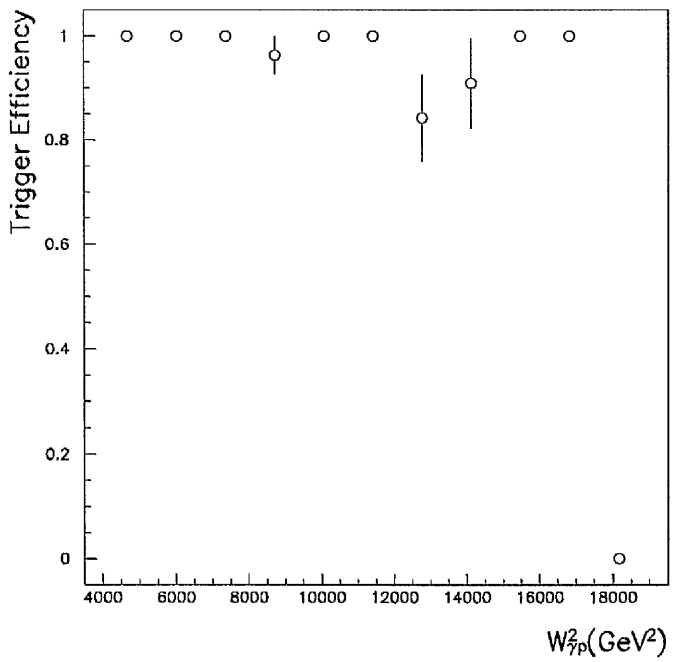

Figure 7.6: The efficiency of the track trigger element as a function of $W^2_{\gamma p}$ for events selected by e-tagger44.

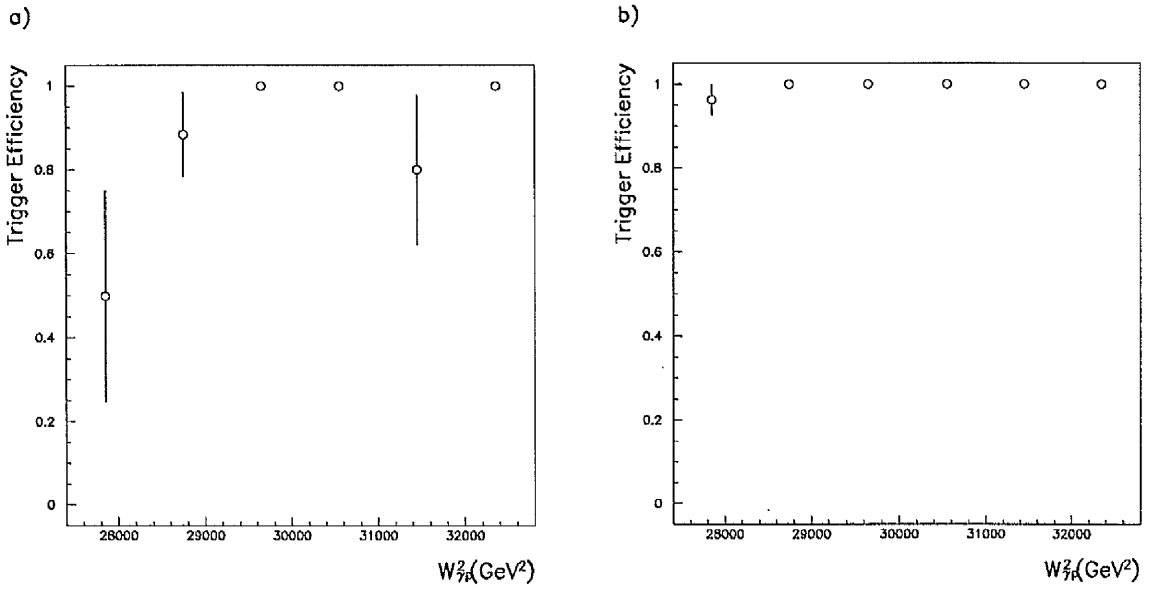

Figure 7.7: The efficiency of a) the SPACAL and b) the track trigger elements as a function of $W^2_{\gamma p}$ for events selected in the e-tagger33 centre-of-mass energy range.

The efficiency of the track trigger element is taken to be flat across the whole $W^2_{\gamma p}$ range. A single estimate is obtained by taking a weighted average. It is given, together with its associated uncertainty, by $\epsilon = 0.9997 \pm 0.0004$. The efficiency of track trigger element of s85 for events selected in the e-tagger33 centre-of-mass energy range is shown in figure 7.7b). The efficiency of the SPACAL trigger element of s81 is shown in figure 7.7a). The two trigger elements are combined together in the same way as for the t-analysis. The result is shown in figure 7.8. The combined trigger efficiency (ϵ_c) in this region is also taken to have no $W^2_{\gamma p}$-dependence. The best estimate of the combined trigger efficiency, together with its associated uncertainty, is $\epsilon_c = 0.98 \pm 0.02$.

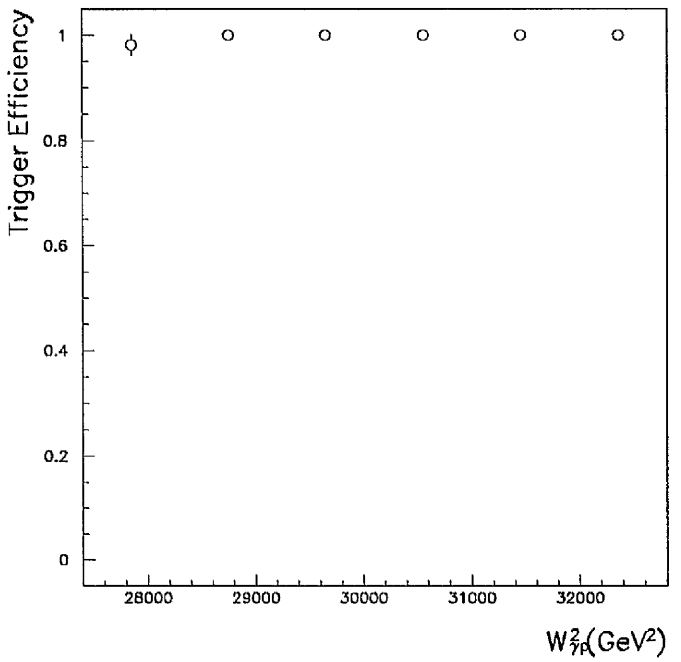

Figure 7.8: The combined efficiency of the SPACAL and track trigger elements as a function of $W^2_{\gamma p}$ in the e-tagger33 centre-of-mass energy range.

7.3 Background Subtraction in Data

The subtraction of background processes in each bin of $W^2_{\gamma p}$ is approached in a similar way to that undertaken in section 6.7. The sources of background discussed in section 6.6 are also expected to occur in the sample of proton-elastic events (The proton may remain intact in both the lepton pair-production process and when a higher mass charmonium state is produced at the photon vertex). Since the number of events obtained in each bin never rise to a height where a full functional fit would be justified, the number of events reconstructed within a mass window of $2.08 < m < 3.16$ GeVc^{-2} are counted. The same mass window is used in each centre-of-mass energy range. The number of events reconstructed are listed, together with their statistical errors ($\sqrt{N}$), in Table 7.1. The reconstructed mass distributions in each bin of $W^2_{\gamma p}$ are to be found in Appendix B of this thesis.

e-tagger44				e-tagger33	
Bin	No. of Events	Bin	No. of Events	Bin	No. of Events
1	0 ± 0	18	0 ± 0	1	3 ± 2
2	1 ± 1	19	4 ± 2	2	1 ± 1
3	0 ± 0	20	3 ± 2	3	1 ± 1
4	1 ± 1	21	3 ± 2	4	3 ± 2
5	3 ± 2	22	5 ± 2	5	1 ± 1
6	2 ± 1	23	2 ± 1	6	1 ± 1
7	2 ± 1	24	1 ± 1	7	1 ± 1
8	6 ± 2	25	1 ± 1	8	2 ± 1
9	6 ± 2	26	1 ± 1	9	4 ± 2
10	5 ± 2	27	0 ± 0	10	2 ± 1
11	5 ± 2	28	1 ± 1	11	2 ± 1
12	14 ± 4	29	1 ± 1	12	3 ± 2
13	6 ± 2	30	0 ± 0		
14	6 ± 2	31	0 ± 0		
15	9 ± 3	32	0 ± 0		
16	10 ± 3	33	0 ± 0		
17	4 ± 2	34	0 ± 0		

Table 7.1: The number of events reconstructed in each bin in the e-tagger44 and e-tagger33 centre-of-mass energy ranges together with their associated statistical uncertainties.

7.4 Differential Cross Section in $W^2_{\gamma p}$

The results of the previous sections are now all combined to give a measurement of the cross section in each bin of $W^2_{\gamma p}$. The positron-proton cross section σ in each bin is obtained according to the following expression

$$\sigma = \frac{N}{A\epsilon bLW}$$

where the bin has a width W, an acceptance A, N events were reconstructed there and ϵ refers to the trigger efficiency appropriate for that bin. The luminosity (L) is equivalent to the value calculated previously as described in section 6.11. Likewise the branching ratio (b) is unchanged. Of interest here is the photon-proton cross

e-tagger44				e-tagger33	
Bin	Photon Flux	Bin	Photon Flux	Bin	Photon Flux
1	0.002312	18	0.000729	1	0.000262
2	0.002068	19	0.000699	2	0.000256
3	0.001868	20	0.000670	3	0.000251
4	0.001702	21	0.000644	4	0.000246
5	0.001562	22	0.000619	5	0.000241
6	0.001443	23	0.000596	6	0.000236
7	0.001339	24	0.000575	7	0.000232
8	0.001248	25	0.000555	8	0.000227
9	0.001169	26	0.000536	9	0.000223
10	0.001098	27	0.000518	10	0.000219
11	0.001035	28	0.000501	11	0.000215
12	0.000978	29	0.000485	12	0.000211
13	0.000926	30	0.000470		
14	0.000880	31	0.000455		
15	0.000837	32	0.000442		
16	0.000798	33	0.000429		
17	0.000762	34	0.000417		

Table 7.2: The calculated photon flux in each centre-of-mass energy bin for both the e-tagger44 and e-tagger33 ranges.

section. To convert the positron-proton cross section into a photon-proton cross section it is necessary to divide by the flux of transverse photons as before. The values of the integrated photon flux obtained in each bin of the e-tagger44 range are listed in Table 7.2. The values for the bins in the e-tagger33 range are also listed. The differential cross section $d\sigma/dW^2_{\gamma p}$ as a function of $W^2_{\gamma p}$ for events selected in the e-tagger44 centre-of-mass energy range is shown in figures 7.9, 7.10 and 7.11. The additional uncertainty in the height of the cross section, arising from the uncertainties in the luminosity, branching ratio and trigger efficiencies, is 1.5%. The differential cross section $d\sigma/dW^2_{\gamma p}$ is shown, for events selected in the e-tagger33 centre-of-mass energy range, as a function of $W^2_{\gamma p}$ in figure 7.12. The additional error in the height of the distribution is 1.6%.

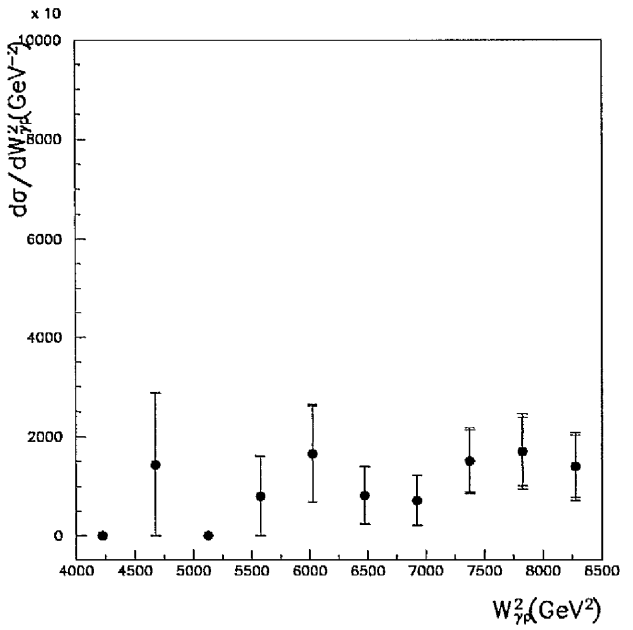

Figure 7.9: The differential cross section $d\sigma/dW^2_{\gamma p}$ as a function of the $W^2_{\gamma p}$ for the process $\gamma p \rightarrow J/\Psi$ p. The outer error bars represent the systematic uncertainties.

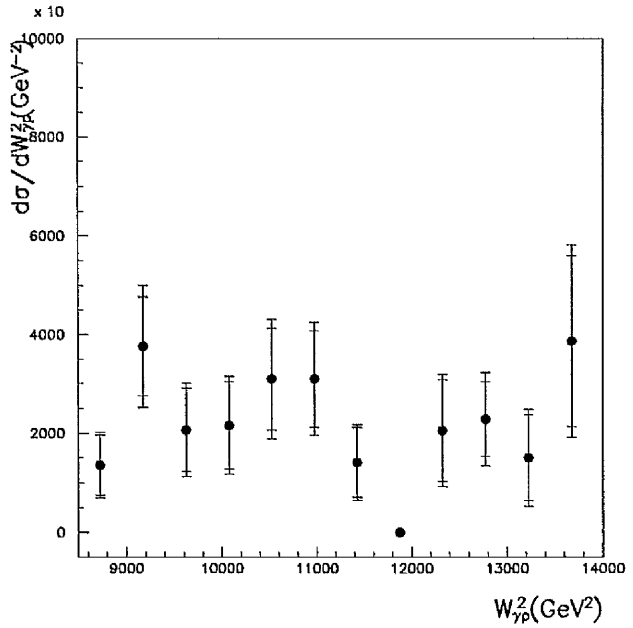

Figure 7.10: The differential cross section $d\sigma/dW^2_{\gamma p}$ as a function of the $W^2_{\gamma p}$ for the process $\gamma p \rightarrow J/\Psi$ p. The outer error bars represent the systematic uncertainties.

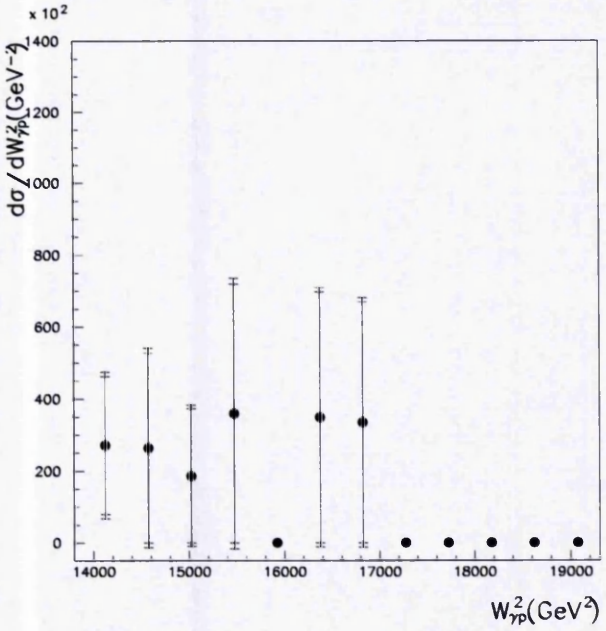

Figure 7.11: The differential cross section $d\sigma/dW^2_{\gamma p}$ as a function of the $W^2_{\gamma p}$ for the process $\gamma p \rightarrow J/\Psi$ p. The outer error bars represent the systematic uncertainties.

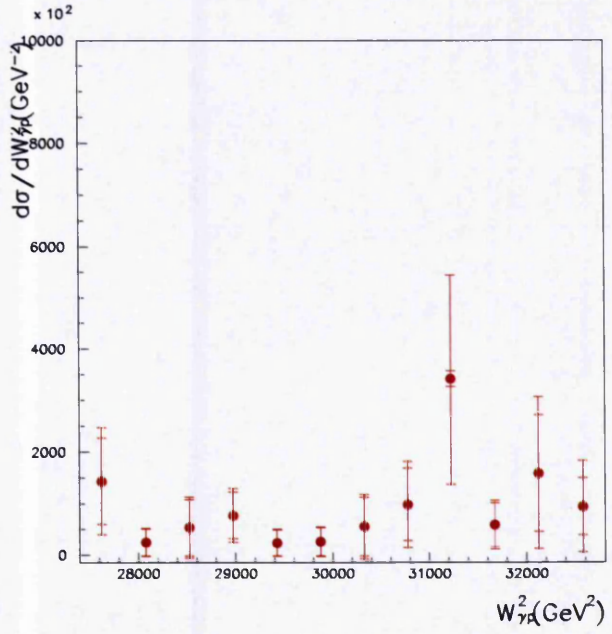

Figure 7.12: The differential cross section $d\sigma/dW^2_{\gamma p}$ as a function of the $W^2_{\gamma p}$ for the process $\gamma p \rightarrow J/\Psi$ p. The outer error bars represent the systematic uncertainties.

Chapter 8

Discussion.

The measured photon-proton differential cross section $d\sigma/dt$ was presented as a function of $|t|$ in two different $W_{\gamma p}$ centre-of-mass energy ranges at the end of chapter 6. Consider first the differential cross section in the lower centre-of-mass energy range. This is most probably described by a smoothly varying function in $|t|$ (there are some very slight variations away from this dependence in the plotted points, however the error bars are still too large to be certain of any real variations). A smooth variation in the differential cross section is predicted in both theories. The Regge theory prediction for the behaviour of the differential cross section was derived in chapter 2. It was given as

$$\frac{d\sigma}{dt} \sim s^{(2\alpha' t + 2\alpha_0 - 2)}.$$

This, however, may also be written as follows

$$\frac{d\sigma}{dt} \sim \exp\left(\ln s^{(2\alpha' t + 2\alpha_0 - 2)}\right)$$

which simplifies to give the following dependence

$$\frac{d\sigma}{dt} \sim \exp(a|t| + b)$$

where $a = -2\alpha' \ln s$ and $b = (2\alpha_0 - 2)\ln s$. The result of a least squares fit of the Regge theory prediction to the low-$W_{\gamma p}$ differential cross section is shown in figure 8.1.

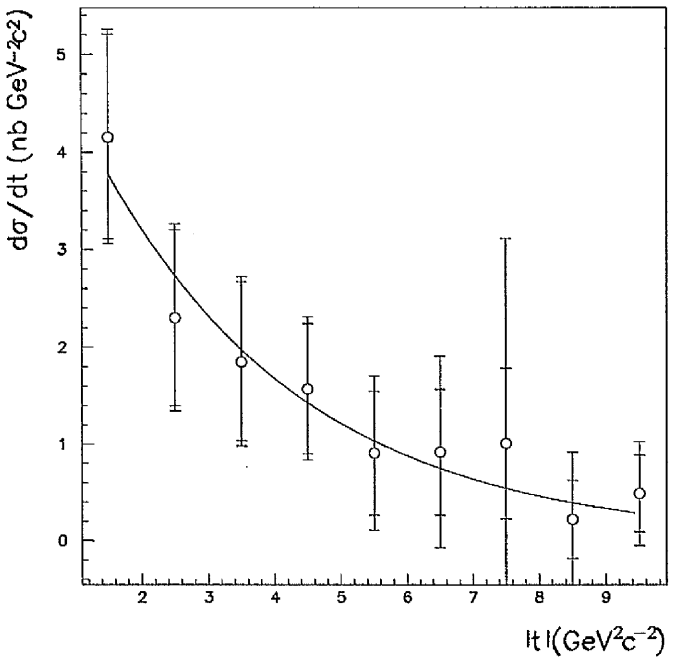

Figure 8.1: The result of a least-squares fit of the Regge theory prediction to the photon-proton differential cross section $d\sigma/dt$ in the e-tagger44 centre-of-mass energy region ($60 < W_{\gamma p} < 147$ GeV).

The best estimates of parameter a may be used to extract an estimate for the gradient of the pomeron trajectory at these energies according to the Regge theory prediction. The best values obtained for the a and b parameters, together with their associated uncertainties, are $a = -0.3 \pm 0.1$ and $b = 8.4 \pm 2.4$. The chi-squared of the fit is 0.114. The best estimate of the gradient of the pomeron trajectory is then given by $\alpha' = 0.016 \pm 0.005$ GeV^{-2}c^{-2}. A value of $s = (103.5)^2$, corresponding to the central value of the $W_{\gamma p}$ range to which this distribution applies, is used. No error in the centre-of-mass energy is included in this estimate. The intercept of the pomeron trajectory may not be estimated since the value of the factor which pre-multiplies the exponential dependence is required. The pre-factor multiplied by e^b gives the height of the cross section at t=0. Clearly it is possible to fit any value for the intercept by making a corresponding change to the fitted pre-factor (the Regge intercept is extracted from fits to the total cross section). The errors here are

obtained in the usual way of summing in quadrature.

The best estimate of the gradient in this centre-of-mass energy range is much smaller than the value of 0.25 $GeV^{-2}c^{-2}$ which was extracted from fits to low t differential cross sections, as described in chapter 2. Regge theory, however, does not predict the gradient and intercept of particle trajectories. These have to be extracted either using the mass states or, if the states are not identified, from fits to total and differential cross sections. The measurement suggests that a pomeron trajectory with a small, positive gradient is responsible for the scattering force in diffractive, high t J/Ψ production, and that this is a different Regge pomeron to that responsible for the scattering force in, for example, low-t proton-proton scattering.

It will be recalled that the pomeron was required to account for the results of scattering experiments performed at high centre-of-mass energies. The typical behaviour of total cross sections which tend to the pomeron trajectory was shown in figure 2.10 for proton-proton and proton-antiproton scattering. Here the two curves join at a centre-of-mass energy of about $\sqrt{s} \approx 160$ GeV. The differential cross section here was measured for centre-of-mass energies of about $W_{\gamma p} \sim 103.5$ GeV. It is important, therefore, to consider whether the extracted behaviour of the pomeron alters as the centre-of-mass energy is increased. Depending on whether the total cross section, for example, converges upon the pomeron dependence from above or below, the extracted intercept in this centre-of-mass energy range would lie either above or below the true value respectively. A better estimate of the parameters of the pomeron trajectory is expected to be extracted in the higher centre-of-mass energy range.

Consider now the differential cross section in the centre-of mass energy range $165 < W_{\gamma p} < 233$ GeV. The Regge theory prediction is fitted to the differential cross section in figure 8.2a). The exponential dependence will only just pass through, within errors, all the points, since the distribution has moved away slightly from the smoother dependence observed in the lower centre-of-mass energy range. The best estimate of the a parameter obtained here is $a = -0.15 \pm 0.23$. The chi-squared of the fit is 0.283. The best estimate for the gradient of the pomeron trajectory extracted from this parameter is then $\alpha' = 0.016 \pm 0.010$ $GeV^{-2}c^{-2}$. A value of $s = (199)^2$ is used to extract this value.

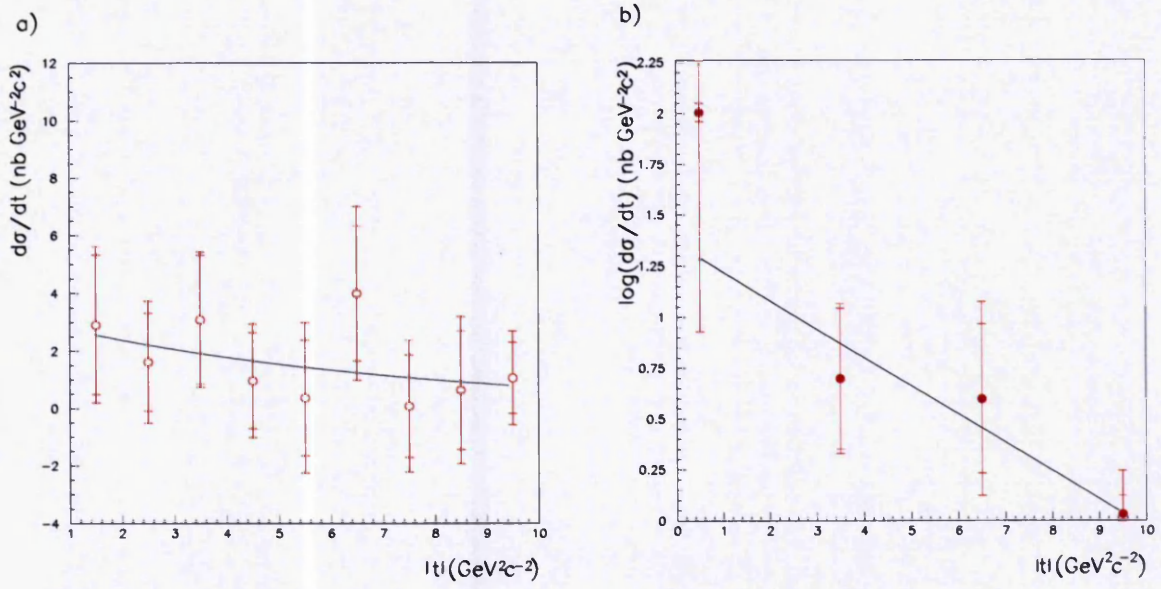

Figure 8.2: a) The photon-proton differential cross section $d\sigma/dt$ in the e-tagger33 centre-of-mass energy region ($165 < W_{\gamma p} < 233$ GeV) and b) the result of a least-squares fit of the Regge theory prediction.

The extracted value of the gradient of the pomeron trajectory in the higher centre-of-mass energy range is consistent with that extracted in the lower centre-of mass energy range. The same Regge trajectory therefore describes the high t differential cross section in both centre-of mass energy ranges. The fall-off of the differential cross section has, however, become more steeper in the higher centre-of-mass energy range. This is expected in Regge theory due to the behaviour of parameter a, which was extracted previously on page 176. Since the expression for the a-parameter is given by

$$a = -2\alpha' \ln s,$$

for a fixed value of the gradient (α') the magnitude of 'a' is expected to increase with increasing centre-of mass energy squared s. This property is referred to as shrinkage, and is a prediction of Regge theory.

A deviation away from the smoother dependence observed at lower centre-of-mass energies is observed at higher s. These deviations might be introduced by the separation of elastic and proton-dissociative events using the forward detectors, but also by a poorer lepton identification at higher $W_{\gamma p}$. No tracking information was used at higher $W_{\gamma p}$. It was also explained, however, in chapter 4 that Regge theory predicts a diffraction pattern to appear at 'high enough' centre-of-mass energies. At HERA, since the energy of the proton is 'fixed' higher centre-of-mass energies correspond to higher photon energies and therefore smaller photon wavelengths. As in optics experiments, the wavelength of the incoming light wave must become comparable with the size of the target for a diffraction pattern to appear. This could also, therefore, account for deviations away from a smooth dependence as the centre-of-mass energy increases.

To test the diffraction pattern hypothesis a fit may be performed to the differential cross section in the higher centre-of-mass energy range. Since the central maximum is expected to appear at $|t| = 0$ GeV^{2}c^{-2} the $|t| = 0-1$ GeV^{2}c^{-2} bin must be included in this fit. The positions of the secondary maxima depend upon the size of the proton target and how they are separated depends upon the shape of the proton, which is not known. In Regge theory the series of maxima and minima are enveloped by the exponential dependence extracted on page 176. This prediction is fitted to the measured differential cross section under the assumption that the maxima are evenly separated by $|t| \sim 3$ GeV^{2}c^{-2} (corresponding to where upward deviations might be appearing) in figure 8.2b). Only the bins $|t| = 0-1$ GeV^{2}c^{-2}, $|t| = 3-4$ GeV^{2}c^{-2}, $|t| = 6-7$ GeV^{2}c^{-2} and $|t| = 9-10$ GeV^{2}c^{-2} are therefore considered. The differential cross section, however, might continue to rise as $|t|$ is increased beyond the highest $|t|$-bin and one could also argue that the differential cross section is consistent with zero for $|t| > 7$ GeV^{2}c^{-2}. Since the differential cross section is large at low t the log of the differential cross section is plotted. A straight line dependence is expected with a gradient given by $-2\alpha' \log s$. The best estimate of the gradient is -0.14 ± 0.06 (the best estimate of the intercept is 1.4 ± 0.5). The chi-squared of the fit is 0.378. Using a central value of $s = (199)^2$ GeV^2 the best estimate of the gradient of the pomeron trajectory is therefore $\alpha' = 0.016 \pm 0.010$ GeV^{-2}c^{-2} and is consistent with the values extracted previously. It is therefore not possible to rule out that a diffraction pattern is starting to appear at these centre-of-mass energies. Also the same extracted trajectory might also describe the low t region.

Consider now comparing this result to the results of other analyses. Previous differential cross sections obtained from a consideration of just low |t| scattering and just high |t| scattering are both shown in figure 8.3. The low |t| result has been published [51], whereas the high |t| distribution represents a preliminary result [52]. Both of the differential cross sections are presented for positron-proton scattering at HERA. The method of anti-tagging the scattered lepton was used, so the results cover a slightly different kinematic range. The J/Ψ was selected via its decay to muons [52]. It is first of all apparent that there is a very sharp change in the fall-off of the differential cross section at $|t| = 1.0$ GeV^{2}c^{-2}. This could be interpreted as being due to a second, different pomeron giving rise to the scattering force at high t. If just low |t| events are considered, however, the fall off of the differential cross section is typically very steep (corresponding to just the central maximum). In the high centre-of-mass energy range considered here a pomeron trajectory with a gradient of about $\alpha' \sim 0.14$ GeV^{-2}c^{-2} would be needed to account for the fall-off between the first and second |t| bins. This gradient is much more consistent with the value of $\alpha' = 0.25$ GeV^{-2}c^{-2}, previously extracted using Regge theory. If, on the other hand, one ignores the low |t| events and attempts to fit a dependence through all the high |t| points, a much smaller gradient will be obtained. It may be necessary therefore to examine the diffraction pattern hypothesis in more detail. The sudden change at $|t| = 1.0$ GeV^{2}c^{-2} also occurs exactly where the low t region where DIFFVM is used and the high t region where HITVM is used meet.

The data points show a rise at about $|t| = 3.5$ GeV^{2}c^{-2} and again at about $|t| = 6.5$ GeV^{2}c^{-2} as in the higher centre-of-mass measurement of this analysis. The results of these analyses suggest the production of a similar deviation away from a smooth dependence in the muon channel, although the centre-of-mass energy range considered in the muon analysis only corresponds to the lower centre-of-mass energy range considered here . It is hard to believe, however, that identical statistical deviations arose in both analyses (1994 and 1995 data were considered in the muon analysis). The Regge dependence for one particular choice of the pomeron gradient and intercept is also plotted. The detection of events at high |t| only, however, rules out this particular choice of trajectory, not the prediction in general.

The differential cross sections measured here are well described by a Regge trajectory with a gradient $\alpha' = 0.016 \pm 0.005$ GeV^{-2}c^{-2}. As the centre-of-mass energy is increased the cross section becomes narrower and starts to collect at low t

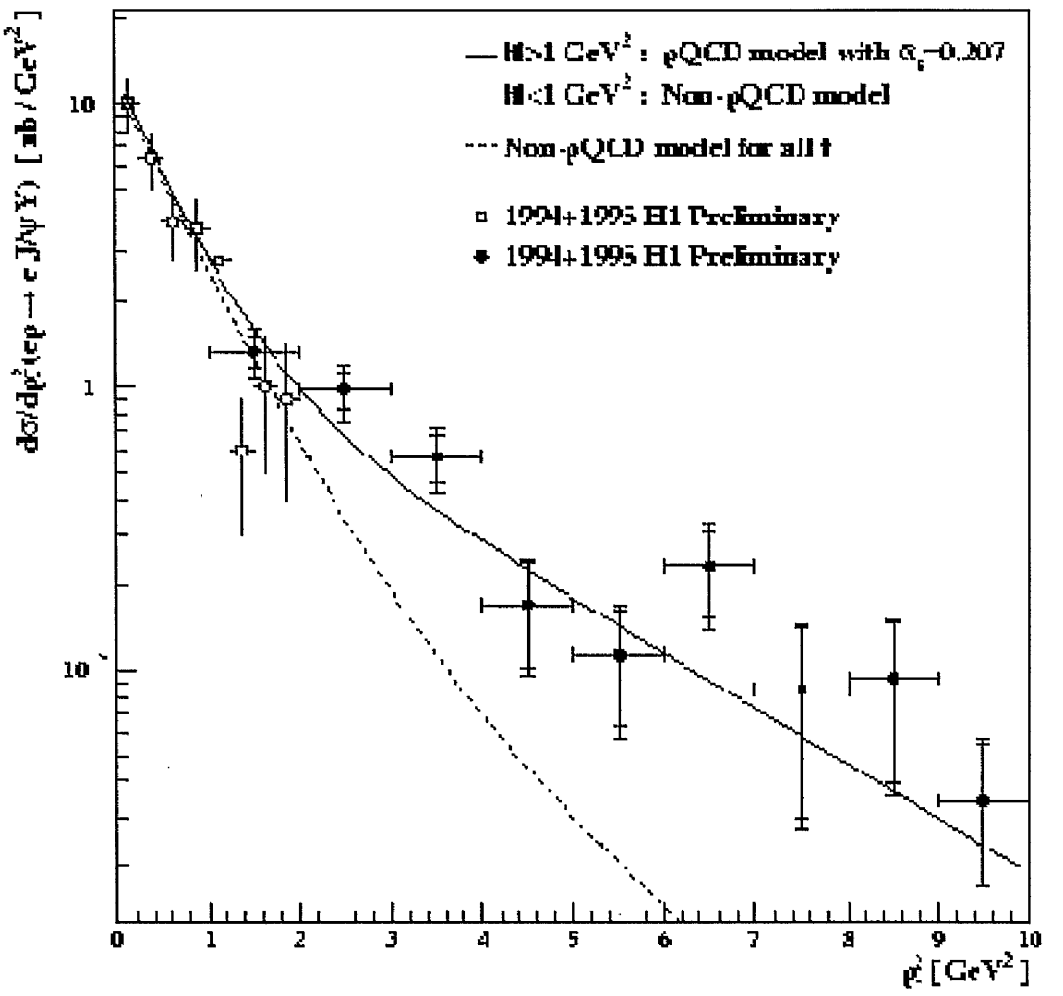

Figure 8.3: The published low-t data for diffractive J/Ψ (open points) and the results of a high-t analysis in which the J/Ψ was selected via its decay to muons (closed points).

(in the range $165 < W_{\gamma p} < 233$ GeV the first |t|-bin contains about 83% of the observed cross section, compared to only about 50% in the lower centre-of-mass energy range). The behaviour of the differential cross sections agree well with the predicted shrinkage of the diffraction peak in Regge theory. The appearance of a shrinkage effect is not predicted in perturbative QCD. These and other high t

measurements are perhaps indicating a shift away from a smooth dependence for increasing $W_{\gamma p}$ and increasing Q^2. These deviations can be consistently described by a diffraction pattern here using the same pomeron gradient extracted from the exponential fits. There is then no change in the fall-off of the differential cross section at $|t| = 1.0$ GeV^{2}c^{-2}. At still higher values of s, however, shrinkage predicts that the cross section will tend to a very narrow central maximum (this is also expected through the optical theorem) which contains all of the cross section, therefore justifying the approximation that the pomeron gradient may be extracted from low t measurements.

Consider now the behaviour of the intercept of the pomeron trajectory. Over the kinematic region considered here the total cross section may still be converging upon the pomeron. For a fixed value of the factor which pre-multiplies the expression for the differential cross section in Regge theory, the value of the intercept required to reproduce the height of the differential cross section at $t = 0$ may differ in the lower and higher centre-of mass energy ranges. The ratio of the heights of the differential cross sections at $t = 0$ is given, according to Regge theory, by

$$r = \frac{A s_1^{2(\alpha_0^a - 1)}}{A s_2^{2(\alpha_0^b - 1)}}$$

where α_0^a and α_0^b refer to the effective intercepts in the lower centre-of-mass energy range ($s = s_1$) and the higher centre-of-mass energy range ($s = s_2$) respectively. Taking the log of this equation gives

$$\log r = 2(\alpha_0^a \log s_1 - \alpha_0^b \log s_s) - 2(\log s_1 - \log s_2).$$

Using, once again, values of s which correspond to the central values of the ranges considered one may approximate the ratio using the heights of the differential cross section in the $|t| = 0 - 1$ GeV^{2}c^{-2} bin giving

$$\alpha_0^a \approx 1.14\alpha_0^b - 0.217.$$

The ratio is given by $r = 0.25 \pm 0.04$. There is a linear relationship between the intercept required in the lower centre-of-mass energy range and the intercept required in the higher centre-of-mass energy range. The line intersects the line $\alpha_0^a = \alpha_0^b$ at about 1.55. If one were to fit the variation in the cross section with one fixed value of the pomeron intercept this is the value that would be obtained. Below this value

however α_0^a is always smaller than α_0^b, therefore, in the range where the intercept is expected in both theories the cross section is expected to converge on the pomeron trajectory from below (if the intercept is actually higher than about 1.55 then the trajectory is expected to converge from above). The total cross section is therefore expected to be rising quicker with centre-of-mass energy in this region as it converges to the pomeron trajectory. If it were now attempted to describe this variation with a single pomeron intercept, the intercept would be overestimated.

The measured photon-proton differential cross section $d\sigma/dW^2_{\gamma p}$ was presented as a function of $W^2_{\gamma p}$, in two $W^2_{\gamma p}$ ranges, at the end of chapter 7 for events in which the proton remained intact. The gradient of the total cross section plotted as a function of s is therefore sampled here in small bins of s. In Regge theory the total cross section is predicted to behave as

$$\sigma \sim s^{\alpha_0 - 1}$$

where α_0 is the intercept of the leading Regge pole. Differentiating this with respect to s gives

$$\sigma \sim s^{\alpha_0 - 2}.$$

The differential cross section $d\sigma/dW^2_{\gamma p}$ multiplied in each bin by s therefore gives, apart from a pre-multiplying constant, a measurement of the total cross section. The differential cross section is converted into a total cross section and plotted, for the e-tagger44 centre-of-mass energy range, in fig. 8.4a), and across both centre-of-mass energy ranges in fig. 8.4b).

Consider first the total cross section for events selected by e-tagger44. The total cross section is rising over this centre-of-mass energy range. As previously explained, however, the total cross section may still be converging upon the pomeron trajectory in this region. One must therefore be careful not to fit a functional dependence prematurely. A smoothly varying function would describe this rise well. As s becomes larger, however, the total cross section starts to deviate away from a smooth dependence. This effect could, however, be simply due to the smaller statistics obtained in these bins. Consider now the total cross section viewed across both the investigated regions. In the e-tagger33 s-range a better approximation to pomeron behaviour is expected. Here, however, the total cross section has moved still further away from a smooth dependence. This behaviour does not appear to have been introduced by the bin acceptances.

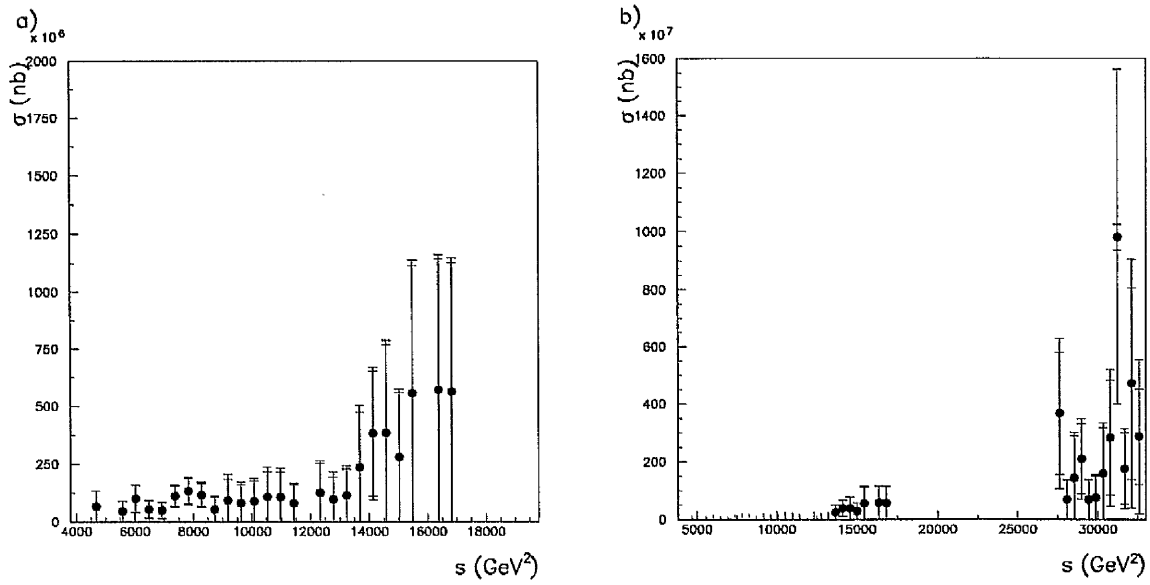

Figure 8.4: a) The measured total cross section for $\gamma p \rightarrow J/\Psi$ p in the s-range covered e-tagger44 and b) the same measurement together with the total cross section measured in the s-range covered by e-tagger33.

It was explained at the beginning of chapter 7 that, if a trajectory of bound states exist, one version of each of the pomeron states are expected to be produced as resonances in this scattering process. The differential cross sections $d\sigma/dt$ appear to be more consistent with the Regge theory approach. The deviation away from a smooth dependence in the total cross section as s is increased might indicate a resonant production of pomeron states, as suggested by Regge theory. Higher statistics, however, will be needed.

Chapter 9

Conclusion.

The lepton-proton and photon-proton differential cross sections $d\sigma/dt$ have been measured as a function of t for diffractive J/Ψ production in the photon-proton centre-of-mass energy ranges $60 < W_{\gamma p} < 147$ GeV and $165 < W_{\gamma p} < 233$ GeV, using data taken during 1997 by the H1 detector at HERA. A photon elasticity cut of $z > 0.8$ was used to select J/Ψ vector mesons produced elastically at the photon vertex. Photon virtualities $Q^2 < 0.01$ GeV^{2}c^{-2} were selected by tagging the scattered lepton and proton-dissociative events were selected by demanding a proton remnant mass greater than about 1.6 GeVc^{-2} at the proton vertex. The differential cross sections were measured in the range $|t| = 0 - 10$ GeV^{2}c^{-2}.

The differential cross sections in both the lower and higher $W_{\gamma p}$ ranges were well described by a falling exponential dependence. The fall-off in the higher centre-of-mass energy range was sharper, however, than the fall-off in the lower centre-of-mass energy range, a greater percentage of the observed cross section collecting in the $|t| = 0 - 1$ GeV^{2}c^{-2} range at higher s than at lower s. The gradient of the pomeron trajectory obtained by performing an exponential fit in the lower centre-of-mass energy range was $\alpha' = 0.016 \pm 0.005$ GeV^{-2}c^{-2}. In the higher centre-of-mass energy range the extracted value was $\alpha' = 0.016 \pm 0.010$ GeV^{-2}c^{-2}. These gradients were found to be consistent with each other and therefore with the prediction for a shrinkage of the diffraction peak in Regge theory. No shrinkage is expected within the framework of perturbative QCD. The measured gradient of this trajectory, however, suggests that a different pomeron is responsible for the scatter-

ing force in high t, diffractive J/Ψ production than that responsible for the force in the low t processes used to extract the soft pomeron behaviour. Shrinkage, however, predicts that the cross section will shift towards low $|t|$ with increasing s, and this justifies the use of low t measurements to approximate the behaviour of the pomeron. A pomeron gradient extracted using just the low $|t|$ data was found to be much larger than that obtained by a fit to the entire t-range. This also suggested that as s is increased the gradient of the pomeron trajectory will tend towards the soft pomeron value and further away from the QCD prediction.

The measurements are consistent with the results of low $|t|$ and high $|t|$ muon channel analyses. Possible deviations away from a smooth exponential dependence in this and the muon channel analyses were discussed. It was not possible to rule out that a diffraction pattern starts to appear at higher $W_{\gamma p}$ and higher Q^2. Diffraction patterns are predicted in Regge theory at 'high enough' s. It was possible to describe the behaviour of the differential cross section over the whole t-range at high $W_{\gamma p}$ in terms of the same, single pomeron trajectory extracted from the exponential fits using this prediction.

The lepton-proton and photon-proton differential cross sections $d\sigma/dW^2_{\gamma p}$ have been measured as a function of $s = W^2_{\gamma p}$ in the same kinematic region for diffractive J/Ψ production in which the proton remains intact (proton remnant masses less than about 1.6 $GeVc^{-2}$). The differential cross section $d\sigma/dW^2_{\gamma p}$ can be converted into a measurement of the total proton-intact cross section as a function of s. The total cross section is rising over this kinematic range. A deviation away from a smooth dependence is observed in the total cross section with increasing s. These deviations might be interpreted as being due to the resonant production of pomeron states, as predicted by Regge theory.

It is concluded that the Regge theory gives a much more plausible description of relativistic scattering. A higher luminosity has since been collected by the H1 detector during 1999 and this provides an opportunity to decrease the statistical uncertainties in these measurements. A more detailed approach to decoupling the parameters of the pomeron trajectory from convergence effects is however needed. Of particular interest would be a measurement of the total cross section across the entire s-range visible at HERA. This may be done at HERA by anti-tagging the scattered lepton, which in itself would lead to an increase in available statistics. In

addition, an investigation of the differential cross section $d\sigma/dt$ in the muon channel with increasing centre-of-mass energy should confirm the shrinkage effect observed here. Investigations of the diffractive process which make use of both of the leptonic decay modes of the J/Ψ should also be considered.

Acknowledgements The author would particularly like to acknowledge Sandy Donnachie, Jeff Forshaw and Terry Wyatt for their valuable help. In addition, the author would like to thank Roger Barlow, Vato Kartelishvili, Ben Waugh, Chris Hilton, Paul Neumann, Andy Mehta, Julian Philips and Paul Thompson for many useful discussions.

Appendix A

Feynman Rules for QCD

The following Feynman Rules are required for the amplitudes considered when deriving the BFKL pomeron in QCD:

Gluon propagator

$$\frac{-i\delta_{ab}g_{\mu\nu}}{(k^2+i\epsilon)}$$

Massless fermion propagator

$$\frac{i\delta_{ij}(\gamma\cdot k)_{\alpha\beta}}{(k^2+i\epsilon)}$$

Fermion-gluon interaction

$$-ig(\tau^a)_{ij}(\gamma^\mu)_{\alpha\beta}$$

Gluon self interaction

$$ig(T^a)_{bc}[g^{\mu\rho}(q-p)^\mu + g^{\rho\mu}(2p+q)^\nu - g^{\mu\nu}(p+2q)^\rho]$$

Appendix B

Reconstructed Mass Distributions in Bins of $W^2_{\gamma p}$

B.1 E-tagger44 Mass Distributions.

The reconstructed mass distributions in the e-tagger44 range. The first row, from left to right, contains bins 1, 2 and 3, the second row bins 4, 5 and 6 and so on.

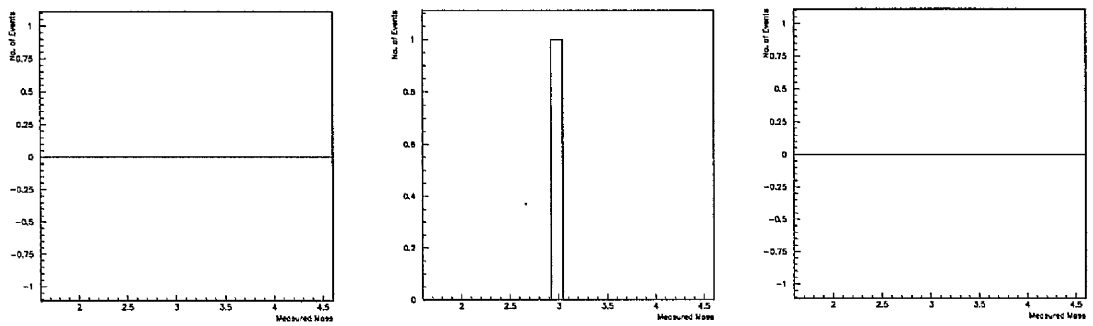

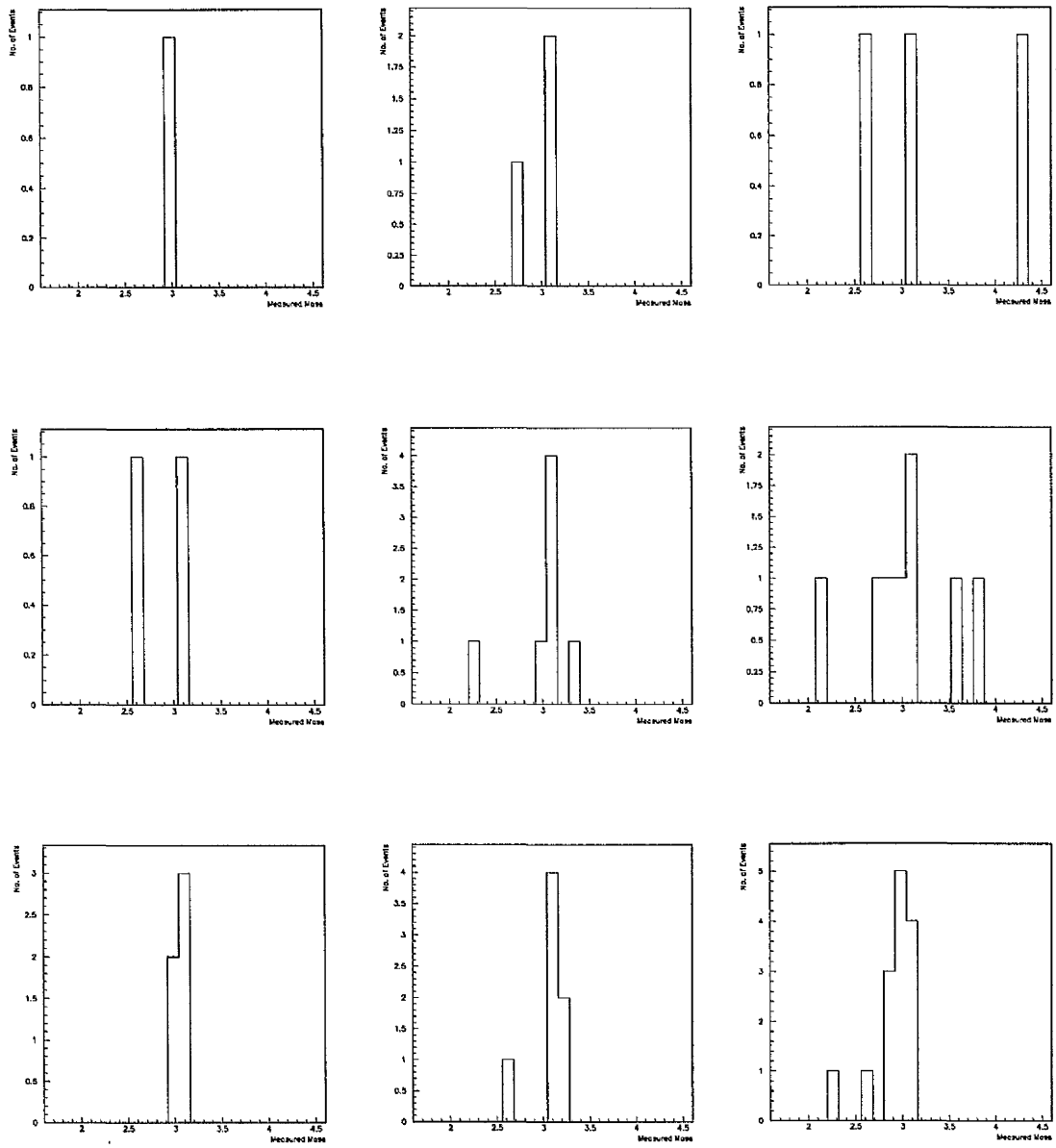
No. of Events
Measured Mass

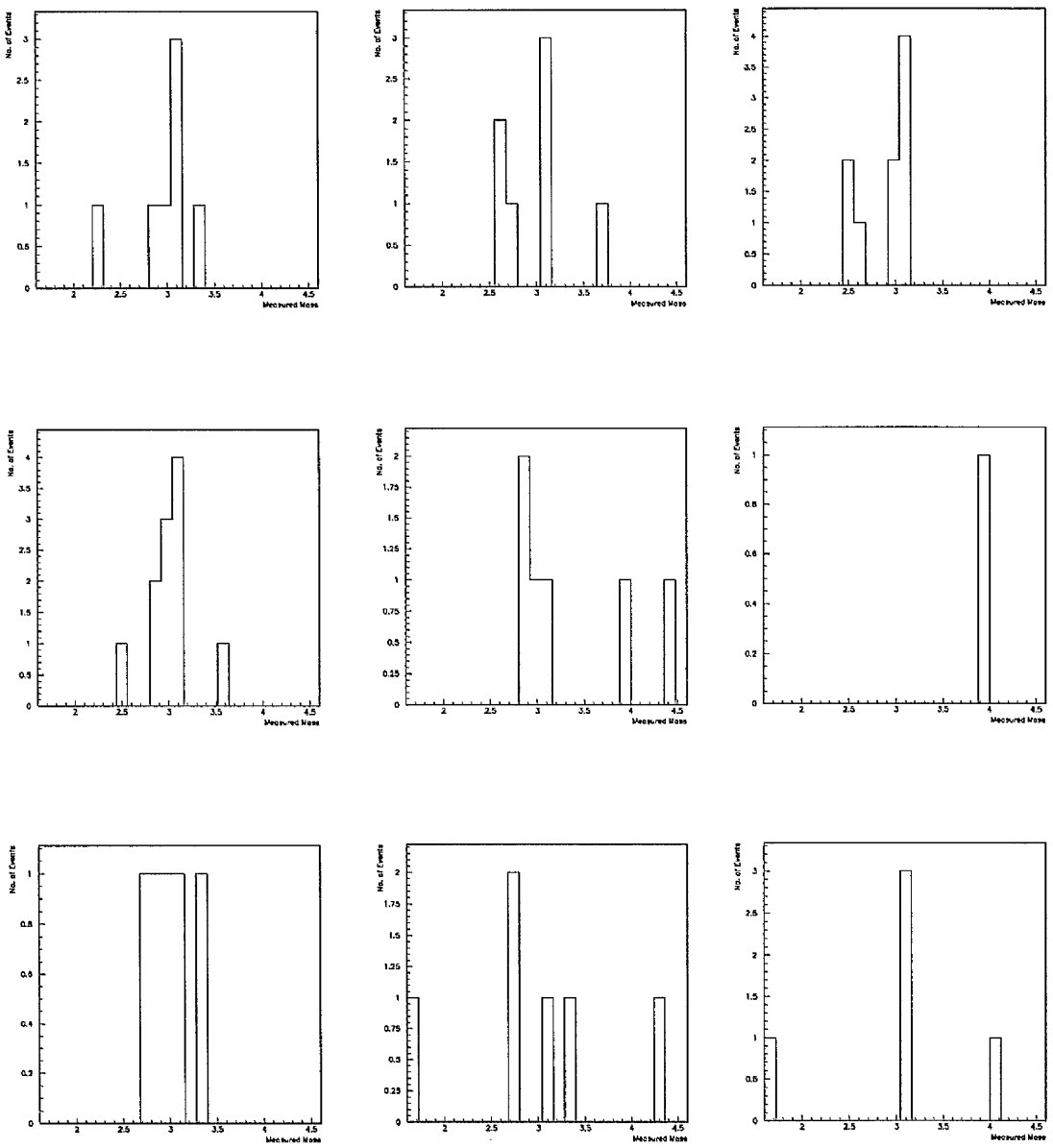
No. of Events
Measured Mass

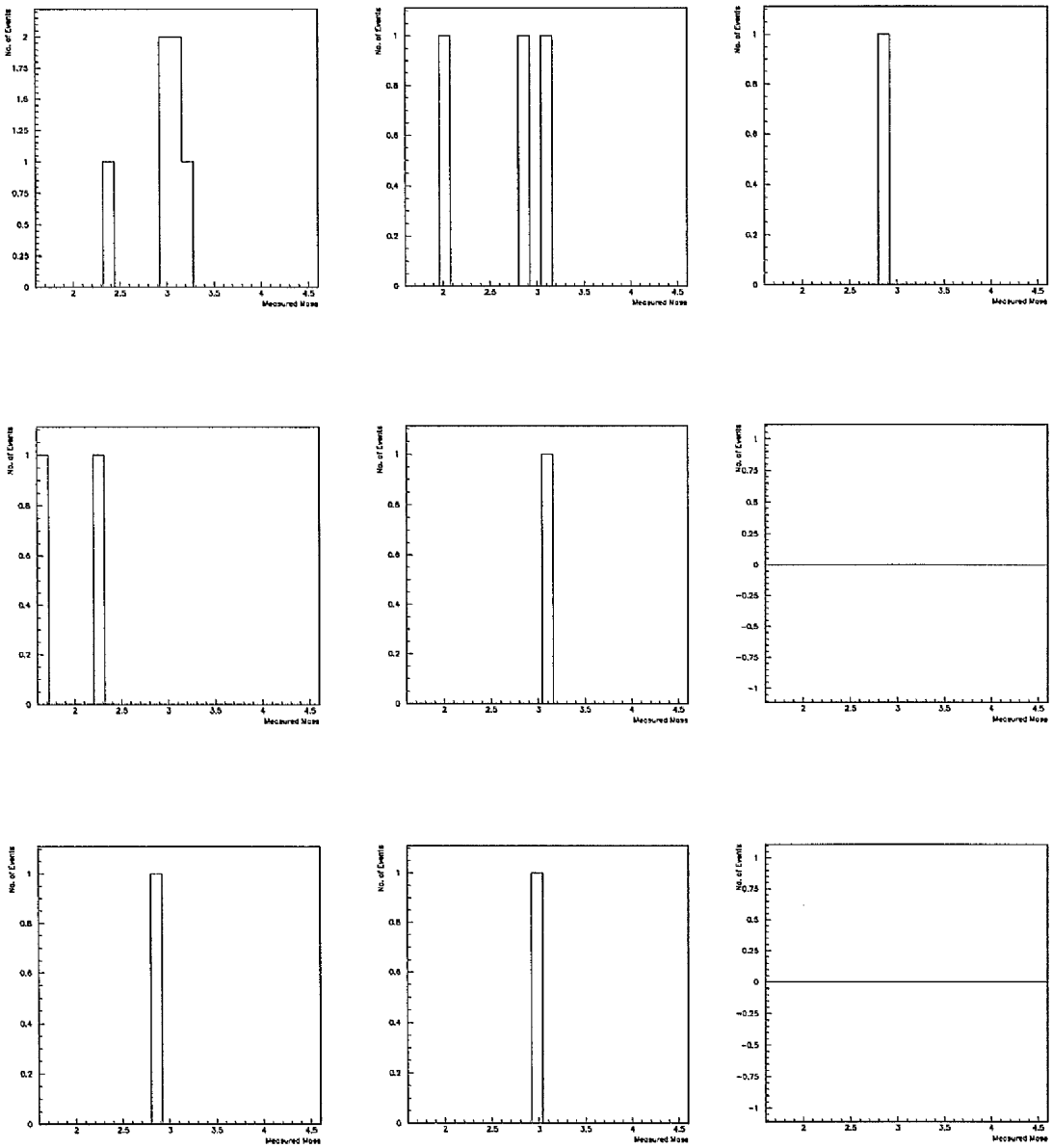
No. of Events
Measured Mass

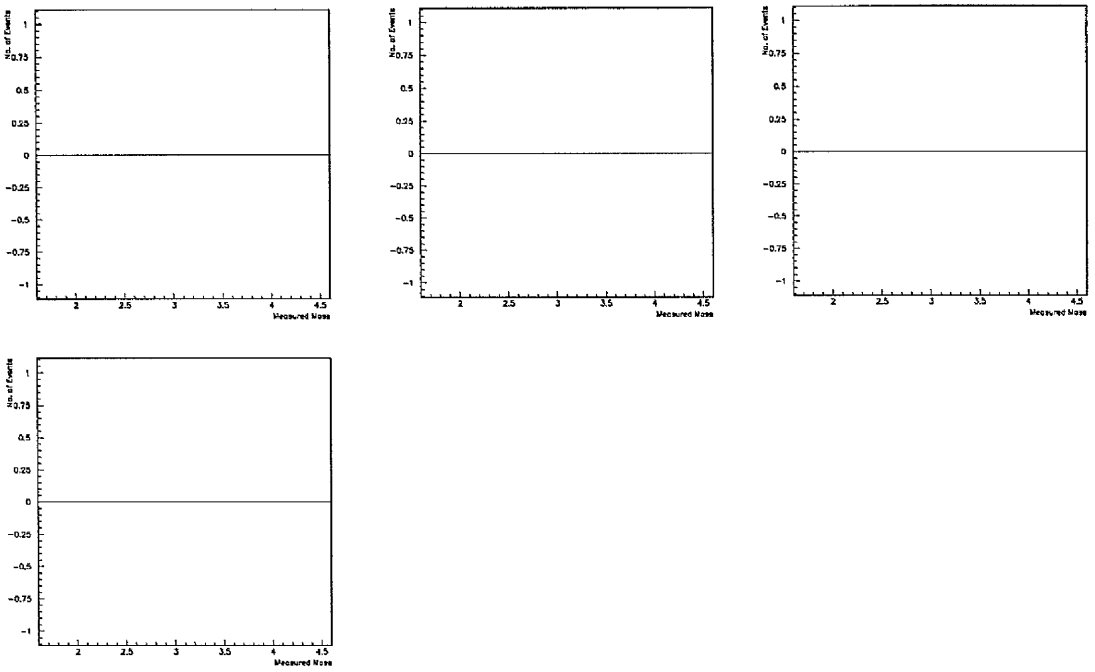

Figure B.1: The data mass distributions in bins of s in the e-tagger44 centre-of-mass energy range.

B.2 E-tagger33 Mass Distributions.

The reconstructed mass distributions in the e-tagger33 range. The first row, from left to right, contains bins 1, 2 and 3, the second row bins 4, 5 and 6 and so on.

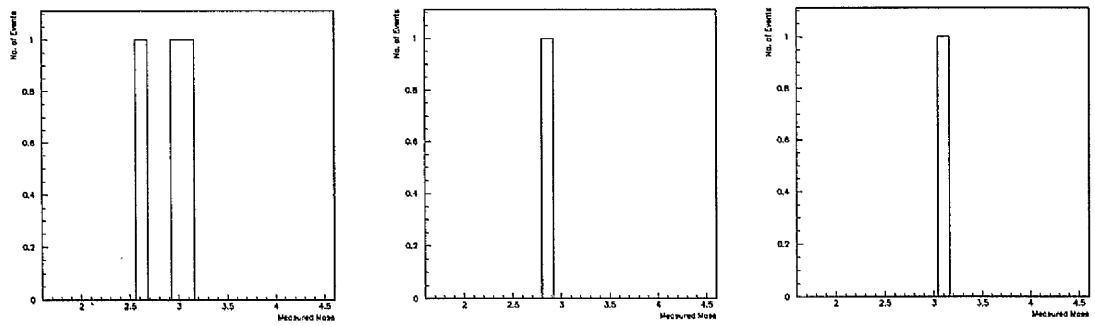

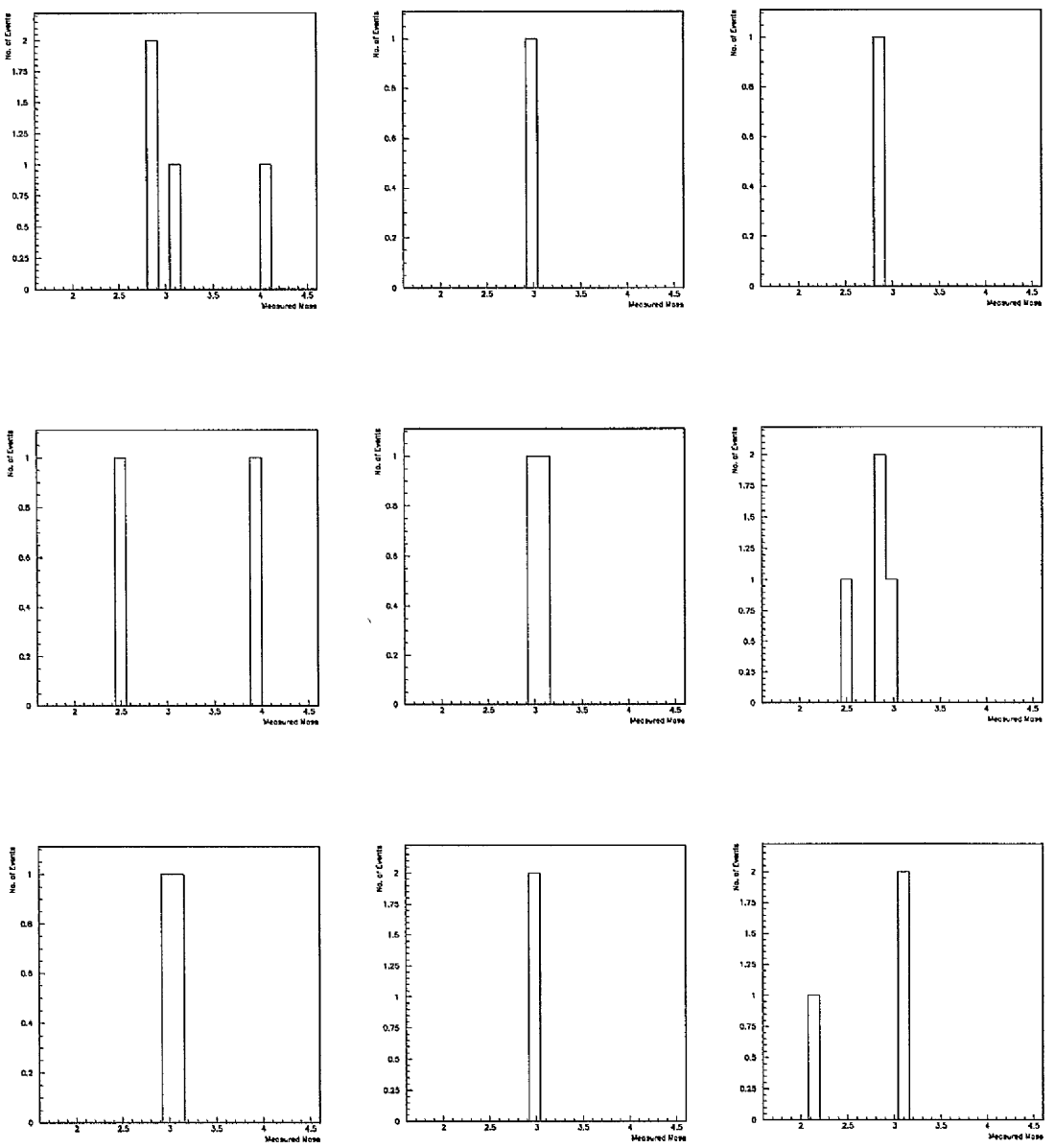

Figure B.2: The data mass distributions in bins of s in the e-tagger33 centre-of-mass energy range.

Bibliography

[1] Shankar, R., (1980) "The Principles of Quantum Physics" Plenum Press. p553

[2] Abatzis, S., et al. (1994) Phys. Lett. B324, 509

[3] Rae, A. I. M., (1993) "Quantum Mechanics" Third Edition. I. O. P. Publishing. p190

[4] Bronstein, I. N., Semendjajew, K. A., Musiol, G., & Mühlig, H., (1993) "Taschenbuch Der Mathematik" Verlag Harri Deutsch.

[5] French, A. P., & Taylor, E. F., (1978) "An Introduction to Quantum Physics" The Massachussetts Institute of Technology. p110

[6] Townsend. J. S., (1992) "A Modern Approach to Quantum Mechanics" McGraw-Hill International Editions. p383

[7] Williams W. S. C., (1971) "An Introduction to Elementary Particles" Second Edition. Academic Press. pp68-70

[8] Omnès, R., (1971) "Introduction to Particle Physics" Wiley Interscience. pp171-89

[9] Park, D., (1966) "Introduction to Strong Interactions" W. A. Benjamin, Inc. p105

[10] Mathews, J. & Walker, R. L., (1970) "Mathematical Methods of Physics" Second Edition. Addison-Wesley Publishing Company, Inc.

[11] Froissart, M. & Omnès, R., (1963) "Mandelstam Theory and Regge Poles" W. A. Benjamin, Inc. pp41-53

[12] Regge, T., (1959) Nuov. Cim. 14, 951

[13] Regge, T., (1960) Nuov. Cim. 18, 947

[14] Watson, G. N., (1918) Proc. Roy. Soc. 95, 83

[15] Sommerfeld, A., (1949) Partial Differential Equations in Physics, Academic Press

[16] Eden R. J., (1967) "High Energy Collisions of Elementary Particles" Cambridge University Press. p128-9

[17] Cheng, D. C. & O' Neill G. K., (1979) "Elementary Particle Physics" Addison-Wesley Pulishing Company. p391

[18] Chew, G. F. P., & Frautschi, S. C., (1961) Phys. Rev. Lett. 7, 394

[19] Barnes, A. V., et al. (1976) Phys. Rev. Lett37, 76

[20] Donnachie, A., & Landshoff P. V., (1992) Phys. Lett. B296, 227

[21] Pomeranchuk, I. Y., (1956) Sov. Phys. 3, 306

[22] Foldy, L. F., & Peierls, R. F., (1963) Phys. Rev. 130, 1585

[23] Störmer, H. & Tsui, D. C. (1994) "Composite Fermions: New particles in the fractional quantum Hall effect" Physics News in 1994, American Institute of Physics 1995, p. 33

[24] Lictenberg D. B., (1978) "Unitary Symmetry and Elementary Particles" Second Edition. Academic Press. pp193-201,246-250

[25] Berger, C. (1992) "Teilchenphysik: Eine Einführung" Springer-Verlag.

[26] Dirac, P. A. M., (1935) "The Principles of Quantum Mechanics" Second Edition. Oxford University Press.

[27] Bjorken J. D. & Drell S. D., (1964) "Relativistic Quantum Mechanics" McGraw-Hill Book Company. p96

[28] Eden, R. J., Landshoff, P. V., Olive, D. I., & Polkinghorne J. C., (1966) "The Analytic S-matrix" Cambridge University Press.

[29] Cutkosky, R. E. (1960) J. Math. Phys. 1, 429

[30] Ryder, L. H. (1996) "Quantum Field Theory" Second Edition. Cambridge University Press.

[31] Forshaw, J. R. & Ross, D. A. (1997) "Quantum Chromodynamics and the Pomeron" Cambridge University Press. pp25-112

[32] Tyburski, L. (1976) Phys. Rev. D13, 1107

[33] Franfurt, L. L., & Shermann, V. E., (1976) Sov. J. Nucl. Phys. 23, 581

[34] Lipatov, L. N., (1976) Sov. J. Nucl. Phys. 23, 338

[35] Cheng, H., & Lo, C. Y., (1976) Phys. Rev. D13, 1131

[36] Boas., M. L., (1983) "Mathematical Methods in the Physical Sciences" Second Edition. John Wiley & Sons.

[37] Fadin, V. S., Kuraev, E. A. & Lipatov. L. N., (1976) Sov. Phys. JETP 44, 443

[38] Balitsky, Y. Y. & Lipatov, L. N., (1978) Sov. J. Nucl. Phys. 28, 822

[39] Lipatov, L. N. (1986) Sov. Phys. JETP 63, 904

[40] Landshoff, P. V., & Polkinghorne, J. C., (1971) Nucl. Phys. B32, 541

[41] Levin, E. M. & Tan, C. (1992) Brown Preprint HEP-889 hep-ph/9302308

[42] Bartels, J., Forshaw, J. R., Lotter, H. & Wüsthoff, M. (1995) "Diffractive Production of Vector Mesons at Large t"

[43] Sakurai, J. J. (1969) "Currents and Mesons" The University of Chicago Press. Chicago-London.

[44] Forshaw, J. R. & Ryskin, M. G. (1995) "Diffractive Vector Meson Production at Large Momentum Transfer" HEP-PH-9501376

[45] H1 Collaboration (1996) "Elastic and Inelastic Photoproduction of J\Ψ Mesons at HERA." DESY 96-037

[46] H1 Collaboration (1997) "The H1 Detector at HERA" Nucl. Instr. and Meth. A386 pp310-396.

[47] H1 Collaboration "The H1 Liquid Argon Calorimeter System" NIAM. A336 (1993) 460-498

[48] Andreev, V. (1996) "Acceptance Determination of Electron Tagger (ET44) in 1995" H1-10/96-493

[49] Future Physics at HERA. Proc. of the Workshop 1995/96. Volume 2. Ed. Ingelmann, G., De Roeck, A., & Klamer, R.

[50] Physics at HERA. Volume 3. Monte Carlo Generators. Proc. of the Workshop 1991. Ed. Ingelmann, G., & Buchmüller, W.

[51] Aid, S. et al., (1996) H1 collaboration. Nucl. Phys. B472. Submitted to the 28th International Conference on High Energy Physics, Warsaw, Poland, July 1996

[52] West, L. (1997) "Production of J\Ψ Mesons with large $|t|$ at HERA" Submitted to the International Conference on High Energy Physics HEP97, Jerusalem, Israel, August 1997.